

Magnetic Resonance Force Microscopy: Harnessing Nuclear Spin Fluctuations

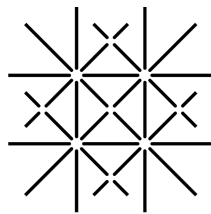
Inauguraldissertation

zur

Erlangung der Würde eines Doktors der Philosophie
vorgelegt der
Philosophisch-Naturwissenschaftlichen Fakultät
der Universität Basel

von

Phani Peddibhotla
aus **Indien**



**UNI
BASEL**

Basel, 2013

Genehmigt von der Philosophisch-Naturwissenschaftlichen Fakultät
auf Antrag von
Prof. Dr. Martino Poggio
Prof. Dr. Christian Degen

Basel, den **18. June 2013**

Prof. Dr. Jörg Schibler
Dekan

To my beautiful wife,

Lakshmi Sai Phani Keerthana Sripada

Contents

Acknowledgements	v
List of Symbols	vii
List of Figures	ix
Abstract	xi
1 Introduction	1
2 Spin Physics	5
2.1 Spin in a static magnetic field	5
2.2 Spin in a rotating magnetic field	7
2.3 Spin in a magnetic field gradient	9
2.4 Spin relaxation induced by a mechanical resonator	10
2.5 Spin relaxation - Kubo-Anderson model	12
2.6 Spins - polarization and distribution	18
2.6.1 Multinomial distribution	19
2.6.2 Density matrix	21
2.6.3 Gaussian distribution	23
3 Nanomechanical Resonators	27
3.1 Brownian motion	27
3.2 Driven motion	30
4 Experimental Apparatus	33
4.1 Operation	33
4.2 Cantilevers	34
4.3 Fiber-optic interferometer	34
4.4 Microwire RF source	38
4.5 RF pulse generation	39

4.5.1	Arbitrary waveform generator	39
4.5.2	Timing	39
4.5.3	Digital synthesis of amplitude and phase modulated RF pulses	40
4.6	FPGA-based control system	42
4.6.1	Laser PID controller	44
4.6.2	Displacement PID controller	44
4.6.3	Optimal controller	45
4.6.4	Phase locked loop (PLL)	45
4.6.5	Lock-in filter bank	46
4.6.6	Frequency counter, trigger and pulse generator	47
5	Spin Order	49
5.1	Introduction	49
5.2	Nanowire sample preparation	51
5.3	Nanowire growth	51
5.3.1	InP nanowire growth	51
5.3.2	GaP nanowire growth	52
5.4	Experimental details	53
5.5	ARP sweep detection protocol	54
5.6	Nuclear spin noise simulations	57
5.7	Real-time measurement	58
5.8	Real-time control	60
5.9	Non-equilibrium spin states in the rotating frame	61
5.10	Capture-store-readout pulse sequence	63
5.11	Narrowing of spin polarization fluctuations	67
6	Magnet-on-Cantilever MRFM	71
6.1	Introduction	71
6.2	Magnetic tips	73
6.3	Microcoil	74
6.4	Outlook	74
7	Outlook	77
A	FPGA Programs	79
A.1	Steps to run the laser PID controller	79
A.2	Steps to run the displacement PID controller	80
A.3	Steps to run the phase shifter	80

B	MATLAB simulation of spin noise	81
C	Microcoil fabrication steps	83
	Bibliography	85
	Curriculum Vitae	89
	List of Publications	91

Acknowledgements

Firstly, I express my sincere gratitude to my advisor Prof. Dr. Martino Poggio for giving me an opportunity to pursue doctoral research in his group. I thank him for reposing faith in my capabilities and accepting me as the first member of his group. Starting as a novice, I couldn't have learnt the nuts and bolts of experimental physics without his teaching and guidance. He was always available, even in the weekends, to help me in setting up and running the experiments. His office doors were always open to me for discussions and questions despite how busy I am sure he is as a young professor.

Working in a small research group gave me a good opportunity to learn a great deal from my group members. Each and every contribution, whether big or small, is vital for increasing the knowledge base of a research group. We couldn't have performed state-of-the-art magnetic resonance force microscopy (MRFM) experiments without the substantial contributions made by Dr. Fei Xue. I am thankful to him for the long discussions we had about the various technical aspects of running an MRFM experiment. I thank Michele Montinaro and Dennis Patrick Weber for inducting me into the clean room techniques. Special thanks to Dennis for sharing his tricks and expertise on SEM imaging of the cantilevers and the electron beam lithography. It was nice to see Michele having succeeded in pursuing the QPC transport project to completion. I am sure he has found a worthy successor in Andrea Mehlin who will continue working in this research direction. I thank Arne Buchter for always providing me prompt assistance with the various computer tasks. I wish him success in the diverse scientific projects he is able to handle. It was impressive to see Benedikt Herzog and Pengfei Wang build their experimental setups almost single-handedly.

I thank Dr. Hari Shankar Solanki for always being willing to help me in the lab and answer all the technical questions I have got. I will value the much needed support and encouragement he has provided me during the tough and frustrating times of my Ph.D. I will never forget his kind words of enquiry "kuch result aa raha hain?" almost on a daily basis. I also thank him for sharing his nanowire samples and e-beam resist for my sample fabrication tasks; and also for the nice figures he made for me in Adobe Illustrator.

Thanks to all the researchers in the MRFM community, especially, Dr. Daniel Rugar, Dr. John Mamin, Dr. John Marohn and Dr. Christian Degen for many scientific discussions and the sharing of technical information. I also express my heartfelt gratitude to Martino, Christian, John Marohn and John Mamin for providing me letters of recommendation and also for their advice in my search for a post-doc position.

Thanks to all the personnel of the mechanical workshop, especially Sascha Martin, Stefan Gentsch and Patrick Stöcklin, for providing us excellent machine parts. I thank Dominik Sifrig for the regular supply of Helium, sometimes, even with short notice.

I thank the secretaries - Germaine Weaver, Audrey Fischer, Barbara Kammermann and Astrid Kalt for always being nice and helpful with the administrative work.

The most important thing that helped me to keep my spirits up during the stressful days of my Ph.D. was the support extended by my wife Keerthana Sripada. I thank her for standing by me through thick and thin. She soaked up all the pressure I brought from the lab in those days when nothing worked in my favour. Without her emotional support, I couldn't have shown perseverance to obtain the scientific results reported in this thesis, which in turn helped me in securing a good postdoc position. I have worked for at least part of every weekend for many months during my Ph.D., especially in the final stages. I am grateful to her for being patient with me and it is time for us to take a well-deserved vacation.

My family members and in-laws always believed in my capabilities and encouraged me through good and bad times. I thank them for the constant love and affection they have shown towards me.

Finally, I thank the Almighty for giving me a wonderful life on this planet Earth. Not many people in this world are fortunate like me!

List of Symbols

Symbol	Unit	Quantity
\mathbf{B}_0	T	Total static magnetic field
$\mathbf{e}_x, \mathbf{e}_y, \mathbf{e}_z$	—	Unit vectors
\hbar	J · s	Reduced Planck's constant
i	—	Unit imaginary number
t	s	Time
$\hat{\boldsymbol{\mu}}$	J T ⁻¹	Total nuclear magnetic moment operator
$\hat{\mu}_x, \hat{\mu}_y, \hat{\mu}_z$	J T ⁻¹	Components of nuclear magnetic moment operator
γ	rad s ⁻¹ T ⁻¹	Gyromagnetic ratio
$\hat{\mathbf{I}}$	—	Nuclear spin angular momentum operator
$\hat{I}_x, \hat{I}_y, \hat{I}_z$	—	Components of nuclear spin angular momentum operator
ω_0	rad/s	Larmor frequency
\mathbf{B}_1	T	Rotating magnetic field
$\varphi(t)$	rad	Phase modulation of radio frequency field
\mathbf{B}_{eff}	T	Effective magnetic field
\mathbf{B}_{ext}	T	External magnetic field
\mathbf{B}_{tip}	T	Tip magnetic field
$\omega(t)$	rad/s	Instantaneous frequency
$\Delta\omega(t)$	rad/s	Instantaneous frequency modulation
G	T m ⁻¹	Magnetic field gradient
I	—	Nuclear spin quantum number
T	K	Temperature
k_B	J K ⁻¹	Boltzmann's constant
Ω_0	rad	Cantilever frequency
T_c	s	Cantilever period
N	—	Number of spins
τ_m	s	Spin correlation time

List of Figures

2.1	The effective field vector in a rotating frame	7
2.2	Description of the hyperbolic secant (HS) pulses for adiabatic inversion.	8
2.3	Configuration of the nuclear spin MRFM experiment	9
2.4	The magnetic field experienced by the spin.	11
2.5	The power spectral density of ^{31}P spin signal	18
2.6	Sketch of an ensemble of randomly polarized nuclear spins	19
2.7	Boltzmann and statistical polarization in an ensemble of N proton spins at $T = 0.4$ K and $B = 4$ T	22
2.8	Net polarized spins in an ensemble of N proton spins at $T = 0.4$ K and $B = 4$ T	23
2.9	The probability distribution of a nuclear spin ensemble containing $N = 10000$ protons	25
3.1	The power spectrum of the thermal displacement of the cantilever	29
3.2	The power spectrum of the damped motion of the cantilever	30
3.3	The power spectrum of the driven motion of the cantilever	31
4.1	Photograph of the probe	34
4.2	Zoom-in photograph of the probe	35
4.3	Fiber-optic interferometer diagram	36
4.4	Flow-chart description of the magnetic resonance force microscope setup	38
4.5	Diagram of the electrical circuit for generation of the RF waveform	40
4.6	A PID controller to tune the temperature of the laser	42
4.7	A PID controller to self-oscillate the cantilever to a set amplitude	43
4.8	An optimal controller to damp the cantilever Q	44
4.9	A bank of moving-average filters to filter the spin noise and thermal noise	45
4.10	A frequency counter to measure the cantilever period in real-time	46
4.11	A trigger generator to generate a digital trigger every N cantilever cycles	47
4.12	A pulse generator to send a digital trigger pulse to the waveform generator	47
5.1	SEMs of a representative InP NW	50
5.2	SEM of the InP NWs on the cantilever tip	50

5.3	SEMs of the GaP NW on the cantilever tip	51
5.4	Schematic of the experimental geometry	52
5.5	SEM micrograph of the Si cantilever	53
5.6	SEM micrograph of the microwire	54
5.7	MRFM signal from the statistical polarization of ^{31}P nuclear spins	55
5.8	MRFM signal from the statistical polarization of ^1H nuclear spins	55
5.9	Cyclic adiabatic rapid passage (ARP) pulse sequence	56
5.10	MRFM signal processing scheme	57
5.11	A typical time trace of the spin noise simulation of an ensemble of 10000 spins	58
5.12	Spin noise measurement from an ensemble of ^{31}P spins in an InP NW	59
5.13	Distribution of the natural spin and thermal cantilever fluctuations	59
5.14	Real-time communication among the measurement hardware.	60
5.15	Pulse sequence showing a π -inversion	60
5.16	Timing diagram for the π -inversion protocol	61
5.17	A time-trace of the hyper-polarized spin fluctuations	61
5.18	A time-trace of the narrowed spin fluctuations	62
5.19	Distributions of the non-equilibrium spin fluctuations	62
5.20	Capture-store-readout pulse sequence.	63
5.21	Ensemble average of measurement data over 100 CSR pulse sequences	64
5.22	Time trace showing an individual capture-store-readout sequence	65
5.23	Decay of ^{31}P polarization in the laboratory frame as a function of the storage time	66
5.24	Decay of ^1H polarization in the laboratory frame as a function of the storage time	66
5.25	Sketch of the electron-nuclear spin system	68
5.26	Ensemble averaged standard deviation of measurement data over 100 CSR pulse sequences	69
6.1	Magnetic tips for magnet-on-cantilever MRFM experiments	72
6.2	SEM micrograph of the microcoil	74

Abstract

Over the past few years, a wide variety of nuclear spin preparation techniques using hyperfine interaction-mediated dynamics have been developed in systems including gate-defined double quantum dots, self-assembled single quantum dots and nitrogen-vacancy centers in diamond. Here, we present a novel approach to nuclear spin state preparation by harnessing the naturally occurring stochastic fluctuations in nanoscale ensembles of nuclear spins in a semiconductor nanowire. Taking advantage of the excellent sensitivity of magnetic resonance force microscopy (MRFM) to monitor the $1/\sqrt{N}$ statistical polarization fluctuations in samples containing very few nuclear spins, we develop real-time spin manipulation protocols that allow us to measure and control the spin fluctuations in the rotating frame. We focus on phosphorus and hydrogen nuclear spins associated with an InP and a GaP nanowire and their hydrogen-containing adsorbate layers. The weak magnetic moments of these spins can be detected with high spatial resolution using the outstanding sensitivity of MRFM. Recently, MRFM has been used to image the proton spin density in a tobacco mosaic virus with a sensitivity reaching up to 100 net polarized spins. We describe how MRFM together with real-time radio frequency (RF) control techniques can also be used for the hyperpolarization, narrowing and storage of nuclear spin fluctuations and discuss how such nuclear spin states could potentially be harnessed for applications in magnetic resonance and quantum information processing.

In addition to presenting the experimental results on nuclear spin order, the theory of nuclear spin resonance and nanomechanical resonators is briefly discussed. The physical concepts explained provide the necessary background for the understanding of our MRFM experiments. The MRFM experimental apparatus, both sample-on-cantilever and magnet-on-cantilever, is also presented in considerable detail.

Chapter 1

Introduction

The weak magnetism of nuclear spins can be observed by polarizing them in a large external magnetic field. In thermal equilibrium, this results in an average macroscopic magnetization (or polarization) directed along the applied field, where the spin states are populated according to the Boltzmann distribution. The nuclear spin system can then be manipulated with a series of radio frequency (RF) pulses to extract the desired spectroscopic and structural information about the studied sample. However, the spin system at equilibrium also exhibits random magnetization fluctuations, the so-called “spin noise” [1], which can be detected continuously in time. The spin noise can be observed without the application of RF pulses and the fluctuations exist along any random direction in space. However, the noise signals are weaker compared to the mean signal obtained from Boltzmann population difference in large nuclear spin ensembles ($N > 10^{10}$).

Recently, the study of small-scale nuclear spin systems ($N \sim 10^4 - 10^6$) has gained importance for understanding electron spin decoherence in solid-state quantum systems and for application in nanoscale magnetic sensing and magnetometry [2–6]. The stochastic spin polarization fluctuations, resulting from random spin flips, typically exceeds the thermal polarization in such small spin ensembles. These fluctuations have random amplitude and phase and have been observed in a wide variety of nuclear spin systems in the solid-state using a superconducting interference device (SQUID) [7], by force-detected magnetic resonance [8], or by nitrogen-vacancy (NV) magnetometry [9, 15]. The ability to control and mitigate these nuclear spin fluctuations might find application in nanoscale magnetic resonance imaging and quantum information processing (QIP). We describe a method to harness the naturally occurring statistical fluctuations in small ensembles of nuclear spins by applying RF electro-magnetic pulses. The experimental work reported in this thesis deals with harnessing the spin fluctuations in a semiconductor nanowire sample using the technique of magnetic resonance force microscopy (MRFM).

Magnetic resonance force microscopy, the mechanical detection of electron or nuclear magnetic moments using an ultra-soft nanomechanical resonator, is a scanning probe technique actively pursued to push the limits of nuclear magnetic resonance (NMR) detection in nanoscale samples [10–14]. With this technique, we can probe ensembles containing few nuclear spins and measure the spin fluctuations in real-time. Detection of the magnetic fields of statistically polarized nuclei is demonstrated recently for very small ensembles of proton spins extrinsic to a diamond lattice using an intrinsic nitrogen vacancy center electron spin [9, 15]. Rather in MRFM, we detect the longitudinal component of the statistical nuclear magnetization of the ensemble in the rotating frame using the technique of adiabatic rapid passage (ARP).

Application in quantum information processing

Spin states of an electron can serve as a two-level quantum system or a qubit for encoding the quantum information. Advances in nanofabrication technology have allowed us to practically realize such spin qubits in a variety of systems including gate-defined quantum dots, optically active self-assembled quantum dots, nitrogen vacancy defects in diamond and phosphorous defects in silicon. Control over the electron spin states has been achieved either through electrical and/or optical means. However, a solid-state electron spin qubit typically interacts with its surrounding mesoscopic ensemble of nuclear spins in the host lattice through the hyperfine interaction [16, 17]. This interaction mechanism is the leading source of decoherence and relaxation for an electron spin qubit, hindering its application in quantum computation scenarios. Several methods such as complete polarization or narrowing of the nuclear spin ensemble have been proposed in order to address this issue. These proposals have been realized in systems like quantum dots using an optical or electrical readout of the nuclear hyperfine magnetic field [18–22]. Here we demonstrate a similar control over a nanoscale ensemble of spins using the mechanical readout of MRFM. We employ the exceptional sensitivity of MRFM to perform real-time measurement and control of an ensemble containing $10^4 - 10^6$ nuclear spins in a semiconductor nanowire. We create hyperpolarized and narrowed nuclear spin states by harnessing the statistical fluctuations of the ensemble [23]. Furthermore, we capture large nuclear spin polarization fluctuations, store them for many seconds, and read the polarization out.

Application in nanoscale magnetic resonance

MRFM overcomes the sensitivity limitations of conventional NMR to enable high spatial resolution detection of nuclear spins in nanoscale sample volumes in two ways: first, MRFM relies on the detection of statistical polarization and the power signal-to-noise ratio (SNR) is proportional to the number of spins in the sample. Second, for small ensembles of spins, nanomechanical resonators offer excellent detection sensitivity compared to electrical resonators and the measured signals are comparatively large [24].

State-of-the-art MRFM relies on the detection of randomly varying statistical polarization of the nuclear spins in the detection volume whereas conventional inductively detected magnetic resonance involves the detection of thermal (Boltzmann) polarization induced by the magnetic field. For small slice volumes, the fluctuating polarization becomes strong and it becomes more natural to consider using the fluctuations as the “signal” [25]. Here we show that mechanically detected NMR can be used to capture and create hyperpolarized states from random fluctuations in nanoscale nuclear spin ensembles [23]. Once captured, these fluctuations can then be used to initialize the polarization of nanoscale spin ensembles with a fixed sign and magnitude. Such initialization schemes could provide the basis for enhancing signals from small samples and for realizing advanced pulse protocols which can be borrowed directly from conventional NMR. We also demonstrate the long-term storage of large polarization fluctuations in nanoscale nuclear spin ensembles. Finally, we note that the only prerequisite for the proposed polarization capture and storage technique is the ability to detect nuclear spin polarization in real-time, which makes it applicable in a wide range of structures beyond nanowires.

Chapter 2

Spin Physics

This Chapter provides a theoretical description of the interaction of nuclear spins in a magnetic field (Section 2.1 and 2.2). The concept of adiabatic inversion of nuclear spin states is briefly described with quantum mechanical equations of motion (Section 2.2). The cyclic nuclear spin inversions occurring in a magnetic field gradient gives rise to an oscillating force on the cantilever (Section 2.3). The problem of relaxation of a nuclear spin resulting from its perturbative coupling to the thermal bath of the cantilever is studied (Section 2.4). A Markovian model for spin relaxation is described in detail (Section 2.5). The concepts of statistical polarization and distribution of nuclear spins are briefly revisited (Section 2.6). All these physical concepts discussed in this chapter provide the conceptual basis for the understanding of nuclear spin detection by magnetic resonance force microscopy (MRFM) technique.

2.1 Spin in a static magnetic field

The Schrödinger equation for a nuclear spin in a static field $\mathbf{B}_0 = B_0 \mathbf{e}_z$ is [26]

$$\begin{aligned} -\frac{\hbar}{i} \frac{\partial}{\partial t} |\Psi\rangle &= -\hat{\boldsymbol{\mu}} \cdot \mathbf{B}_0 |\Psi\rangle \\ &= -\gamma \hbar B_0 \hat{I}_z |\Psi\rangle \end{aligned} \quad . \quad (2.1)$$

We can formally solve (2.1) as $|\Psi(t)\rangle = e^{i\omega_0 t \hat{I}_z} |\Psi(0)\rangle$ where $\omega_0 = \gamma B_0$ is the Larmor frequency. We can compute the expectation value of the observable $\hat{\mu}_z$, the z -component of magnetic moment by means of $|\Psi(t)\rangle$. We have

$$\begin{aligned} \langle \hat{\mu}_z(t) \rangle &= \langle \Psi(t) | \hat{\mu}_z | \Psi(t) \rangle \\ &= \gamma \hbar \langle \Psi(0) | e^{-i\omega_0 t \hat{I}_z} \hat{I}_z e^{i\omega_0 t \hat{I}_z} | \Psi(0) \rangle \end{aligned} \quad . \quad (2.2)$$

We shall employ the useful relations listed below to perform the transformations [26].

$$\begin{aligned}
e^{-i\vartheta\hat{I}_z}\hat{I}_ze^{i\vartheta\hat{I}_z} &= \hat{I}_z \\
e^{-i\vartheta\hat{I}_z}\hat{I}_ye^{i\vartheta\hat{I}_z} &= -\hat{I}_x\sin\vartheta + \hat{I}_y\cos\vartheta \\
e^{-i\vartheta\hat{I}_z}\hat{I}_xe^{i\vartheta\hat{I}_z} &= \hat{I}_x\cos\vartheta + \hat{I}_y\sin\vartheta
\end{aligned} \tag{2.3}$$

Using (2.3) gives us $\langle\hat{\mu}_z(t)\rangle = \gamma\hbar\langle\Psi(0)|\hat{I}_z|\Psi(0)\rangle$ which is independent of time. Similarly we find

$$\begin{aligned}
\langle\hat{\mu}_y(t)\rangle &= -\langle\hat{\mu}_x(0)\rangle\sin\omega_0t + \langle\hat{\mu}_y(0)\rangle\cos\omega_0t \\
\langle\hat{\mu}_x(t)\rangle &= \langle\hat{\mu}_x(0)\rangle\cos\omega_0t + \langle\hat{\mu}_y(0)\rangle\sin\omega_0t
\end{aligned} \tag{2.4}$$

Both $\langle\hat{\mu}_y(t)\rangle$ and $\langle\hat{\mu}_x(t)\rangle$ oscillate in time at the Larmor frequency ω_0 . The equation of motion of the spin $\langle\hat{\mu}(t)\rangle$ is also given by

$$\langle\dot{\hat{\mu}}(t)\rangle = (\langle\hat{\mu}(0)\rangle \cdot \mathbf{e}_z)\mathbf{e}_z + [\langle\hat{\mu}(0)\rangle - (\langle\hat{\mu}(0)\rangle \cdot \mathbf{e}_z)\mathbf{e}_z]\cos\omega_0t + \{[\langle\hat{\mu}(0)\rangle - (\langle\hat{\mu}(0)\rangle \cdot \mathbf{e}_z)\mathbf{e}_z] \times \mathbf{e}_z\}\sin\omega_0t \tag{2.5}$$

In the simplest case of spin-1/2 systems, the eigenstates of operator \hat{I}_z may be denoted by $|\uparrow_z\rangle$ and $|\downarrow_z\rangle$ with eigenvalues $\pm 1/2$. The eigenstates $|\uparrow_n\rangle, |\downarrow_n\rangle$ of $\hat{\mathbf{I}} \cdot \mathbf{e}_n$, where \mathbf{e}_n is a unit vector lying in the xyz-plane that makes a polar angle θ with the positive z-axis and an azimuthal angle ϕ with the positive-x axis, are given by [27]

$$\begin{aligned}
|\uparrow_n\rangle &= \cos\frac{\theta}{2}|\uparrow_z\rangle + e^{i\phi}\sin\frac{\theta}{2}|\downarrow_z\rangle \\
|\downarrow_n\rangle &= \sin\frac{\theta}{2}|\uparrow_z\rangle - e^{i\phi}\cos\frac{\theta}{2}|\downarrow_z\rangle
\end{aligned} \tag{2.6}$$

We have [27]

$$\begin{aligned}
\hat{I}_y &= -\frac{i}{2} [|\uparrow_z\rangle\langle\downarrow_z| - |\downarrow_z\rangle\langle\uparrow_z|] \\
\hat{I}_x &= \frac{1}{2} [|\uparrow_z\rangle\langle\downarrow_z| + |\downarrow_z\rangle\langle\uparrow_z|]
\end{aligned} \tag{2.7}$$

If the spin is in the eigenstate $|\Psi(0)\rangle = |\uparrow_n\rangle$ at $t = 0$ so that $\langle\hat{\mu}_z(0)\rangle = \frac{\gamma\hbar}{2}\cos\theta$, $\langle\hat{\mu}_y(0)\rangle = \frac{\gamma\hbar}{2}\sin\theta\sin\phi$ and $\langle\hat{\mu}_x(0)\rangle = \frac{\gamma\hbar}{2}\sin\theta\cos\phi$, we get

$$\begin{aligned}
\langle\hat{\mu}_z(t)\rangle &= \frac{\gamma\hbar}{2}\cos\theta \\
\langle\hat{\mu}_y(t)\rangle &= \frac{\gamma\hbar}{2}\sin\theta\sin(-\omega_0t + \phi) \\
\langle\hat{\mu}_x(t)\rangle &= \frac{\gamma\hbar}{2}\sin\theta\cos(-\omega_0t + \phi)
\end{aligned} \tag{2.8}$$

We see that $\langle\hat{\mu}(t)\rangle$ behaves as does a vector, which precesses at an angular velocity $\boldsymbol{\Omega} = -\gamma B_0\mathbf{e}_z$ with respect to the laboratory frame, making a fixed angle θ with the z-direction. The equation of motion of the expectation

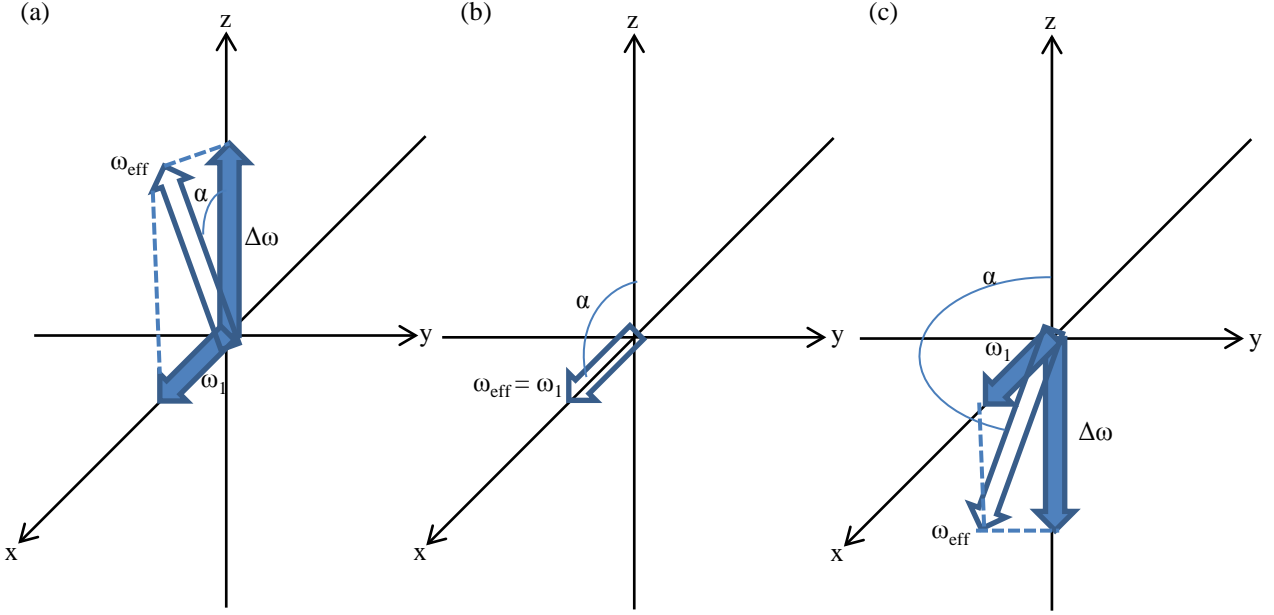


Figure 2.1: The effective field vector $\boldsymbol{\omega}_{\text{eff}} = \gamma \mathbf{B}_{\text{eff}}$ and its components, $\Delta\omega(t)$ and $\omega_1(t) = \gamma B_1(t)$, in a rotating frame of reference. The three conditions shown correspond to (a) far below resonance ($\omega(t) < \omega_0$, $\Delta\omega(t) \gg \omega_1(t)$), (b) at resonance ($\omega(t) = \omega_0$, $\Delta\omega(t) = 0$), and (c) far above resonance ($\omega(t) > \omega_0$, $-\Delta\omega(t) \gg \omega_1(t)$).

value is [26]

$$\frac{d\langle \hat{\boldsymbol{\mu}} \rangle}{dt} = \langle \hat{\boldsymbol{\mu}} \rangle \times \gamma \mathbf{B}_0 \quad . \quad (2.9)$$

2.2 Spin in a rotating magnetic field

We shall consider a radio frequency (RF) field

$$\mathbf{B}_1(t) = B_1(t) [\cos(\omega t - \varphi(t)) \mathbf{e}_x - \sin(\omega t - \varphi(t)) \mathbf{e}_y] \quad (2.10)$$

in addition to the static field $B_0 \mathbf{e}_z$ [28, 29]. The Schrödinger equation of motion of a nuclear spin including the effects of both the fields is [26]

$$-\frac{\hbar}{i} \frac{\partial}{\partial t} |\Psi\rangle = -\gamma \hbar \left[B_0 \hat{I}_z + B_1(t) (\hat{I}_x \cos(\omega t - \varphi(t)) - \hat{I}_y \sin(\omega t - \varphi(t))) \right] |\Psi\rangle \quad . \quad (2.11)$$

By using (2.3) of the preceding section, we can write the equation (2.11) as

$$-\frac{\hbar}{i} \frac{\partial}{\partial t} |\Psi\rangle = -\gamma \hbar \left[B_0 \hat{I}_z + B_1(t) e^{i(\omega t - \varphi(t)) \hat{I}_z} \hat{I}_x e^{-i(\omega t - \varphi(t)) \hat{I}_z} \right] |\Psi\rangle \quad . \quad (2.12)$$

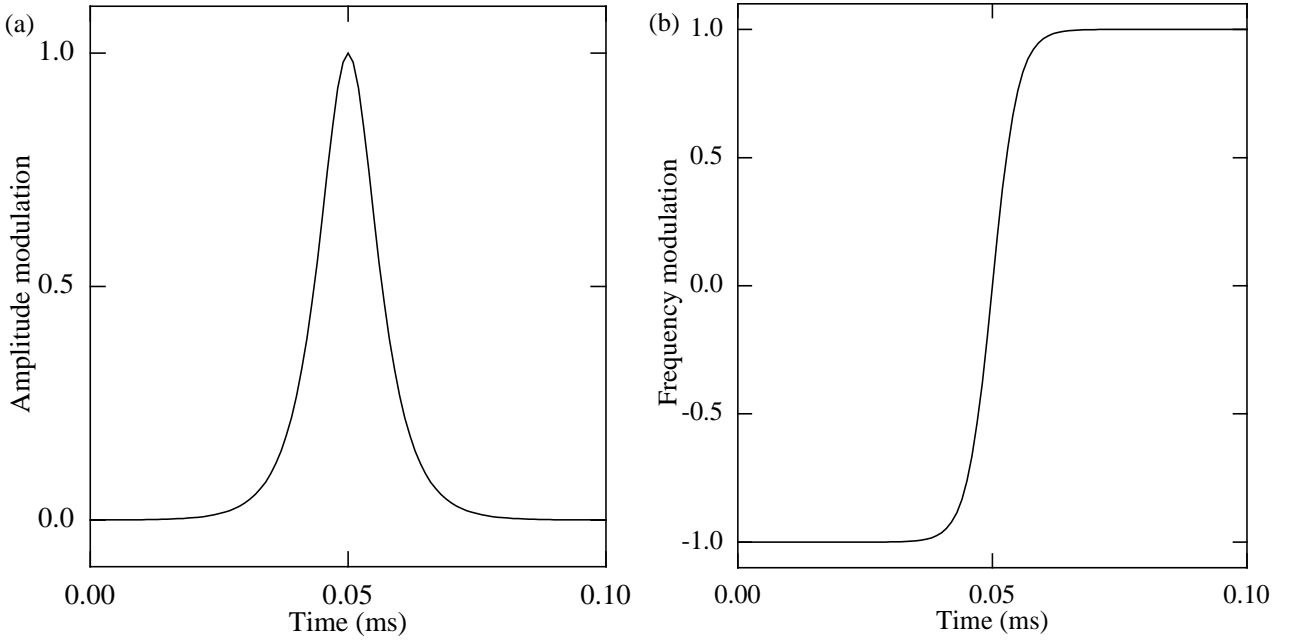


Figure 2.2: Description of the hyperbolic secant (HS) pulses for adiabatic inversion. (a) Amplitude dependence versus time $\frac{B_1(t)}{B_1} = A(t) = \frac{1}{\cosh(\beta(\frac{4t}{T_c}-1))}$, and (b) the frequency sweep $\frac{\Delta\omega(t)}{\Delta\omega} = \frac{\tanh(\beta(\frac{4t}{T_c}-1))}{\tanh\beta}$. $\frac{T_c}{2} = 0.1$ ms and $\beta = 10$ where T_c is one cantilever cycle and β is truncation factor.

The time dependence of \mathbf{B}_1 can be eliminated by moving to a frame rotating with the RF field by making the transformations

$$\begin{aligned} |\Psi\rangle &= e^{i(\omega t - \varphi(t))\hat{I}_z} |\tilde{\Psi}\rangle \\ \frac{\partial}{\partial t} |\Psi\rangle &= i(\omega - \dot{\varphi}(t))\hat{I}_z e^{i(\omega t - \varphi(t))\hat{I}_z} |\tilde{\Psi}\rangle + e^{i(\omega t - \varphi(t))\hat{I}_z} \frac{\partial}{\partial t} |\tilde{\Psi}\rangle \end{aligned} \quad (2.13)$$

Substituting (2.13) into (2.12) and multiplying both sides from the left by $e^{-i(\omega t - \varphi(t))\hat{I}_z}$, we obtain

$$-\frac{\hbar}{i} \frac{\partial}{\partial t} |\tilde{\Psi}\rangle = -\gamma\hbar \left[\left(B_0 + \frac{\dot{\varphi}(t) - \omega}{\gamma} \right) \hat{I}_z + B_1(t)\hat{I}_x \right] |\tilde{\Psi}\rangle \quad (2.14)$$

With such a transformation, (2.14) means that in the rotating frame, the spin acts as though it experiences effectively a magnetic field $\mathbf{B}_{\text{eff}}(t) = \left(B_0 + \frac{\dot{\varphi}(t) - \omega}{\gamma} \right) \mathbf{e}_z + B_1(t)\mathbf{e}_x$. Defining the instantaneous frequency as $\omega(t) = \omega - \dot{\varphi}(t)$ and the instantaneous frequency modulation as $\Delta\omega(t) = \omega_0 - \omega(t)$, the effective magnetic field is simply

$$\mathbf{B}_{\text{eff}}(t) = \frac{\Delta\omega(t)}{\gamma} \mathbf{e}_z + B_1(t)\mathbf{e}_x \quad (2.15)$$

In the MRFM technique, the frequency modulation of the external RF magnetic field causes the periodic reversals of the effective magnetic field acting on the nuclear spins (Fig. 2.1, Fig. 2.2 and Fig. 2.3). If the conditions of adiabatic motion are satisfied $(|\gamma B_{\text{eff}}(t)| \gg \left| \frac{d\alpha(t)}{dt} \right|)$ where $\tan \alpha(t) = \frac{\gamma B_1(t)}{\Delta\omega(t)}$ [30], the nuclear spins in the sample

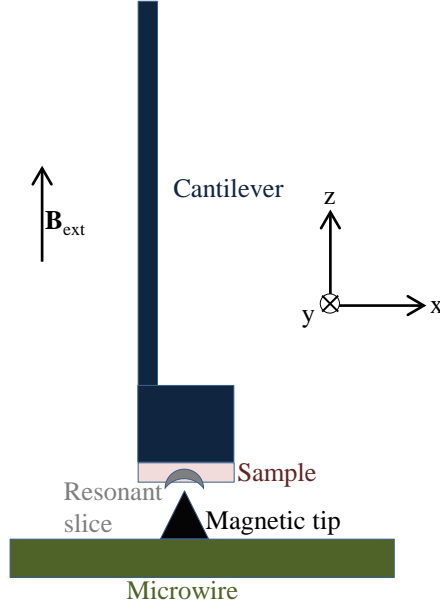


Figure 2.3: Configuration of the nuclear spin MRFM experiment. The sample (containing nuclear spins) at the end of an ultrasensitive silicon cantilever is positioned approximately 100 nm above the magnetic tip. The resonant slice represents those points in the sample where the field from the magnetic tip \mathbf{B}_{tip} (plus an external field \mathbf{B}_{ext}) matches the condition for magnetic resonance $\mathbf{B}_0 = \mathbf{B}_{\text{ext}} + \mathbf{B}_{\text{tip}} = \frac{\omega(t)}{\gamma}$. As the external RF magnetic field is frequency modulated, the resonant slice swings back and forth through the sample causing cyclic adiabatic inversion of the nuclear spins. The cyclic spin inversions causes a slight shift of the cantilever amplitude owing to the magnetic force exerted by the spins on the cantilever.

attached to the cantilever tip follow the effective magnetic field. The forces due to the nuclear spin inversions in a magnetic field gradient acting on the cantilever cause a small change in the amplitude of its vibrations.

2.3 Spin in a magnetic field gradient

Here, a single spin is described as a classical object obeying the classical equations of motion. In general, the magnetic field \mathbf{B}_{tip} produced by the magnetic tip has an arbitrary magnitude and orientation with respect to the external magnetic field $\mathbf{B}_{\text{ext}} = B_{\text{ext}}\mathbf{e}_z$ acting on the spin [31]. We assume that the magnetic moment of the spin $\boldsymbol{\mu}$ points initially in the direction of the magnetic field $\mathbf{B}_0 = \mathbf{B}_{\text{ext}} + \mathbf{B}_{\text{tip}}$. In a new system of coordinates $(\mathbf{e}_{\tilde{x}}, \mathbf{e}_{\tilde{y}}, \mathbf{e}_{\tilde{z}})$ whose \tilde{z} axis points in the direction of \mathbf{B}_0 , $\boldsymbol{\mu} = \mu_{\tilde{z}}\mathbf{e}_{\tilde{z}}$ and $\mathbf{B}_0 = B_0\mathbf{e}_{\tilde{z}}$. The nuclear magnetic moment in a magnetic field will possess a potential energy $E = -\boldsymbol{\mu} \cdot \mathbf{B}_0 = -\mu_{\tilde{z}}B_0$. The x -component of the magnetic force acting on the nuclear spin is $F_x = \mu_{\tilde{z}}\frac{\partial B_0}{\partial x}$. B_0 is obtained from $(B_{0,x}, B_{0,y}, B_{0,z})$ by an expression

$$\begin{aligned} B_0 &= B_{0,x} \cos \alpha_x + B_{0,y} \cos \alpha_y + B_{0,z} \cos \alpha_z \\ &= B_{\text{tip},x} \cos \alpha_x + B_{\text{tip},y} \cos \alpha_y + (B_{\text{ext}} + B_{\text{tip},z}) \cos \alpha_z \end{aligned} \quad (2.16)$$

where α_i ($i=x, y, z$) are the direction cosines relating $\mathbf{e}_{\tilde{z}}$ to \mathbf{e}_i . In the limit $B_{\text{ext}} \gg B_{\text{tip},i}$, $\mathbf{B}_0 \approx (B_{\text{ext}} + B_{\text{tip},z})\mathbf{e}_z$ and the gradient $G = \frac{\partial B_0}{\partial x} \approx \frac{\partial B_{\text{tip},z}}{\partial x}$.

Next we consider how the x, y, z components of the spin magnetic moment respond to the modulation of the effective field. The equation of motion for the nuclear spin in the rotating system of coordinates has the form $\frac{d\boldsymbol{\mu}}{dt} = \boldsymbol{\mu} \times \gamma \mathbf{B}_{\text{eff}}(t)$. We have

$$\begin{aligned}\dot{\mu}_x &= \Delta\omega(t)\mu_y \\ \dot{\mu}_y &= \gamma B_1(t)\mu_z - \Delta\omega(t)\mu_x \\ \dot{\mu}_z &= -\gamma B_1(t)\mu_y\end{aligned}\quad . \quad (2.17)$$

Assuming the conditions of adiabatic inversion, $\boldsymbol{\mu}$ quasistatically follows the effective field $\mathbf{B}_{\text{eff}}(t)$. Putting in (2.17) $\frac{d\boldsymbol{\mu}}{dt} = 0$, we obtain

$$\begin{aligned}\mu_x &= \frac{\gamma B_1(t)}{[(\Delta\omega(t))^2 + (\gamma B_1(t))^2]^{\frac{1}{2}}}\mu \\ \mu_y &= 0 \\ \mu_z &= \frac{\Delta\omega(t)}{[(\Delta\omega(t))^2 + (\gamma B_1(t))^2]^{\frac{1}{2}}}\mu\end{aligned}\quad . \quad (2.18)$$

2.4 Spin relaxation induced by a mechanical resonator

This section describes how the relaxation of nuclear spins is determined by the magnetic coupling to the thermal excitations of a cantilever [32–36]. The spins in the sample attached to the cantilever experience a magnetic field noise $\mathbf{B}_n(t) = Gx(t)\mathbf{e}_z$ due to the motion $x(t)$ of the cantilever. The total magnetic field at the position of the spin is $\mathbf{B}'_0(t) = \mathbf{B}_0 + \mathbf{B}_n(t)$. A circularly polarized RF field $\mathbf{B}_1(t) = B_1 [\cos\omega t\mathbf{e}_x - \sin\omega t\mathbf{e}_y]$ is applied in a direction perpendicular to \mathbf{B}_0 . Then, in the rotating reference frame that rotates with frequency ω , the spin experiences an effective magnetic field (Fig. 2.4)

$$\mathbf{B}'_{\text{eff}}(t) = \left(B_0 - \frac{\omega}{\gamma} + Gx(t) \right) \mathbf{e}_z + B_1 \mathbf{e}_x \quad . \quad (2.19)$$

The Hamiltonian of a spin in the rotating frame is

$$\mathcal{H}(t) = \mathcal{H}_0 + \mathcal{H}_1(t) \quad (2.20)$$

where

$$\begin{aligned}\mathcal{H}_0 &= -\hat{\boldsymbol{\mu}} \cdot \mathbf{B}_{\text{eff}} = -\gamma\hbar \left[\left(B_0 - \frac{\omega}{\gamma} \right) \hat{I}_z + B_1 \hat{I}_x \right] \text{ and} \\ \mathcal{H}_1(t) &= -\hat{\boldsymbol{\mu}} \cdot \mathbf{B}_n(t) = -\gamma\hbar Gx(t) \hat{I}_z\end{aligned}\quad . \quad (2.21)$$

Without any time-dependent perturbation, the spins are quantized along the effective field, the energy spacing

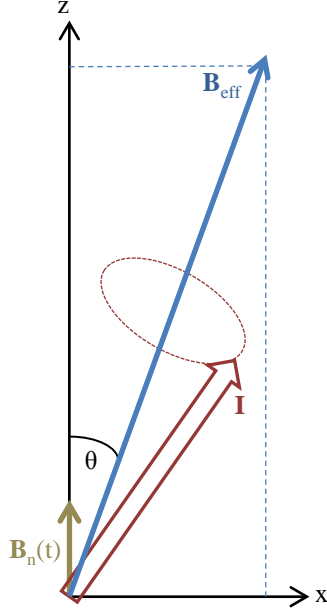


Figure 2.4: The magnetic field experienced by the spin.

$\hbar\omega_{\text{eff}}$ being

$$\hbar\omega_{\text{eff}} = \gamma\hbar B_{\text{eff}} = \gamma\hbar \left[\left(B_0 - \frac{\omega}{\gamma} \right)^2 + B_1^2 \right]^{\frac{1}{2}} . \quad (2.22)$$

Let the spin state at $t = 0$ is the energy eigenstate $|\uparrow_n\rangle$ where the polar angle θ is given by $\tan\theta = \frac{B_1}{B_0 - \frac{\omega}{\gamma}}$. We wish to find $C_{\uparrow_n}(t)$ and $C_{\downarrow_n}(t)$ such that

$$|\Psi(t)\rangle = C_{\uparrow_n}(t)e^{i\frac{\omega_{\text{eff}}}{2}t} |\uparrow_n\rangle + C_{\downarrow_n}(t)e^{-i\frac{\omega_{\text{eff}}}{2}t} |\downarrow_n\rangle \quad (2.23)$$

where $|\Psi(t)\rangle$ stands for the state ket at time t . The transition probability for $|\uparrow_n\rangle \rightarrow |\downarrow_n\rangle$ is obtained from the first-order time-dependent perturbation theory by $P_{\uparrow_n\downarrow_n}(t) = |C_{\downarrow_n}(t)|^2$ [27], where

$$\begin{aligned} C_{\downarrow_n}(t) &= -\frac{i}{\hbar} \int_0^t e^{i\omega_{\text{eff}}t'} \langle \downarrow_n | \mathcal{H}_1(t') | \uparrow_n \rangle dt' \\ &= i\gamma G \int_0^t e^{i\omega_{\text{eff}}t'} x(t') \langle \downarrow_n | \hat{I}_z | \uparrow_n \rangle dt' \\ &= \frac{i\gamma G \sin\theta}{2} \int_0^t e^{i\omega_{\text{eff}}t'} x(t') dt' \quad . \end{aligned} \quad (2.24)$$

The transition probability per unit time or the spin-flip relaxation rate is:

$$\begin{aligned} \frac{1}{T} &= \frac{d}{dt} (C_{\downarrow_n}(t)C_{\downarrow_n}^*(t)) \\ &= \left(\frac{d}{dt} C_{\downarrow_n}(t) \right) C_{\downarrow_n}^*(t) + C_{\downarrow_n}(t) \left(\frac{d}{dt} C_{\downarrow_n}^*(t) \right) \\ &= \left(\frac{\gamma G \sin\theta}{2} \right)^2 \left(e^{i\omega_{\text{eff}}t} x(t) \int_0^t e^{-i\omega_{\text{eff}}t'} x(t') dt' + e^{-i\omega_{\text{eff}}t} x(t) \int_0^t e^{i\omega_{\text{eff}}t'} x(t') dt' \right) \end{aligned}$$

$$= \left(\frac{\gamma G \sin \theta}{2} \right)^2 \left(\int_0^t e^{i\omega_{\text{eff}}(t-t')} x(t)x(t') dt' + \int_0^t e^{-i\omega_{\text{eff}}(t-t')} x(t)x(t') dt' \right) \quad (2.25)$$

Due to the random thermal (Brownian) motion $x(t)$ of the cantilever, it is possible to only calculate stochastic expectation values $\langle x(t)x(t') \rangle$. If the stochastic process is assumed to be stationary and $\tau = t' - t$, then

$$\begin{aligned} \frac{1}{T} &= \left(\frac{\gamma G \sin \theta}{2} \right)^2 \left(\int_{-t}^0 e^{-i\omega_{\text{eff}}\tau} \langle x(t)x(t+\tau) \rangle d\tau + \int_{-t}^0 e^{i\omega_{\text{eff}}\tau} \langle x(t)x(t+\tau) \rangle d\tau \right) \\ &= \left(\frac{\gamma G \sin \theta}{2} \right)^2 \left(\int_{-t}^t e^{-i\omega_{\text{eff}}\tau} \langle x(t)x(t+\tau) \rangle d\tau \right) \\ &\approx \left(\frac{\gamma G \sin \theta}{2} \right)^2 \left(\int_{-\infty}^{\infty} e^{-i\omega_{\text{eff}}\tau} \langle x(t)x(t+\tau) \rangle d\tau \right) \\ &= \left(\frac{\gamma G \sin \theta}{2} \right)^2 2\pi S_x(\omega_{\text{eff}}) \end{aligned} \quad (2.26)$$

The assumption of the approximate equality may be justified because the relevant times t can be significantly longer than the correlation time of the thermal motion. Therefore, the spectral density of the thermal cantilever motion at the Larmor frequency in the rotating frame determines the relaxation time T . Further analysis of the spin-flips induced by the magnetic coupling to the thermal excitation of the cantilever modes is identical to that presented in [32].

2.5 Spin relaxation - Kubo-Anderson model

In this section, a simplified mathematical model based on Kubo-Anderson type statistical fluctuations is developed to derive the power spectral density of the nuclear spin- I signal measured in magnetic resonance force microscopy (MRFM) is developed. The conclusion is that the line shape is Lorentzian-shaped. It is assumed that each spin switches energy levels in a random manner in time due to the interactions with the environment and the spectral width is estimated from this time variation.

The mathematical model assumes that the cyclically inverted moments giving rise to a periodic force on the cantilever undergo random, instantaneous jumps in time, because the interactions act to change the magnetic moment of the nuclear spin [37]. Assuming that the spin jumps are very rapid compared to the length of time between them, the random modulation of the magnetic moment is ‘‘Markoffian’’. This Markov model is solved by making the simplifying assumption that the jumps lead to a completely randomized magnetic moment distribution.

The nuclear spin fluctuations are accompanied by a change of a large number of microscopic degrees of freedom characterizing the reservoir. Therefore, the time interval between consecutive spin jumps must be many times

greater than the times that are necessary for the microscopic parameters to adjust to change of the nuclear spin energy. As on the time scale of spin jumps, the microscopic parameters can be considered as completely adjusted to the instantaneous value of the nuclear spin magnetic moment. For each jump, the spin exchanges its energy with the reservoir within a very short equilibration time. That is why the ‘spin’ forgets its previous history long before the next jump occurs, the probability of which depends therefore on its present position only. Thus, the jumping motion of spins is usually approximated as a Markov random process.

The fluctuations experienced by a nuclear spin can be modeled by a continuous-time discrete-state stochastic process with the set of allowed values for the random variable $\mathbf{m}(t)$ (nuclear spin quantum number) being $-I, -I + 1, \dots, I$ [38]. Suppose we observe this discrete-state process from time t_0 up to time t_k , and let $t_0 \leq t_1 \leq \dots \leq t_{k-1} \leq t_k$. The *observed* value m_k at t_k is the “present spin state” of the process, and m_0, m_1, \dots, m_{k-1} is its *observed* “past history”. Then, $\mathbf{m}_{k+1}, \mathbf{m}_{k+2}, \dots$, for time instants $t_{k+1} \leq t_{k+2} \leq \dots$, represents the unknown “future”. In a *Markov process*, the future is *conditionally* independent of the past history and the entire past history is summarized in the present spin state. This fact is referred to as the *memoryless property* since (a) all past spin state information is irrelevant, and (b) how long the spin has been in the current spin state is irrelevant, to probabilistically predict the future. The *Markov process* $\{\mathbf{m}(t)\}$ is formally defined as

$$P[\mathbf{m}(t_{k+1}) = m_{k+1} | \mathbf{m}(t_k) = m_k, \mathbf{m}(t_{k-1}) = m_{k-1}, \dots, \mathbf{m}(t_0) = m_0] = P[\mathbf{m}(t_{k+1}) = m_{k+1} | \mathbf{m}(t_k) = m_k] \quad (2.27)$$

for any $t_0 \leq t_1 \leq \dots \leq t_k \leq t_{k+1}$ where $P[\dots]$ is the conditional probability.

In a continuous-time process, spin transitions may occur at any time. We need to specify a transition probability matrix $\mathbf{P}(\tau)$ whose (i, j) th entry, $p_{ij}(\tau)$, is the probability of a transition from quantum state m_i to quantum state m_j within a time interval of duration τ for all possible τ . The time-dependent transition probabilities are defined as follows:

$$p_{ij}(t, s) \equiv P[\mathbf{m}(s) = m_j | \mathbf{m}(t) = m_i], \quad t \leq s \quad . \quad (2.28)$$

We will refer to $p_{ij}(t, s)$ as a transition function. For a homogeneous Markov process, all transition functions $p_{ij}(t, s)$ are independent of absolute time instants t, s , and depend only on the difference $\tau = s - t$. Then, homogeneity requires that, for any time t ,

$$p_{ij}(\tau) \equiv p_{ij}(t, t + \tau) = P[\mathbf{m}(t + \tau) = m_j | \mathbf{m}(t) = m_i] \quad . \quad (2.29)$$

The transition functions satisfy the *forward Chapman-Kolmogorov-Smoluchowski (CKS)* matrix differential equa-

tion

$$\frac{d\mathbf{P}(\tau)}{d\tau} = \mathbf{P}(\tau)\mathbf{Q} \quad (2.30)$$

where $\mathbf{Q} \equiv [q_{ij}]$ is called the *Transition Rate Matrix* of the Markov process. For any state i and time instant τ :

$$\sum_j p_{ij}(\tau) = 1 \quad (2.31)$$

since we are summing over all possible mutually exclusive events causing a transition from m_i to some new state. We also have the following initial conditions (assuming that a spin transition from any m_i to $m_j \neq m_i$ cannot occur in zero time):

$$p_{ij}(0) = \begin{cases} 1 & \text{if } m_j = m_i \\ 0 & \text{if } m_j \neq m_i \end{cases} . \quad (2.32)$$

The Poisson counting process is an essential building block in the stochastic modeling and analysis of Markov processes. The Poisson process counts events that occur in a very random but time-invariant way. The Poisson process possesses the memoryless property and is characterized by exponentially distributed interevent times (T) $P(T > t) = e^{-\lambda t}$ where λ is the average rate at which events occur per unit time. There is an useful result that the superposition of n independent Poisson processes, each possibly modelling a different event, with parameters $\lambda_i, i = 1, \dots, n$ is also a Poisson process with average rate parameter

$$\Lambda = \sum_{i=1}^n \lambda_i \quad . \quad (2.33)$$

Let T_i denote the amount of time spent at state m_i whenever this state is visited by the spin, which we also refer to as the spin dwell time. It is a fundamental property of continuous-time discrete-state Markov processes that the distribution of the spin dwell time $T_i, P[T_i > t], t \geq 0$, is exponential. Thus, $P(T_i > t) = e^{-\Lambda_i t}$ where $\Lambda_i > 0$ is a parameter generally dependent on the state m_i . This is a direct consequence of the memoryless property and in fact, there exists a close connection between Poisson counting processes and Markov processes. The interpretation of the parameter Λ_i is that it is the sum of the Poisson rates of all possible events which lead to a spin transition from state m_i . Each event is generated by a Poisson process with rate λ_{ij} which causes a spin transition from state m_i to state $m_j \neq m_i$. Then,

$$\Lambda_i = \sum_j \lambda_{ij} \quad . \quad (2.34)$$

The individual scalar differential equations for the CKS matrix equation are:

$$\frac{dp_{ij}(\tau)}{d\tau} = p_{ij}(\tau)q_{jj} + \sum_{r \neq j} p_{ir}(\tau)q_{ri} \quad . \quad (2.35)$$

This is a set of $2I + 1$ equations for a fixed i . The matrix element q_{ii} represents the instantaneous rate at which a spin transition out of m_i takes place and satisfies the relation $q_{ii} = -\Lambda_i$. The interpretation of q_{ij} is the instantaneous rate at which a spin transition from m_i to m_j takes place and satisfies the relation $q_{ij} = \lambda_{ij}$. In addition, we have

$$\sum_j q_{ij} = 0 \quad . \quad (2.36)$$

Suppose spin transitions occur at random time instants $T_1 < T_2 < \dots < T_k < \dots$ and let the spin state following the transition at T_k is denoted by \mathbf{m}_k . The *transition probability*, P_{ij} , is defined as $P_{ij} = P[\mathbf{m}_{k+1} = m_j | \mathbf{m}_k = m_i]$ and is expressed in terms of elements of \mathbf{Q} as $P_{ij} = \frac{q_{ij}}{-q_{ii}}, j \neq i$. Moreover, we have

$$\sum_{j \neq i} P_{ij} = 1 \quad (2.37)$$

and $P_{ii} = 0$.

The spin state probability is defined as $\pi_j(t) \equiv P[\mathbf{m}(t) = m_j]$ and accordingly, we have a spin state probability vector $\boldsymbol{\pi}(t) = [\pi_0(t), \pi_1(t), \dots]$. A continuous-time discrete-state Markov process is completely specified by the state space m_0, m_1, \dots and the transition matrix $\mathbf{P}(\tau)$, and an initial spin state probability vector $\boldsymbol{\pi}(0)$ which provides the probability distribution of the initial spin state $\mathbf{m}(0)$. Using the rule of total probability, we can obtain a relationship in matrix form $\boldsymbol{\pi}(t) = \boldsymbol{\pi}(0)\mathbf{P}(t)$. The steady state solution of this equation is the stationary distribution or the equilibrium distribution to which the ensemble of our nuclear spins must approach starting from any arbitrary distribution.

The fundamental task is to calculate the probability of finding $\mathbf{m}(t)$ at state m at time t , that is, $P[\mathbf{m}(t) = m]$ to probabilistically assess which energy levels are more likely than others. The power spectrum of the spin signal is given by the Fourier transform

$$S(f) = \mathcal{F}[\langle \mu_z(t) \mu_z(t + \tau) \rangle] \quad (2.38)$$

where $\mu_z(t) = 2\mu m(t)$ is the time-dependent spin z -component. The problem is to find $S(f)$ under the assumption that $\boldsymbol{\mu}_z(t)$ is Markovian.

The simplest possible case is that of a nuclear spin with $I = \frac{1}{2}$ in which it has only two possible spin z -magnetic moment components, which we take to be $\pm\mu$, and these moments are equally probable so that

$P[\boldsymbol{\mu}(t) = \mu] = P[\boldsymbol{\mu}(t) = -\mu]$. The only possible “transition rate matrix” \mathbf{Q} for this case is

$$\mathbf{Q} = \begin{bmatrix} -\lambda & \lambda \\ \lambda & -\lambda \end{bmatrix} \quad (2.39)$$

where λ is a parameter specifying the rate at which jumping takes place back and forth between the two spin states.

In the case of spin- I , the magnetic moment spectrum consists of a series of $2I + 1$ equally spaced moments

$$\mu_i = -2I\mu, -2(I-1)\mu, \dots, 2(I-1)\mu, 2I\mu \quad . \quad (2.40)$$

Let us suppose that the possible z -magnetic moments of a nuclear spin are numbered as $\mu_1, \mu_2, \dots, \mu_{2I+1}$. In the simplest case, we say that transitions are equally likely to all other spin states (we assume a symmetrical \mathbf{Q} -matrix) [39, 40]

$$\mathbf{Q} = \begin{bmatrix} -\Lambda & \frac{\Lambda}{2I} & \frac{\Lambda}{2I} & \dots & \dots & \dots & \frac{\Lambda}{2I} \\ \frac{\Lambda}{2I} & -\Lambda & \frac{\Lambda}{2I} & \dots & \dots & \dots & \dots \\ \frac{\Lambda}{2I} & \frac{\Lambda}{2I} & -\Lambda & \dots & \dots & \dots & \dots \\ \dots & \dots & \dots & \dots & \dots & \dots & \dots \\ \dots & \dots & \dots & \dots & \dots & \dots & \dots \\ \dots & \dots & \dots & \dots & \dots & \dots & \dots \\ \frac{\Lambda}{2I} & \dots & \dots & \dots & \dots & \dots & -\Lambda \end{bmatrix} \quad . \quad (2.41)$$

The transition rate *from* each state is Λ . For a fixed i , equation 2.35 can be written in a more compact form

$$\frac{d\mathbf{p}_i(\tau)}{d\tau} = \mathbf{Q}\mathbf{p}_i(\tau) \quad (2.42)$$

where $\mathbf{p}_i(\tau)$ is a $(2I + 1)$ -dimensional transition function vector. To solve this differential equation is equivalent to find the eigenvalues and associated eigenvectors of the matrix \mathbf{Q} .

\mathbf{Q} is a $2I + 1 \times 2I + 1$ circulant matrix fully specified by one column vector \mathbf{q} . The eigenvalues of \mathbf{Q} are given by

$$\lambda_j = -\Lambda + \frac{\Lambda}{2I}\omega_j + \frac{\Lambda}{2I}\omega_j^2 + \dots + \frac{\Lambda}{2I}\omega_j^{2I}, \quad j = 0, 1, \dots, 2I \quad (2.43)$$

$$\lambda_j = \begin{cases} 0 & \text{if } j = 0 \\ -\Lambda \left(1 + \frac{1}{2I}\right) & \text{if } j \neq 0 \end{cases} \quad (2.44)$$

where $\omega_j = e^{i\frac{2\pi j}{2I+1}}$ are the $(2I+1)$ -th roots of unity. The corresponding orthonormal eigenvectors are given by

$$\Psi_j = \frac{1}{\sqrt{2I+1}} (1, \omega_j, \omega_j^2, \dots, \omega_j^{2I})^T \quad . \quad (2.45)$$

The block matrix \mathbf{U} that diagonalizes \mathbf{Q} is given by $(\Psi_0\Psi_1\dots\Psi_{2I})$ and is also unitary and orthogonal. Let the diagonal matrix be denoted by \mathbf{D} . The solution is given by [41]

$$\begin{aligned} \mathbf{p}_i(\tau) &= e^{\mathbf{Q}\tau} \mathbf{p}_i(0) \\ &= \mathbf{U} e^{\mathbf{D}\tau} \mathbf{U}^{-1} \mathbf{p}_i(0) \\ &= \mathbf{U} \begin{bmatrix} 1 & 0 & 0 & \dots & \dots & \dots & 0 \\ 0 & e^{-\Lambda(1+\frac{1}{2I})\tau} & 0 & \dots & \dots & \dots & \dots \\ 0 & 0 & e^{-\Lambda(1+\frac{1}{2I})\tau} & \dots & \dots & \dots & \dots \\ \dots & \dots & \dots & \dots & \dots & \dots & \dots \\ \dots & \dots & \dots & \dots & \dots & \dots & \dots \\ \dots & \dots & \dots & \dots & \dots & \dots & \dots \\ 0 & \dots & \dots & \dots & \dots & \dots & e^{-\Lambda(1+\frac{1}{2I})\tau} \end{bmatrix} \mathbf{U}^{-1} \mathbf{p}_i(0) \\ &= \mathbf{U} e^{-\Lambda(1+\frac{1}{2I})\tau} \mathbf{I} \mathbf{U}^{-1} \mathbf{p}_i(0) + \mathbf{U} \begin{bmatrix} 1 - e^{-\Lambda(1+\frac{1}{2I})\tau} & 0 & 0 & \dots & \dots & \dots & 0 \\ 0 & 0 & 0 & \dots & \dots & \dots & \dots \\ 0 & 0 & 0 & \dots & \dots & \dots & \dots \\ \dots & \dots & \dots & \dots & \dots & \dots & \dots \\ \dots & \dots & \dots & \dots & \dots & \dots & \dots \\ \dots & \dots & \dots & \dots & \dots & \dots & \dots \\ 0 & \dots & \dots & \dots & \dots & \dots & 0 \end{bmatrix} \mathbf{U}^{-1} \mathbf{p}_i(0) \quad . \quad (2.46) \end{aligned}$$

The transition function is given by

$$p_{ij}(\tau) = e^{-\Lambda(1+\frac{1}{2I})\tau} \delta_{ij} + \frac{1}{2I+1} (1 - e^{-\Lambda(1+\frac{1}{2I})\tau}) \quad . \quad (2.47)$$

Assuming a uniform distribution among the initial states $P[\mathbf{m}(0) = m_i] = \frac{1}{2I+1}$, the probability $P[\mathbf{m}(t) = m_j]$ is

$$\pi_j(t) = \sum_i p_{ij}(\tau) \pi_i(0) = \frac{1}{2I+1} \quad . \quad (2.48)$$

The spin state probabilities remain uniform at any later time. Using the Markov properties, the two-time autocorrelation function between the values of $\mu_z(t)$ at time t and time $t + \tau$ can be evaluated as

$$\langle \mu_z(t) \mu_z(t + \tau) \rangle = \sum_{i,j} \mu_i \mu_j P(\mu_i, t; \mu_j, t + \tau)$$

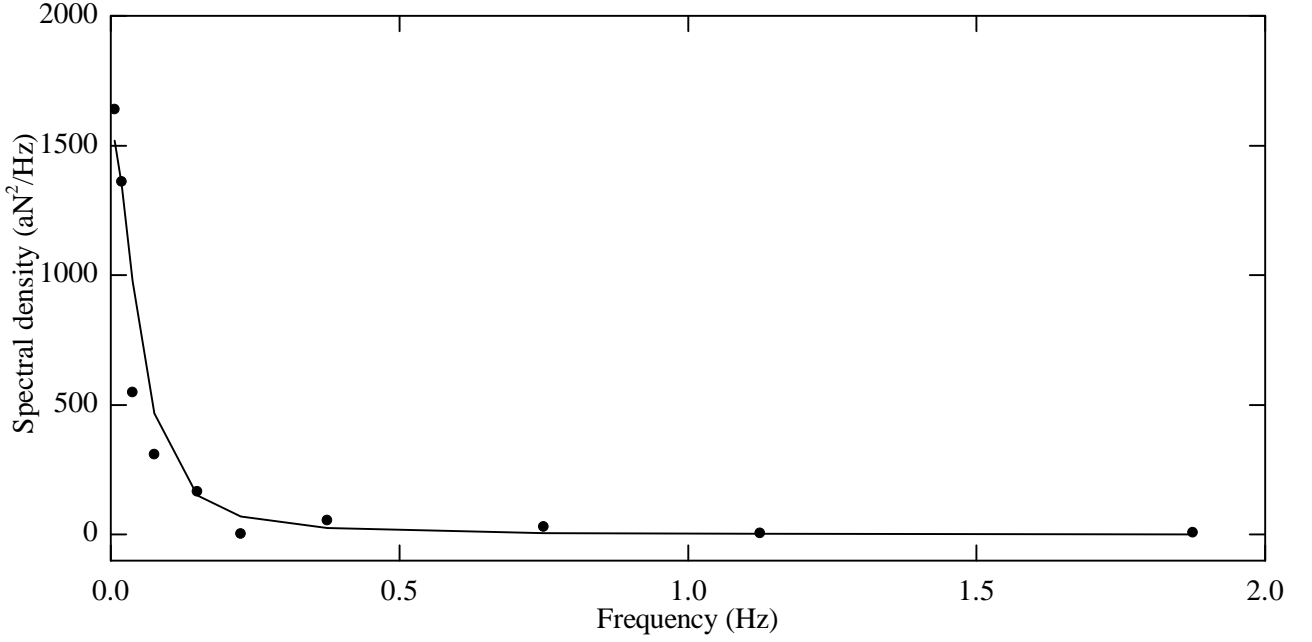


Figure 2.5: The power spectral density of a two minute record of ^{31}P spin fluctuations measured using MRFM technique. It fits well to a Lorentzian and the correlation time extracted from the fit is given by $\tau_m = 2.5$ s.

$$\begin{aligned}
&= \sum_{i,j} (2\mu m_i)(2\mu m_j) p_{ij}(\tau) \pi_i(t) \\
&= \frac{4\mu^2}{2I+1} \sum_{i,j} m_i m_j \left[e^{-\Lambda(1+\frac{1}{2I})\tau} \delta_{ij} + \frac{1}{2I+1} \left(1 - e^{-\Lambda(1+\frac{1}{2I})\tau} \right) \right] \\
&= \frac{4\mu^2}{2I+1} \left[e^{-\Lambda(1+\frac{1}{2I})\tau} \sum_i m_i^2 + \frac{1}{2I+1} \left(1 - e^{-\Lambda(1+\frac{1}{2I})\tau} \right) \sum_{i,j} m_i m_j \right] \\
&= \frac{4\mu^2 I(I+1)}{3} e^{-\Lambda(1+\frac{1}{2I})\tau}
\end{aligned} \tag{2.49}$$

which is a simple exponential in form. From the Wiener-Khinchin theorem, the single-sided power spectral density is the Fourier transform of the autocorrelation function (Fig. 2.5)

$$\begin{aligned}
S(f) &= 2 \int_{-\infty}^{\infty} d\tau e^{-i2\pi f\tau} \langle \mu_z(t) \mu_z(t+\tau) \rangle \\
&= \frac{4\mu^2 I(I+1)}{3} \frac{4\Lambda \left(1 + \frac{1}{2I} \right)}{\Lambda^2 \left(1 + \frac{1}{2I} \right)^2 + 4\pi^2 f^2}
\end{aligned} \tag{2.50}$$

It determines the connection between fluctuations in the value of $\mu_z(t)$ and the frequency distribution of the time variations of $\mu_z(t)$.

2.6 Spins - polarization and distribution

The volume of the resonant slice studied in our MRFM experiment is typically tiny ($\sim 100 \text{ nm}^3$) and contains $N \sim 10^4 - 10^6$ randomly oriented nuclear spins. For such small number of spins in the slice, the time-varying

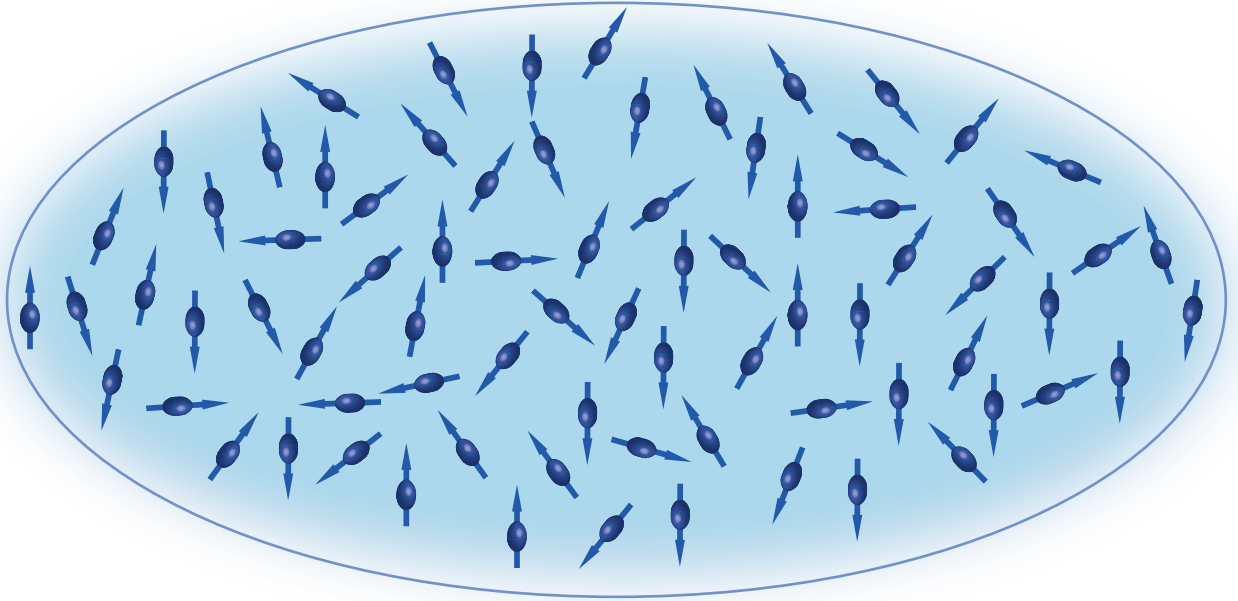


Figure 2.6: An ensemble of randomly polarized nuclear spins has a resultant magnetic moment because of statistically incomplete cancellation.

statistical fluctuations of the polarization generated by random spin flips far exceeds the mean Boltzmann polarization. This section describes the derivation of the statistical polarization and distribution of a nuclear spin ensemble using different methods (Fig. 2.6).

2.6.1 Multinomial distribution

Let us consider an ensemble containing N spin- I nuclei placed in a magnetic field B and is in thermodynamic equilibrium at a temperature T . For the sake of illustration, we shall consider nuclei with half-integer spin, i.e., $I = \frac{2k-1}{2}$ where k is a natural number. Each spin occupying a state j (ranging from $-\frac{2k-1}{2}$ to $\frac{2k-1}{2}$ in steps of one) possesses an energy $E_j = -2j\mu B$ where $\mu = \frac{\gamma\hbar}{2}$. Let the total number of spins N be divided among the $2I + 1$ spin states, so that $N = \sum_j N_j$ where N_j represents the occupation number of state j . The probability p_j of occupation of each state is determined by the Boltzmann factor

$$p_j = \frac{e^{-\frac{E_j}{k_B T}}}{2I + 1} \approx \frac{1}{2k} \left(1 + 2j \frac{\mu B}{k_B T} \right) \quad . \quad (2.51)$$

The vector random variable $\mathbf{N} = \left(N_{-\frac{2k-1}{2}}, \dots, N_j, \dots, N_{\frac{2k-1}{2}} \right)$ follows a multinomial distribution with parameters N and \mathbf{p} where $\mathbf{p} = (\dots, p_j, \dots)$ and $\sum_j p_j = 1$. The properties of the multinomial distribution such as the expected value, the variance and the covariance are given by

$$\begin{aligned} \mathbf{E}(N_j) &= p_j N \\ \text{Var}(N_j) &= p_j(1 - p_j)N \end{aligned} \quad (2.52)$$

$$\text{Cov}(N_i, N_j) = -p_i p_j N \quad .$$

The total magnetization ΔM of the ensemble is given by

$$\Delta M = \sum_{j=-\frac{2k-1}{2}}^{\frac{2k-1}{2}} 2j N_j \mu \quad . \quad (2.53)$$

The variance $\sigma_{\Delta M}^2$ of the typical magnetization fluctuations will be

$$\begin{aligned} \sigma_{\Delta M}^2 &= 4\mu^2 \left[\sum_{j=-\frac{2k-1}{2}}^{\frac{2k-1}{2}} j^2 \text{Var}(N_j) + \sum_{i=-\frac{2k-1}{2}}^{\frac{2k-1}{2}} \sum_{j \neq i, j=-\frac{2k-1}{2}}^{\frac{2k-1}{2}} ij \text{Cov}(N_i, N_j) \right] \\ &= 4N\mu^2 \left[\sum_{j=-\frac{2k-1}{2}}^{\frac{2k-1}{2}} j^2 p_j (1-p_j) - \sum_{i=-\frac{2k-1}{2}}^{\frac{2k-1}{2}} \sum_{j \neq i, j=-\frac{2k-1}{2}}^{\frac{2k-1}{2}} ij p_i p_j \right] \quad . \end{aligned} \quad (2.54)$$

Substituting equation (2.51) in the above equation, we get

$$\begin{aligned} \sigma_{\Delta M}^2 &= 4N\mu^2 \left[\sum_{j=-\frac{2k-1}{2}}^{\frac{2k-1}{2}} j^2 \frac{1}{2k} \left(1 + 2j \frac{\mu B}{k_B T} \right) \left(1 - \frac{1}{2k} \left(1 + 2j \frac{\mu B}{k_B T} \right) \right) \right. \\ &\quad \left. - \sum_{i=-\frac{2k-1}{2}}^{\frac{2k-1}{2}} \sum_{j \neq i, j=-\frac{2k-1}{2}}^{\frac{2k-1}{2}} ij \frac{1}{2k} \left(1 + 2i \frac{\mu B}{k_B T} \right) \frac{1}{2k} \left(1 + 2j \frac{\mu B}{k_B T} \right) \right] \\ &= 4N\mu^2 \left[\sum_{j=-\frac{2k-1}{2}}^{\frac{2k-1}{2}} j^2 \frac{1}{2k} \left(1 + 2j \frac{\mu B}{k_B T} - \frac{1}{2k} \left(1 + 2j \frac{\mu B}{k_B T} \right) \right) - \frac{1}{2k} 2j \frac{\mu B}{k_B T} - \frac{1}{2k} 4j^2 \left(\frac{\mu B}{k_B T} \right)^2 \right) \\ &\quad \left. - \sum_{i=-\frac{2k-1}{2}}^{\frac{2k-1}{2}} \sum_{j \neq i, j=-\frac{2k-1}{2}}^{\frac{2k-1}{2}} ij \frac{1}{(2k)^2} \left(1 + 2(i+j) \frac{\mu B}{k_B T} + 4ij \left(\frac{\mu B}{k_B T} \right)^2 \right) \right] \\ &= \frac{4N\mu^2}{(2k)^2} \left[\sum_{j=-\frac{2k-1}{2}}^{\frac{2k-1}{2}} j^2 \left((2k-1) + (2k-2)2j \frac{\mu B}{k_B T} - 4j^2 \left(\frac{\mu B}{k_B T} \right)^2 \right) \right. \\ &\quad \left. - \sum_{i=-\frac{2k-1}{2}}^{\frac{2k-1}{2}} \sum_{j \neq i, j=-\frac{2k-1}{2}}^{\frac{2k-1}{2}} \left(ij + 2(i^2 j + ij^2) \frac{\mu B}{k_B T} + 4(ij)^2 \left(\frac{\mu B}{k_B T} \right)^2 \right) \right] \\ &= \frac{N\mu^2}{k^2} \left[\left((2k-1) \sum_{j=-\frac{2k-1}{2}}^{\frac{2k-1}{2}} j^2 \right) + \left(4(k-1) \frac{\mu B}{k_B T} \sum_{j=-\frac{2k-1}{2}}^{\frac{2k-1}{2}} j^3 \right) \right. \\ &\quad \left. - \left(4 \left(\frac{\mu B}{k_B T} \right)^2 \sum_{j=-\frac{2k-1}{2}}^{\frac{2k-1}{2}} j^4 \right) - \left(\sum_{i=-\frac{2k-1}{2}}^{\frac{2k-1}{2}} i \left(\sum_{j \neq i, j=-\frac{2k-1}{2}}^{\frac{2k-1}{2}} j \right) \right) \right. \\ &\quad \left. - \left(4 \frac{\mu B}{k_B T} \sum_{i=-\frac{2k-1}{2}}^{\frac{2k-1}{2}} i^2 \left(\sum_{j \neq i, j=-\frac{2k-1}{2}}^{\frac{2k-1}{2}} j \right) \right) - \left(4 \left(\frac{\mu B}{k_B T} \right)^2 \sum_{i=-\frac{2k-1}{2}}^{\frac{2k-1}{2}} i^2 \left(\sum_{j \neq i, j=-\frac{2k-1}{2}}^{\frac{2k-1}{2}} j^2 \right) \right) \right] \quad . \end{aligned} \quad (2.55)$$

Noting that $\sum_{j=-\frac{2k-1}{2}}^{\frac{2k-1}{2}} j = 0$ and $\sum_{j=-\frac{2k-1}{2}}^{\frac{2k-1}{2}} j^3 = 0$, we can simplify the above expression as

$$\begin{aligned}
\sigma_{\Delta M}^2 &= \frac{N\mu^2}{k^2} \left[\left((2k-1) \sum_{j=-\frac{2k-1}{2}}^{\frac{2k-1}{2}} j^2 \right) - \left(4 \left(\frac{\mu B}{k_B T} \right)^2 \sum_{j=-\frac{2k-1}{2}}^{\frac{2k-1}{2}} j^4 \right) - \left(\sum_{i=-\frac{2k-1}{2}}^{\frac{2k-1}{2}} i(-i) \right) \right. \\
&\quad \left. - \left(4 \frac{\mu B}{k_B T} \sum_{i=-\frac{2k-1}{2}}^{\frac{2k-1}{2}} i^2(-i) \right) - \left(4 \left(\frac{\mu B}{k_B T} \right)^2 \sum_{i=-\frac{2k-1}{2}}^{\frac{2k-1}{2}} i^2 \left(\left(\sum_{j=-\frac{2k-1}{2}}^{\frac{2k-1}{2}} j^2 \right) - i^2 \right) \right) \right] \\
&= \frac{N\mu^2}{k^2} \left[\left(2k \sum_{j=-\frac{2k-1}{2}}^{\frac{2k-1}{2}} j^2 \right) - 4 \left(\frac{\mu B}{k_B T} \right)^2 \left(\sum_{j=-\frac{2k-1}{2}}^{\frac{2k-1}{2}} j^2 \right)^2 \right] \\
&= \frac{N\mu^2}{k^2} \left[2k \left(\frac{k(2k-1)(2k+1)}{6} \right) - 4 \left(\frac{\mu B}{k_B T} \right)^2 \left(\frac{k(2k-1)(2k+1)}{6} \right)^2 \right] \\
&= N\mu^2 \left[\frac{(2k-1)(2k+1)}{3} - \left(\frac{\mu B}{k_B T} \right)^2 \left(\frac{(2k-1)(2k+1)}{3} \right)^2 \right] \\
&= \frac{4I(I+1)N\mu^2}{3} \left[1 - \frac{4I(I+1)}{3} \left(\frac{\mu B}{k_B T} \right)^2 \right] \\
&= \frac{4I(I+1)N\mu^2}{3} \left[1 - \frac{\overline{\Delta M} B}{Nk_B T} \right] \tag{2.56}
\end{aligned}$$

where $\overline{\Delta M}$ is the thermal or Boltzmann magnetization.

2.6.2 Density matrix

Consider an ensemble of N spins with the spin quantum number I and the magnetic quantum numbers $m = -I, -I+1, \dots, I$. The ensemble has an instantaneous statistical magnetization excess ΔM due to the incomplete cancellation of the nuclear spin magnetic moments. The Hamiltonian of a single spin in the presence of a magnetic field B along the z -direction is

$$\mathcal{H} = -\hat{\mu}_z B = -2\mu B \hat{I}_z \tag{2.57}$$

where $\hat{\mu}_z$ is the z -component of the magnetic dipole moment operator; and the energies of the different spin states are no longer equal. Statistical mechanics predicts the equilibrium distribution at a temperature T to be a Boltzmann distribution over the energies of the spin states and the density matrix $\hat{\rho} = \frac{1}{Z} e^{-\frac{\mathcal{H}}{k_B T}}$ where $Z = \text{Tr}\{e^{-\frac{\mathcal{H}}{k_B T}}\}$ contains all the information about the nuclear spin polarization in the system [26, 42]. The density matrix of the spin system can be used to compute the mean $\overline{\Delta M}$ and the fluctuation variance $\sigma_{\Delta M}^2$

$$\begin{aligned}
\overline{\Delta M} &= N \text{Tr}\{\hat{\mu}_z \hat{\rho}\} \\
\sigma_{\Delta M}^2 &= N [\text{Tr}\{\hat{\mu}_z^2 \hat{\rho}\} - (\text{Tr}\{\hat{\mu}_z \hat{\rho}\})^2] \tag{2.58}
\end{aligned}$$

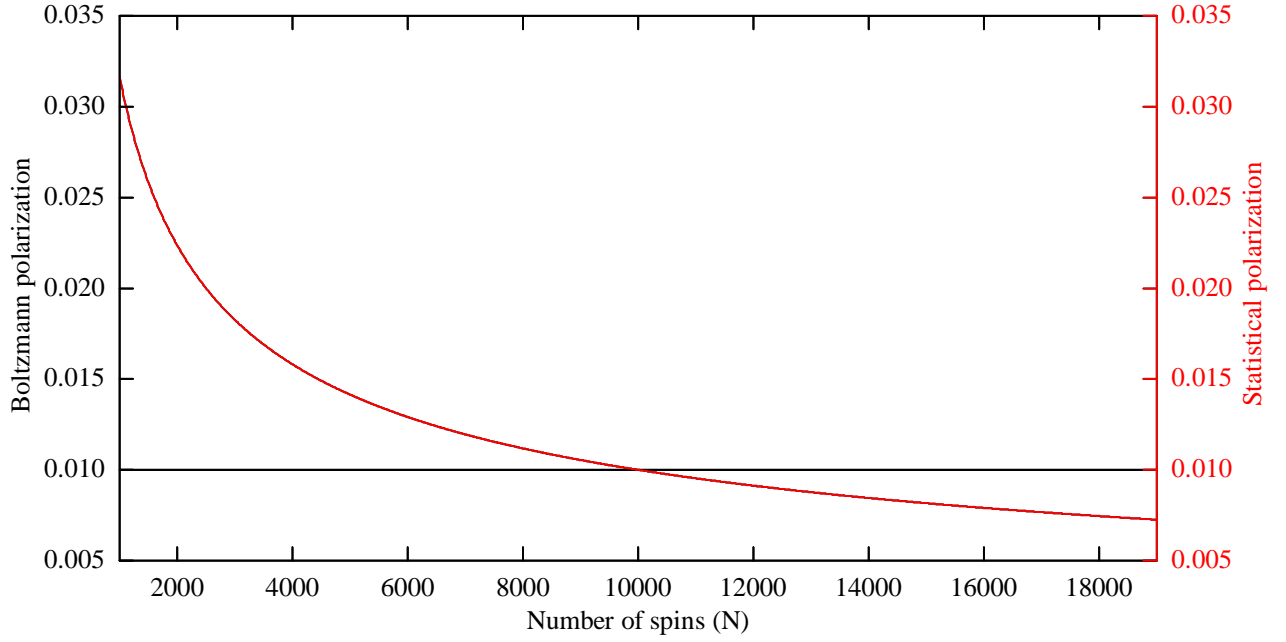


Figure 2.7: Boltzmann and statistical polarization in an ensemble of N proton spins at a temperature $T = 0.4$ K and a magnetic field $B = 4$ T.

of the z -magnetization. In the high-temperature limit, $Z = 2I + 1$ and

$$e^{-\frac{\mathcal{H}}{k_B T}} \approx \mathbf{1} - \frac{\mathcal{H}}{k_B T} = \mathbf{1} + 2 \left(\frac{\mu B}{k_B T} \right) \hat{I}_z \quad . \quad (2.59)$$

Since

$$\begin{aligned} \text{Tr}\{\hat{I}_z\} &= 0 \\ \text{Tr}\{\hat{I}_z^2\} &= \frac{I(I+1)(2I+1)}{3} \\ \text{Tr}\{\hat{I}_z^3\} &= 0 \end{aligned} \quad (2.60)$$

we have

$$\begin{aligned} \overline{\Delta M} &= \frac{4I(I+1)}{3} \left(\frac{\mu B}{k_B T} \right) N\mu \\ \sigma_{\Delta M}^2 &= \frac{4I(I+1)}{3} N\mu^2 \left[1 - \frac{4I(I+1)}{3} \left(\frac{\mu B}{k_B T} \right)^2 \right] \quad . \end{aligned} \quad (2.61)$$

Therefore, the equation for $\sigma_{\Delta M}^2$ derived here agrees with that obtained in the equation (2.56). Even at high magnetic fields and cryogenic temperatures, $\mu B \ll k_B T$ and the statistical magnetization fluctuations have the variance $\sigma_{\Delta M}^2 = \frac{4I(I+1)}{3} N\mu^2$. One can define the statistical nuclear spin polarization as

$$SNP = \frac{\sigma_{\Delta M}}{2IN\mu} = \sqrt{\frac{I+1}{3I}} \left(\frac{1}{\sqrt{N}} \right) \quad (2.62)$$

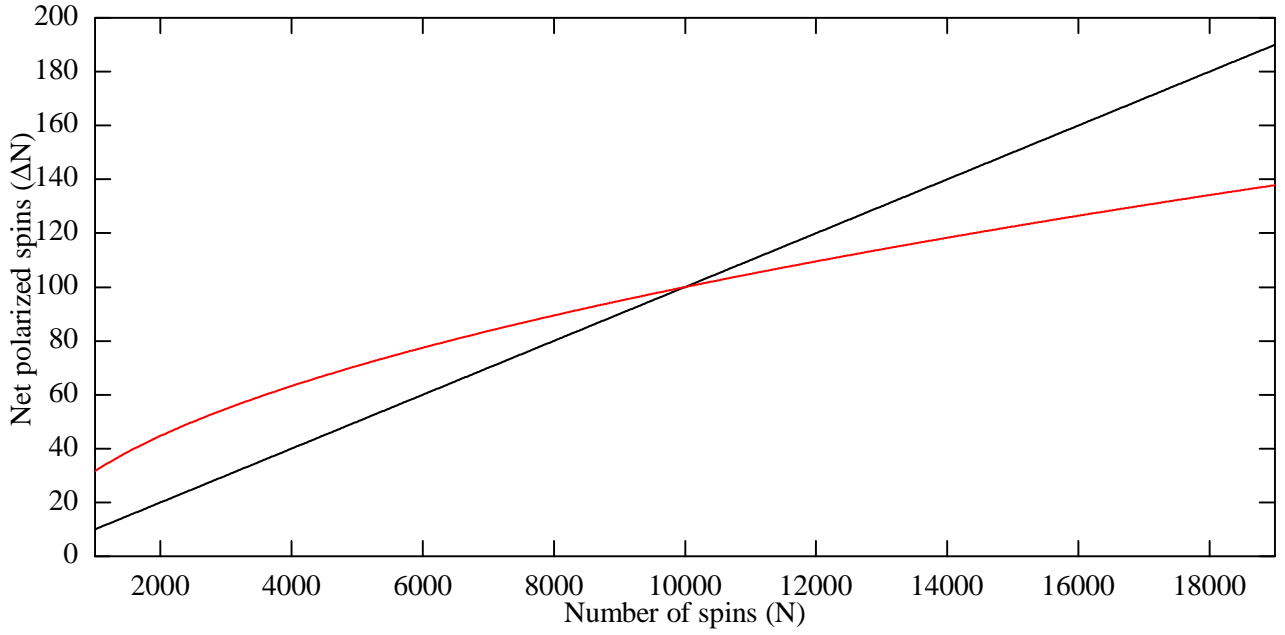


Figure 2.8: Boltzmann (black) and statistically polarized spins (red) in an ensemble of N proton spins at a temperature $T = 0.4$ K and a magnetic field $B = 4$ T.

and the Boltzmann nuclear spin polarization as

$$BNP = \frac{\overline{\Delta M}}{2IN\mu} = \frac{2(I+1)}{3} \left(\frac{\mu B}{k_B T} \right) \quad (2.63)$$

The term in the denominator $2IN\mu$ corresponds to 100% polarization of the nuclear spins. The dominance of statistical nuclear spin polarization, as defined by $SNP > BNP$, occurs for sample volumes $V < \frac{3}{4I(I+1)} \left(\frac{\mu B}{k_B T} \right)^{-2} \rho_N^{-1}$ where $\rho_N = \frac{N}{V}$ is the spin number density (Fig. 2.7 and Fig. 2.8).

	Magnetization	Polarization	Net polarized spins
Boltzmann	$\frac{4I(I+1)}{3} \left(\frac{\mu B}{k_B T} \right) N\mu$	$\frac{2(I+1)}{3} \left(\frac{\mu B}{k_B T} \right)$	$\frac{2(I+1)}{3} \left(\frac{\mu B}{k_B T} \right) N$
Statistical	$\sqrt{\frac{4I(I+1)}{3}} \sqrt{N}\mu$	$\sqrt{\frac{I+1}{3I}} \left(\frac{1}{\sqrt{N}} \right)$	$\sqrt{\frac{I+1}{3I}} \sqrt{N}$

Table 2.1: Boltzmann vs Statistical.

2.6.3 Gaussian distribution

Consider a system of N independent spins, each bearing a magnetic moment μ which may be directed either parallel or antiparallel to an external magnetic field B [43, 44]. Let the average polarization of the nuclear spin system be $p = \frac{\mu B}{k_B T}$. The ensemble averaged density matrix of single spin with spin-1/2 is

$$\rho = \begin{bmatrix} \frac{1+p}{2} & 0 \\ 0 & \frac{1-p}{2} \end{bmatrix} \quad (2.64)$$

Let us calculate the probability distribution of the total magnetic moment ΔM of the polarized system. The average value of ΔM in these conditions is $pN\mu$, and we are interested in the probability distribution $P(\Delta M)$. The projection of each moment is likely to be $+\mu$ with the probability $\frac{1+p}{2}$ and $-\mu$ with the probability $\frac{1-p}{2}$. We are interested in the probability of arrangements which result in $N_{\uparrow} = \frac{N+n}{2}$ moments being positive and $N_{\downarrow} = \frac{N-n}{2}$ being negative. The probability of a net moment $\Delta M = n\mu$ is given by

$$P(\Delta M) = P(n\mu) = \frac{N!}{\left(\frac{N+n}{2}\right)! \left(\frac{N-n}{2}\right)!} \left(\frac{1+p}{2}\right)^{\frac{N+n}{2}} \left(\frac{1-p}{2}\right)^{\frac{N-n}{2}} . \quad (2.65)$$

An approximation to the binomial distribution for large N can be obtained by expanding about the value $\overline{\Delta M}$ where $P(\overline{\Delta M})$ is a maximum, i.e., where $\frac{dP(\Delta M)}{dn} = 0$. Since the logarithm function is monotonic, we can instead choose to expand the logarithm. Let $n = \bar{n} + \delta n$, then

$$\ln [P(\Delta M)] = \ln [P(\overline{\Delta M} = \bar{n}\mu)] + B_1\delta n + \frac{1}{2}B_2(\delta n)^2 + \frac{1}{3!}B_3(\delta n)^3 + \dots \quad (2.66)$$

where

$$B_k \equiv \left[\frac{d^k \ln [P(\Delta M)]}{dn^k} \right]_{n=\bar{n}} . \quad (2.67)$$

But we are expanding about the maximum, so, by definition,

$$B_1 \equiv \left[\frac{d \ln [P(\Delta M)]}{dn} \right]_{n=\bar{n}} = 0 . \quad (2.68)$$

This also means that B_2 is negative, so we can write $B_2 = -|B_2|$.

Now, taking the logarithm of 2.63 gives

$$\ln [P(\Delta M)] = \ln N! - \ln \left(\frac{N+n}{2}\right)! - \ln \left(\frac{N-n}{2}\right)! + \frac{N+n}{2} \ln \left(\frac{1+p}{2}\right) + \frac{N-n}{2} \ln \left[\frac{1-p}{2}\right] . \quad (2.69)$$

For large $\frac{N+n}{2}$ and $\frac{N-n}{2}$, we can use Stirling's approximation

$$\ln \left(\frac{N+n}{2}\right)! \approx \frac{N+n}{2} \ln \left(\frac{N+n}{2}\right) - \frac{N+n}{2} , \quad (2.70)$$

so

$$\frac{d \ln \left(\frac{N+n}{2}\right)!}{dn} \approx \frac{1}{2} \left[\ln \left(\frac{N+n}{2}\right) + 1 \right] - \frac{1}{2} = \frac{1}{2} \ln \left(\frac{N+n}{2}\right) , \quad (2.71)$$

$$\frac{d \ln \left(\frac{N-n}{2}\right)!}{dn} \approx -\frac{1}{2} \ln \left(\frac{N-n}{2}\right) , \quad (2.72)$$

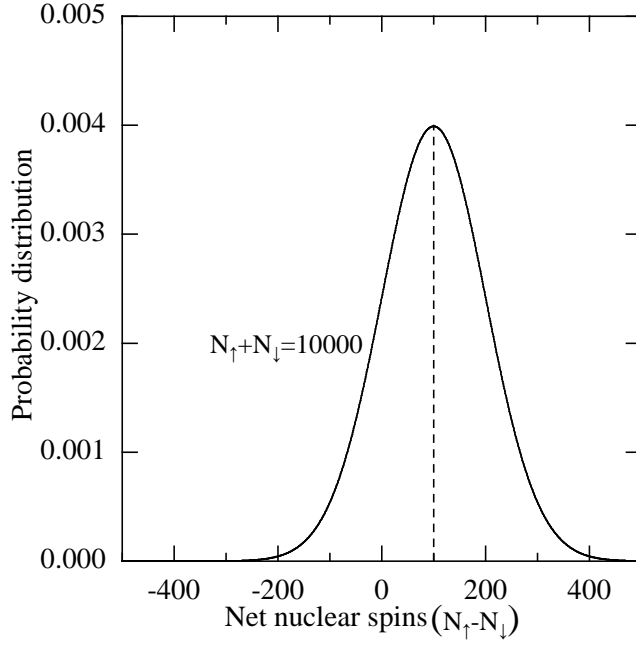


Figure 2.9: The probability distribution of a nuclear spin ensemble containing $N = 10000$ protons at a temperature $T = 0.4$ K and a magnetic field $B = 4$ T ($p \approx 0.01$).

and

$$\frac{d \ln P(\Delta M)}{dn} \approx -\frac{1}{2} \ln \left(\frac{N+n}{2} \right) + \frac{1}{2} \ln \left(\frac{N-n}{2} \right) + \frac{1}{2} \ln \left(\frac{1+p}{2} \right) - \frac{1}{2} \ln \left(\frac{1-p}{2} \right) \quad . \quad (2.73)$$

Setting this expression to 0, we get $\bar{n} = pN$.

We can now find the terms in the expansion,

$$\begin{aligned} B_2 &\equiv \left[\frac{d^2 \ln P(\Delta M)}{dn^2} \right]_{n=\bar{n}} \\ &= -\frac{1}{2} \left(\frac{1}{N+\bar{n}} + \frac{1}{N-\bar{n}} \right) \\ &= -\frac{1}{(1-p^2)N} \quad . \end{aligned} \quad (2.74)$$

Now, treating the distribution as continuous,

$$\lim_{N \rightarrow +\infty} \sum_{n=-N}^N P(\Delta M) \approx \int P(\Delta M) dn = \int_{-\infty}^{\infty} P(\overline{\Delta M} + \delta M) d\delta n = 1 \quad . \quad (2.75)$$

Ignoring terms higher than B_2 , we get

$$P(\Delta M) = P(\overline{\Delta M}) e^{-\frac{|B_2|(\delta n)^2}{2}} \quad . \quad (2.76)$$

The probability must be normalized, so

$$\int_{-\infty}^{\infty} P(\overline{\Delta M}) e^{-\frac{|B_2|(\delta n)^2}{2}} d\delta n = P(\overline{\Delta M}) \sqrt{\frac{2\pi}{|B_2|}} = 1 \quad (2.77)$$

and

$$\begin{aligned} P(\Delta M) &= \sqrt{\frac{|B_2|}{2\pi}} e^{-\frac{|B_2|(\delta n)^2}{2}} \\ &= \frac{1}{\sqrt{2\pi(1-p^2)N}} e^{-\frac{(n-pN)^2}{2(1-p^2)N}} . \end{aligned} \quad (2.78)$$

The binomial distribution is therefore approximated by a Gaussian distribution for any fixed p (even if p is small) as N is taken to infinity (Fig. 2.9). The mean and the variance of the polarization for this probability distribution is identical to that derived using the two methods described earlier.

Chapter 3

Nanomechanical Resonators

This Chapter deals with the determination of the power spectra of the mechanical resonators which are driven by random thermal forces and amplitude modulated periodic forces generated by nuclear spin inversions.

3.1 Brownian motion

The harmonic Brownian motion of an eigenmode of the mechanical resonator is well-described by the stochastic Langevin equation [33, 45]

$$\ddot{\mathbf{x}} = -\frac{\Omega_0}{Q}\dot{\mathbf{x}} - \Omega_0^2\mathbf{x} + \frac{\mathbf{F}(t)}{m} \quad (3.1)$$

where \mathbf{x} is the displacement of the resonator, Ω_0 is the natural frequency and Q is the quality factor. The force acting on the resonator is divided into three parts. The first part is the frictional force and is proportional to the velocity of the resonator. The second part of the force is the harmonic force proportional to the displacement. The third part is the random force acting independent of the motion of the resonator.

We Fourier-expand the random force and the displacement as stationary stochastic processes,

$$\mathbf{F}(t) = \sum_{n=-\infty}^{\infty} \mathbf{F}_n e^{i\Omega_n t}, \mathbf{x}(t) = \sum_{n=-\infty}^{\infty} \mathbf{x}_n e^{i\Omega_n t} \quad . \quad (3.2)$$

Then the stochastic differential equation is converted into the relation

$$\mathbf{x}_n = \frac{1}{\Omega_0^2 - \Omega_n^2 + i\frac{\Omega_n\Omega_0}{Q}} \frac{\mathbf{F}_n}{m} \quad (3.3)$$

between the Fourier components. If we write the power spectra of $\mathbf{F}(t)$ and $\mathbf{x}(t)$ as S_F and S_x respectively, we

obtain

$$\begin{aligned}
S_x(\Omega) &= \frac{1}{\left| \Omega_0^2 - \Omega^2 + i \frac{\Omega \Omega_0}{Q} \right|^2} \frac{S_F(\Omega)}{m^2} \\
&= \frac{1}{(\Omega_0^2 - \Omega^2)^2 + \left(\frac{\Omega \Omega_0}{Q} \right)^2} \frac{S_F(\Omega)}{m^2} .
\end{aligned} \tag{3.4}$$

Making the assumption of a white spectrum for the random force $\mathbf{F}(t)$, we have

$$S_F(\Omega) = S_F = \text{const} . \tag{3.5}$$

From the Wiener-Khintchine theorem, it follows that the correlation function of $\mathbf{F}(t)$ has a vanishingly short correlation time,

$$\langle F(t)F(t + \tau) \rangle = 2\pi S_F \delta(\tau) . \tag{3.6}$$

It follows from the Wiener-Khintchine theorem that for $\tau > 0$,

$$\begin{aligned}
\langle x(t)x(t + \tau) \rangle &= \int_{-\infty}^{\infty} d\Omega e^{i\Omega\tau} \frac{1}{(\Omega_0^2 - \Omega^2)^2 + \left(\frac{\Omega \Omega_0}{Q} \right)^2} \frac{S_F}{m^2} \\
&= \frac{S_F}{m^2} \int_{-\infty}^{\infty} d\Omega e^{i\Omega\tau} \frac{1}{(\Omega - \Omega_1 + i\frac{\gamma}{2})(\Omega + \Omega_1 + i\frac{\gamma}{2})} \frac{1}{2\Omega_1} \left(\frac{1}{\Omega - \Omega_1 - i\frac{\gamma}{2}} - \frac{1}{\Omega + \Omega_1 - i\frac{\gamma}{2}} \right) \\
&= \frac{S_F}{2m^2\Omega_1} 2\pi i \left(\frac{e^{i(\Omega_1 + i\frac{\gamma}{2})\tau}}{(i\gamma)(2\Omega_1 + i\gamma)} - \frac{e^{i(-\Omega_1 + i\frac{\gamma}{2})\tau}}{(-2\Omega_1 + i\gamma)(i\gamma)} \right) \\
&= \frac{\pi S_F}{m^2\Omega_1\gamma} e^{-\frac{\gamma}{2}\tau} \left(\frac{e^{i\Omega_1\tau}}{2\Omega_1 + i\gamma} - \frac{e^{-i\Omega_1\tau}}{-2\Omega_1 + i\gamma} \right) \\
&= \frac{\pi S_F}{m^2\Omega_1\gamma} \frac{1}{4\Omega_1^2 + \gamma^2} e^{-\frac{\gamma}{2}\tau} (2\Omega_1(e^{i\Omega_1\tau} + e^{-i\Omega_1\tau}) - i\gamma(e^{i\Omega_1\tau} - e^{-i\Omega_1\tau})) \\
&= \frac{\pi S_F}{m^2\Omega_0^2\gamma} e^{-\frac{\gamma}{2}\tau} \left(\cos \Omega_1\tau + \frac{\gamma}{2\Omega_1} \sin \Omega_1\tau \right) .
\end{aligned} \tag{3.7}$$

For a derivation of this result, the residues at the poles $\Omega = \pm\Omega_1 + i\frac{\gamma}{2}$, where $\gamma = \frac{\Omega}{Q}$ and $\Omega_1 = \left(\Omega_0^2 - \frac{\gamma^2}{4} \right)^{\frac{1}{2}}$ of the integrand are calculated. Thus, the correlation function of the displacement of the resonator is an exponentially decaying sinusoidal function in time with the decay constant $\frac{\gamma}{2}$. In particular, in the limit $\tau \rightarrow 0$, this reduces to

$$\langle x^2 \rangle = \frac{\pi S_F}{m^2\Omega_0^2\gamma} . \tag{3.8}$$

If the resonator mode is in thermal equilibrium with the bath at temperature T , the equipartition law

$$k \langle x^2 \rangle = k_B T \tag{3.9}$$

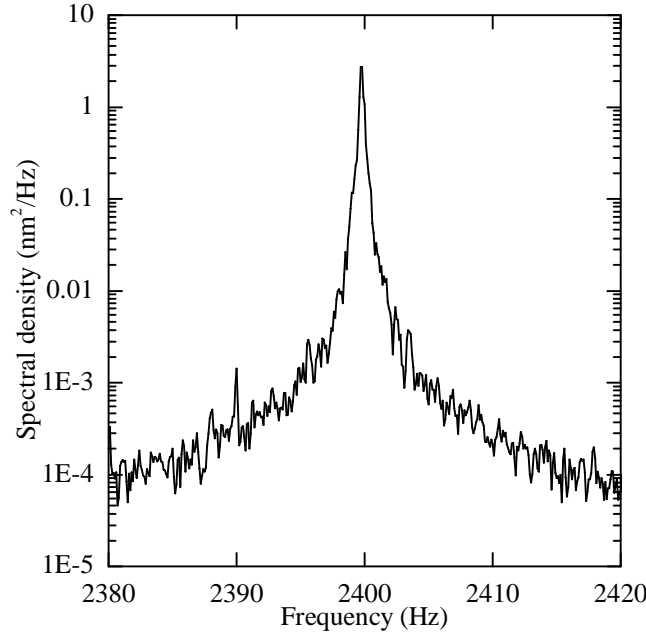


Figure 3.1: The power spectrum ($2\pi S_x(\Omega)$) of the thermal ($T = 4.5$ K) displacement of the cantilever has a Lorentzian lineshape. Spin force exerted at the cantilever frequency can give rise to the resonant response.

must hold for the energy distribution. For (3.8) to be consistent with this,

$$S_F = \frac{\Gamma k_B T}{\pi} \quad (3.10)$$

must hold where $\Gamma = m\gamma$. In other words, the random force F (if it has a white spectrum) must have the power spectral density given by (3.10) so that the Langevin equation (3.1) represents free Brownian motion in thermal equilibrium at temperature T . This stochastic force acting on the resonator determines its force sensitivity. Therefore, the equation (3.4) reduces to

$$S_x(\Omega) = \frac{1}{(\Omega_0^2 - \Omega^2)^2 + \left(\frac{\Omega\Omega_0}{Q}\right)^2} \frac{\Gamma k_B T}{\pi m^2} \quad (3.11)$$

In the single-sided spectrum convention, the above expressions for S_F and $S_x(\Omega)$ get doubled and hereafter, we shall work in this convention. For the frequencies Ω close to Ω_0 ,

$$\begin{aligned} S_x(\Omega) &\approx \frac{\pi Q}{2\Omega_0^3} \left(\frac{1}{\pi} \frac{\frac{\Omega_0}{2Q}}{(\Omega_0 - \Omega)^2 + \left(\frac{\Omega_0}{2Q}\right)^2} \right) \frac{S_F}{m^2} \\ &= \frac{\pi Q}{2\Omega_0^3} \frac{2\Gamma k_B T}{\pi m^2} \left(\frac{1}{\pi} \frac{\frac{\Omega_0}{2Q}}{(\Omega_0 - \Omega)^2 + \left(\frac{\Omega_0}{2Q}\right)^2} \right) \\ &= \frac{k_B T}{k} \left(\frac{1}{\pi} \frac{\frac{\Omega_0}{2Q}}{(\Omega_0 - \Omega)^2 + \left(\frac{\Omega_0}{2Q}\right)^2} \right) \\ &= \frac{1}{2\pi} \frac{k_B T}{m\Omega_0 Q} \frac{1}{(\Omega_0 - \Omega)^2 + \left(\frac{\Omega_0}{2Q}\right)^2} \end{aligned} \quad (3.12)$$

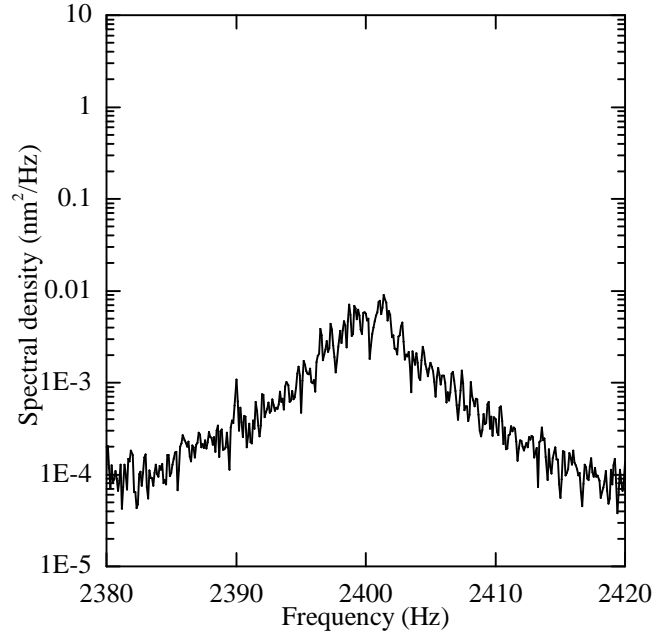


Figure 3.2: The power spectrum of the damped motion of the cantilever. An FPGA controller is used to damp the cantilever response thereby increasing the bandwidth of detection.

which gives a Lorentzian shape to the power spectrum of the displacement of the resonator (Fig. 3.1). The function in the bracket has an integral equal to unity. The mechanical Q of the cantilever can be damped down to increase its detection bandwidth without sacrificing force sensitivity [46] (Fig. 3.2).

3.2 Driven motion

From equation (3.1), one can derive the displacement of the cantilever due to the time-dependent force $F_i(t) = \mu_{z,i}(t)G_i \cos(\Omega_S t + \theta_i)$ exerted by a single spin as

$$x_i(t) = \frac{\mu_{z,i}(t)G_i}{m} \frac{\Omega_0^2 - \Omega_S^2}{(\Omega_0^2 - \Omega_S^2)^2 + (\frac{\Omega_0 \Omega_S}{Q})^2} \cos(\Omega_S t + \theta_i) + \frac{\mu_{z,i}(t)G_i}{m} \frac{\frac{\Omega_0 \Omega_S}{Q}}{(\Omega_0^2 - \Omega_S^2)^2 + (\frac{\Omega_0 \Omega_S}{Q})^2} \sin(\Omega_S t + \theta_i) \quad . \quad (3.13)$$

Defining $\Delta\Omega_S = \Omega_0 - \Omega_S$ and $\Delta\Omega_0 = \frac{\Omega_0}{Q}$, and keeping only the first order terms in $\frac{\Delta\Omega_S}{\Delta\Omega_0}$, we obtain

$$x_i(t) \approx \frac{2\Delta\Omega_S}{\Delta\Omega_0} \frac{\mu_{z,i}(t)G_i Q}{k} \cos(\Omega_S t + \theta_i) + \frac{\mu_{z,i}(t)G_i Q}{k} \sin(\Omega_S t + \theta_i) \quad . \quad (3.14)$$

The displacement due to the force exerted by N spins is

$$X(t) = \sum_{i=1}^N x_i(t) = \sum_{i=1}^N \frac{2\Delta\Omega_S}{\Delta\Omega_0} \frac{\mu_{z,i}(t)G_i Q}{k} \cos(\Omega_S t + \theta_i) + \sum_{i=1}^N \frac{\mu_{z,i}(t)G_i Q}{k} \sin(\Omega_S t + \theta_i) \quad . \quad (3.15)$$

The phase θ_i for each spin depends on its resonance frequency and the type of adiabatic inversion pulse being used. The region where the lateral gradient is largest contributes predominantly to the displacement signal.

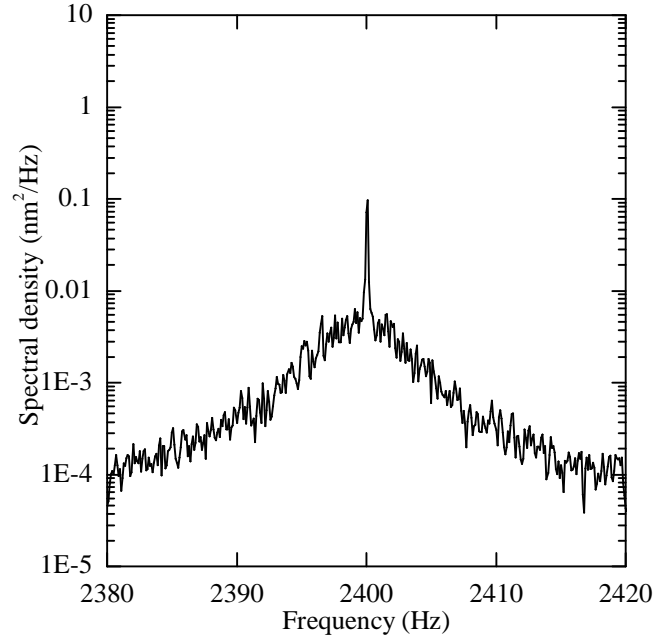


Figure 3.3: The power spectrum of the motion of the cantilever driven by forces generated by the adiabatic inversions. The narrowband spin noise spectral peak, whose spectral width is inversely proportional to the spin correlation time τ_m , rests atop a much broader peak generated by the damped cantilever vibrations [47].

Making the simplifying assumptions that all the spins in this region are flipped periodically at the cantilever frequency ($\Omega_S = \Omega_0$) at the same phase θ and experience the same gradient, the expression for the displacement reduces to a superposition of N independently fluctuating Kubo-Anderson signals (KAS) (Fig. 3.3).

$$X(t) = \sum_{i=1}^N \frac{\mu_{z,i}(t)GQ}{k} \sin(\Omega_S t + \theta) \quad . \quad (3.16)$$

The displacement of the cantilever is 90 degrees out of phase with respect to the driving force.

Chapter 4

Experimental Apparatus

The main goals of my doctoral research are to contribute to setting up of state-of-the-art low temperature, high vacuum magnetic resonance force microscopy (MRFM) setup and most importantly to use this setup to the detection of magnetic resonance in nanoscale samples. I am the first member of Poggio lab to work on the MRFM project and began working in an empty lab. Most of the experimental work discussed in this thesis is performed in a ^4He cryostat. The construction of a MRFM probe head for the ^4He system and the assembly of measurement electronics required ~ 1.5 years of build-up time. Apart from my contribution to the design and building, the successful running of the MRFM experimental setup is possible only because of the major contributions from Fei Xue and Martino Poggio. This Chapter gives a brief overview of the important components of the MRFM experimental setup. RF waveform generation and FPGA control system which have been mainly realised by myself is discussed in detail.

4.1 Operation

The MRFM setup is based on the cyclic adiabatic inversion (CAI) technique (Fig. 4.1, Fig. 4.2 and Fig. 4.4). It consists of a sample attached to the cantilever, a static magnetic field B_0 in the z -direction, and a micron width current carrying microwire patterned onto the substrate generating an amplitude and phase modulated RF field $\mathbf{B}_1(t)$. The sample consists of nuclear spins interacting with the magnetic gradient source, the static and RF fields. The idea of the CAI-based MRFM is that by setting the frequency of the phase modulation of the RF field equal to the natural frequency $\left(\frac{\Omega_0}{2\pi} = \frac{1}{T_c}\right)$ of the cantilever, we can cause adiabatic inversions of the spins in the resonant slice. These spin inversions in a field gradient exert an oscillating force on the cantilever, thereby increasing the vibration amplitude of the cantilever. The magnetic tip is then scanned with respect to the sample, and an image of the sample's structure can be taken.

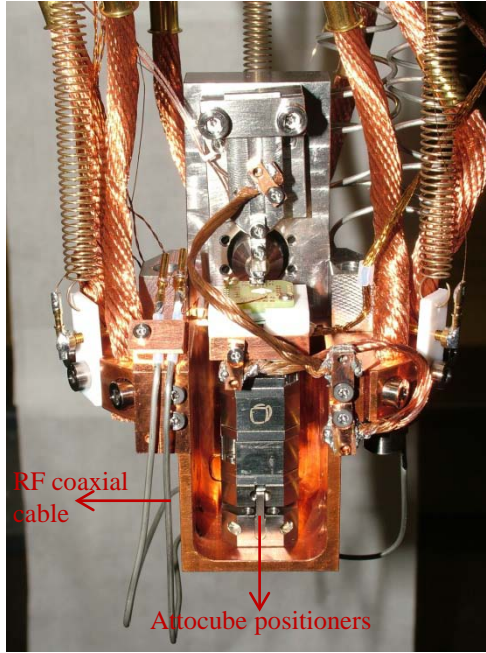


Figure 4.1: Photograph of the probe.

The MRFM probe is housed in a vacuum chamber that achieves a vacuum of 10^{-6} mbar or better at 4 K. The chamber is built into a ^4He cryostat and a large-bore superconducting magnet capable of producing static magnetic fields up to 6 T. The force-detecting element is a custom-made cantilever with a resonant frequency less than 5 kHz, with an attached sample. Attocube piezo positioners position the sample. The microwire is driven via a vacuum feedthrough from RF (DC to 300 MHz) generators, which are amplitude and frequency-modulated. A piezo actuator provides feedback to the cantilever from the FPGA controller. The cantilever vibration is detected using a sensitive fiber-optic interferometer.

4.2 Cantilevers

For our experiments, custom-made silicon cantilevers with a nominal spring constant $k = 100 \mu\text{N/m}$ and a frequency $f_c = 2.5$ kHz are employed. The cantilever has a length of $\sim 100 \mu\text{m}$ and a paddle to accommodate the laser spot. The sample is attached to the tip of the cantilever. Quality factors varied between 10000 and 50000 in vacuum (pressure $< 10^{-5}$ mbar). The tip of the cantilever is e-beam evaporated either with Si/Au (10/30 nm) or Ti/Au (10/30 nm) to reduce the strong surface interactions with the substrate.

4.3 Fiber-optic interferometer

The light beam is produced by a laser module ($\lambda=1550$ nm) and transmitted by a single-mode optical fiber into the vacuum chamber. A collimating lens focuses the beam onto the paddle of the cantilever. The reflected light is collected by a photodiode. Cantilever alignment is done mechanically when the vacuum chamber is open.

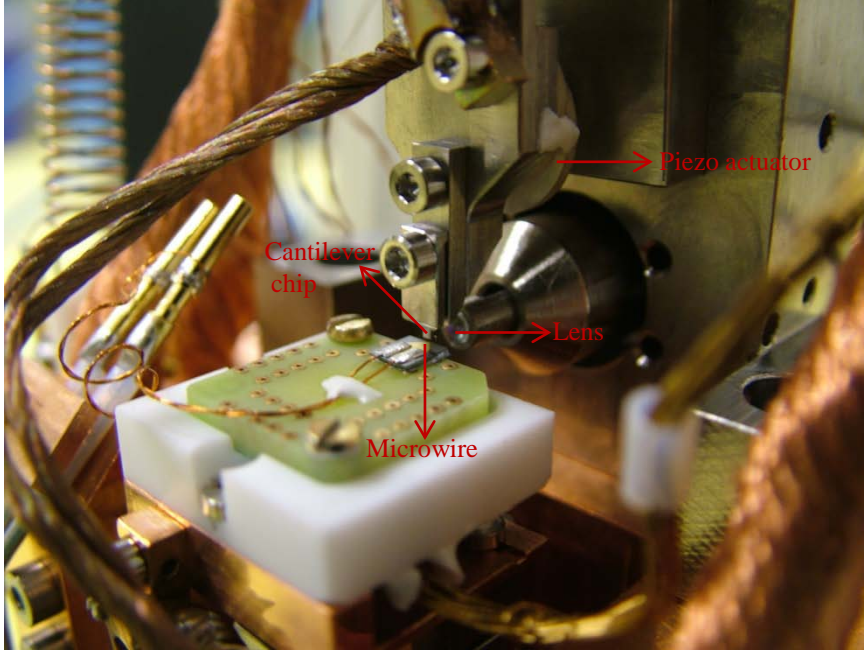


Figure 4.2: Zoom-in photograph of the probe.

The single-mode fiber-optic interferometer is well-suited to detect the displacement of cantilevers in scanning force microscopy experiments [48, 49] (Fig. 4.3). In a typical application, the laser couples coherent light into one arm of a 2×2 directional coupler with a 99/1 coupling ratio thereby serving as an interferometric beam splitter. Only 1% of the laser power reaches the cleaved end of the fiber. The cleaved end is positioned nearby a force sensing cantilever. Light reflects from both the cantilever and the cleaved end, then reenters the sensing fiber, where it interferes to form a displacement-dependent signal. The interferometer operates in the bad-cavity limit with the cavity “mirrors” being the cantilever and the cleaved end. Assuming that the power reflectance at the fiber-air interface R_1 and at the cantilever interface R_2 to be small ($R_1, R_2 \ll 1$), one can derive an expression for the detected power P_R in terms of the incident optical power $P_I = E_I^2$

$$\begin{aligned}
P_R &= |(E_I \sqrt{R_1} e^{i\phi_1} + E_I \sqrt{1-R_1} \sqrt{R_2} \sqrt{1-R_1} e^{i\phi_2})|^2 \\
&= (E_I \sqrt{R_1} e^{i\phi_1} + E_I \sqrt{1-R_1} \sqrt{R_2} \sqrt{1-R_1} e^{i\phi_2})(E_I \sqrt{R_1} e^{-i\phi_1} + E_I \sqrt{1-R_1} \sqrt{R_2} \sqrt{1-R_1} e^{-i\phi_2}) \\
&= E_I^2 R_1 + E_I^2 R_2 (1-R_1)^2 + E_I^2 \sqrt{R_1 R_2} (1-R_1) (e^{i(\phi_1-\phi_2)} + e^{i(\phi_2-\phi_1)}) \\
&= E_I^2 R_1 + E_I^2 R_2 (1-R_1)^2 + 2E_I^2 \sqrt{R_1 R_2} (1-R_1) \cos(\phi_1 - \phi_2) \\
&= E_I^2 R_1 + E_I^2 R_2 (1-R_1)^2 + 2E_I^2 \sqrt{R_1 R_2} (1-R_1) \cos\left(\frac{4\pi l}{\lambda} + \phi\right)
\end{aligned} \tag{4.1}$$

where l is the fiber-cantilever spacing, ϕ is the phase shift acquired by the light reflected from the cantilever and the laser wavelength is λ . For $R_1, R_2 \ll 1$,

$$\begin{aligned}
P_R &= E_I^2 \left[R_1 + R_2 + 2\sqrt{R_1 R_2} \cos\left(\frac{4\pi l}{\lambda} + \phi\right) \right] \\
P_{\max} &= E_I^2 (R_1 + R_2 + 2\sqrt{R_1 R_2})
\end{aligned}$$

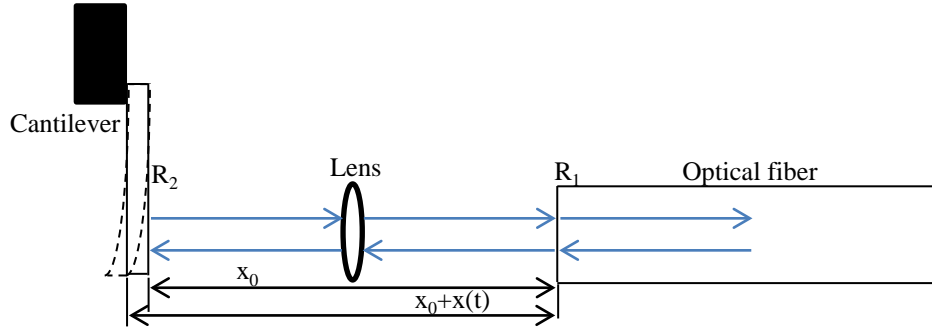


Figure 4.3: Fiber-optic interferometer diagram.

$$\begin{aligned}
 P_{\min} &= E_I^2 (R_1 + R_2 - 2\sqrt{R_1 R_2}) \\
 P_{\text{avg}} &= \frac{P_{\max} + P_{\min}}{2} = E_I^2 (R_1 + R_2) \\
 P_{\max} - P_{\min} &= 4E_I^2 \sqrt{R_1 R_2} \quad .
 \end{aligned} \tag{4.2}$$

Fringe visibility is defined as $F = \frac{P_{\max} - P_{\min}}{P_{\max} + P_{\min}}$, where P_{\max} and P_{\min} are the maximum and minimum output powers produced by constructive and destructive interference. The detected signal power varies with average output power P_{avg} as

$$\begin{aligned}
 P_R &= E_I^2 (R_1 + R_2) \left[1 + \frac{4\sqrt{R_1 R_2}}{2(R_1 + R_2)} \cos \left(\frac{4\pi l}{\lambda} + \phi \right) \right] \\
 &= P_{\text{avg}} \left[1 + F \cos \left(\frac{4\pi l}{\lambda} + \phi \right) \right] \quad .
 \end{aligned} \tag{4.3}$$

The cantilever displacement varies in time either due to its thermal motion or external forced oscillations. For small deviations $x(t)$ of the cantilever from its equilibrium position x_0 ,

$$\begin{aligned}
 P_R &= E_I^2 \left[R_1 + R_2 + 2\sqrt{R_1 R_2} \cos \left(\frac{4\pi(x_0 + x(t))}{\lambda} + \phi \right) \right] \\
 &= E_I^2 \left\{ R_1 + R_2 + 2\sqrt{R_1 R_2} \left[\cos \left(\frac{4\pi x_0}{\lambda} + \phi \right) \cos \left(\frac{4\pi x(t)}{\lambda} \right) - \sin \left(\frac{4\pi x_0}{\lambda} + \phi \right) \sin \left(\frac{4\pi x(t)}{\lambda} \right) \right] \right\} \\
 &\simeq E_I^2 \left\{ R_1 + R_2 + 2\sqrt{R_1 R_2} \left[\cos \left(\frac{4\pi x_0}{\lambda} + \phi \right) - \sin \left(\frac{4\pi x_0}{\lambda} + \phi \right) \frac{4\pi x(t)}{\lambda} \right] \right\} \quad .
 \end{aligned} \tag{4.4}$$

For maximum sensitivity, one should choose x_0 such that

$$\begin{aligned}
 \cos \left(\frac{4\pi x_0}{\lambda} + \phi \right) &= 0 \\
 \sin \left(\frac{4\pi x_0}{\lambda} + \phi \right) &= -1 \quad .
 \end{aligned} \tag{4.5}$$

Then, a linearized interferometer output

$$P_R = E_I^2 \left(R_1 + R_2 + 2\sqrt{R_1 R_2} \frac{4\pi x(t)}{\lambda} \right) = P_{\text{avg}} \left(1 + \frac{4\pi F x(t)}{\lambda} \right) \tag{4.6}$$

is obtained. Interference signals are transmitted by the directional coupler into photodiode amplifiers which

produce a voltage V proportional to signal power P . The linearized interferometer gain (or sensitivity) for small deviations is $\frac{\Delta V}{\Delta x} = \frac{2\pi(V_{\max}-V_{\min})}{\lambda}$.

The power transmittance T_2 of a cantilever of thickness t and refractive index $n = 3.5$ in air is

$$\sqrt{T_2} = \frac{4n \exp(-i\phi)}{(1+n)^2 - (1-n)^2 \exp(-i2\phi)} \quad (4.7)$$

where $\phi = nkt$ and k is the wavenumber. To collect as much cantilever-reflected light as possible back into the fiber, its reflection coefficient should be high. The absorption of light by the cantilever can be neglected. The expression for T_2 can be simplified as

$$\begin{aligned} \sqrt{T_2} &= \frac{4n}{(1+n)^2 \exp(i\phi) - (1-n)^2 \exp(-i\phi)} \\ &= \frac{4n}{((1+n)^2 - (1-n)^2) \cos(\phi) + i((1+n)^2 + (1-n)^2) \sin(\phi)} \\ &= \frac{2n}{2n \cos(\phi) + i(1+n^2) \sin(\phi)}. \end{aligned} \quad (4.8)$$

For minimum transmission, $\cos(nkt) = 0$, which implies $t = \frac{(2j+1)\lambda}{4n}$ ($j = 0, 1, 2, \dots$). Therefore, the minimum thickness is $t = \frac{1550}{4 \times 3.5} = 110$ nm and the maximum power reflectance is $R_2 = 1 - T_2 = \left(\frac{1-n^2}{1+n^2}\right)^2 = 72\%$. Since the cantilever is made of silicon ($n = 3.5$) and has a thickness of 100 nm, it has a reflectance R_2 of approximately 30%. Therefore, it would be best to have the reflectance at the cleaved fiber end also as 30% to couple maximum power into the fiber. Since the refractive index n of the fiber is 1.45, the power reflectance at normal incidence at the fiber-air interface is given by $R_1 = \left(\frac{n_1-n_2}{n_1+n_2}\right)^2 = \left(\frac{1.45-1}{1.45+1}\right)^2 = 3.37\%$. Therefore, the cleaved end of the fiber is evaporated with 25 nm of Si to increase its reflectance to $\sim 30\%$. 70% of the incident light power is reflected back at the cleaved end and the remaining 30% reaches the cantilever. The reflected light from the cantilever differs in phase (based on the cavity length between the cantilever and the fiber cleaved end) from the 70% reflected light. Both these light waves interfere and are observed on a signal photodiode.

The laser can change its emitting wavelength with time according to the variations in the room temperature. In other words, there can be a deviation in the lasing wavelength from the stated value of 1550 nm. The wavelength change of the laser is 0.2 nm/degree celsius. To lock the wavelength at a certain frequency, the laser operated in the constant power mode is controlled with the the help of a thermoelectric cooler (TEC) to counteract the changes in temperature. The interferometer has a broadband response, i.e., we can observe several fringes and accordingly do calibration for our experiments. The TEC controller can be used to change the laser temperature by several degrees.

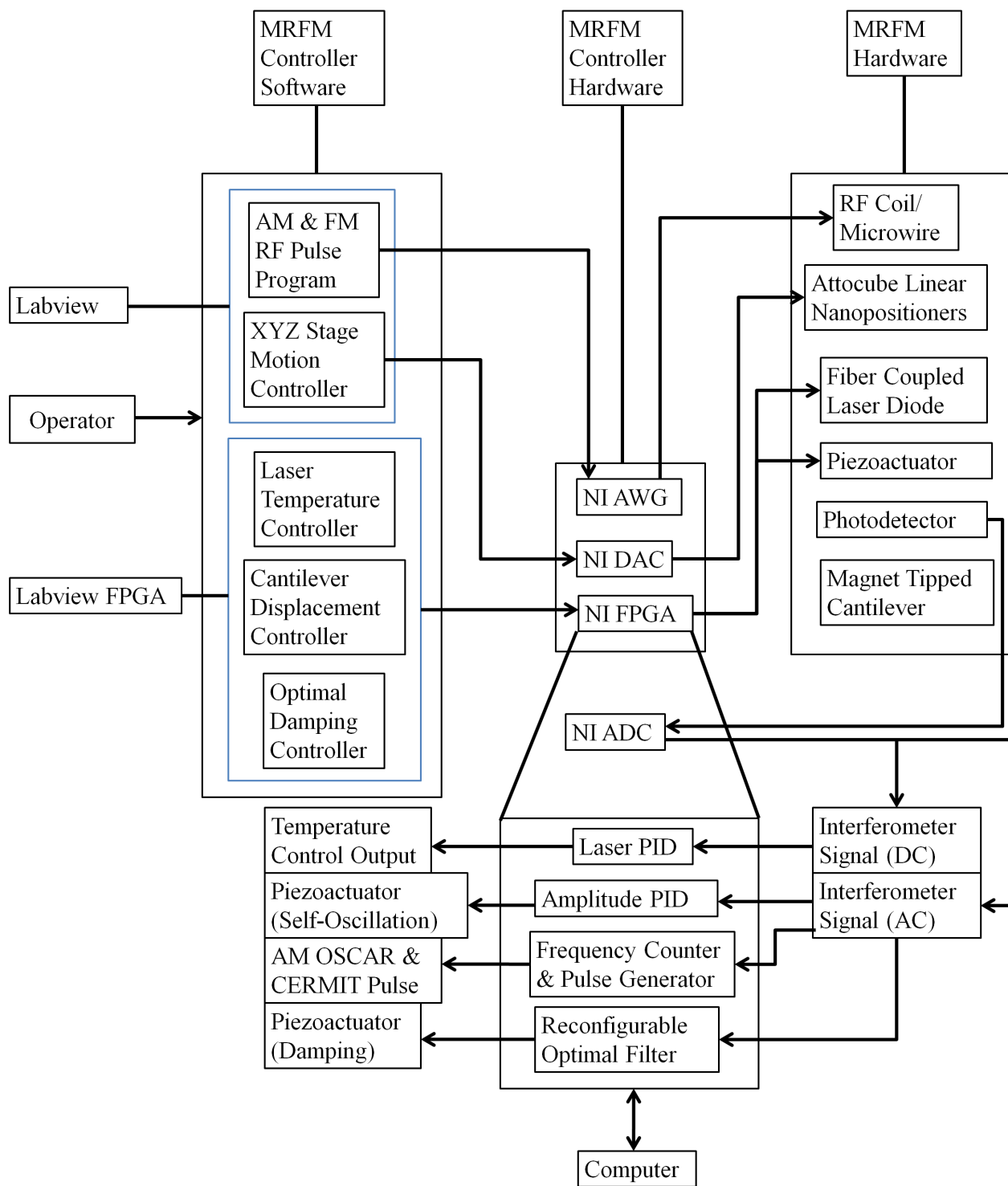


Figure 4.4: Flow-chart description of the magnetic resonance force microscope setup

4.4 Microwire RF source

Current delivered through the microwires, made of Ti/Au (10/190 nm), are used to generate AC magnetic fields for nuclear magnetic resonance (NMR) experiments at cryogenic, high vacuum conditions [47]. The optimum dimensions for the length, width and thickness of the microwire are calculated to generate RF magnetic fields

without too much heating. Ideally, the microwire should have broadband transmission and negligible attenuation over the frequency range between 0 MHz and 300 MHz. The substrate on which the microwire is patterned has to be scanned relative to the cantilever overhanging the chip for our scanning probe experiments. Both the pads of the microwire are connected through short and thin copper leads to the center conductors of rigid coaxial lines leading to the top of the cryostat. These leads are fixed and pressed onto the two pads using sticky indium metal. The non-rigid and flexible copper leads allow us to scan the microwire relative to the cantilever. While scanning, the inductances and capacitances of the copper leads keep changing which also alters the overall impedance of the microwire. However, this is not crucial for low frequencies while it is crucial at high frequencies to deliver power without having any reflections. Therefore, this circuit doesn't work optimally at high frequencies (>1 GHz) since the two leads to the microwire pads should always be impedance matched to 50 Ohms to avoid power losses. The circuit can be tested for its RF characteristics using a microwave circuit analyzer.

4.5 RF pulse generation

4.5.1 Arbitrary waveform generator

The digital arbitrary waveform generator (AWG) hardware from National Instruments (NI) (PXI-5421 & PXIe-5451) is employed for generating the required waveforms for nuclear magnetic resonance (NMR) experiments. PXI-5421 has about 40 MHz of analog bandwidth whereas PXIe-5451 offers up to 140 MHz of analog bandwidth. NMR experiments often require waveforms with carrier frequencies above 100 MHz. The signal from PXI-5421 can be mixed with a RF function generator in order to get waveforms with higher carrier frequencies, for e.g., 120 MHz. To avoid the mixing step altogether, PXIe-5451 can be used directly at 120 MHz. However, the achievable gains with a PXIe-5451 hardware (~ 2.5) are not as high as PXI-5421 hardware (~ 6). Moreover, PXIe-5451 is a PXI Express hardware and can be used only with a PXIe chassis.

4.5.2 Timing

The PXI-1042 chassis (used in our ^3He MRFM system) has an external reference input at the back which is referenced to a stable Rubidium clock source. The reference output at the back of PXI 1042 is connected as a clock input to a HP RF function generator which is used as a mixer to upconvert AWG signals from 0-40 MHz to higher carrier frequencies. This maintains synchronisation between the PXI chassis clock and the RF function generator clock. The PXI chassis supplies a 10 MHz reference clock signal independently to each peripheral slot. An independent buffer drives the clock signal to each peripheral slot. This common reference clock signal can be used to synchronize multiple devices such as PXI-5421 and PXI-7854R (FPGA hardware) in a measurement or control system.

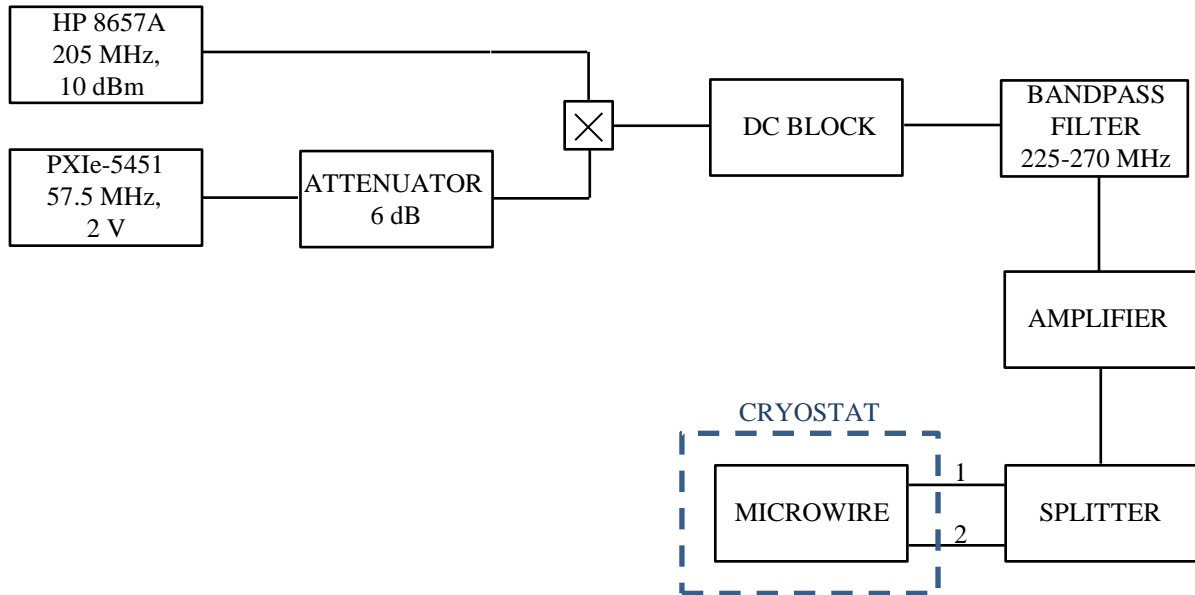


Figure 4.5: Diagram of the electrical circuit for generation of the RF waveform in MRFM experiments. Two signal generators (HP 8657A) and (NI PXIe-5451) are used to produce sine wave carriers and arbitrary waveform envelopes respectively. Carrier and envelope waveforms are combined on an analogue mixer (\times) to produce the desired adiabatic inversion pulse. The generated RF waveform is band-pass filtered and sent to a RF power amplifier. The resulting signal is passed through a splitter to create two independent signals ‘1’ and ‘2’ that have nominally the same amplitudes and opposite phases to differentially drive the RF microwire and to ensure a voltage null at the constriction to minimize excitation of the cantilever by time-varying electric fields.

The PXI-1033 chassis (used in our ^4He MRFM system) does not have such a reference clock input and output. In other words, PXI-1033 doesn’t provide the possibility of overriding the 10 MHz clock with BNC connectors as PXI-1042 does. In order to resolve the synchronization issue for PXI-1033 chassis, it is possible to reference the AWG hardware by phase-locking its sample clock timebase to an external signal that is present on the CLK IN front panel connector. The synchronization is made possible by routing the output clock of the RF function generator to CLK IN input.

4.5.3 Digital synthesis of amplitude and phase modulated RF pulses

The waveform for the RF excitation is produced by AWG, and after the power amplifier, coupled to the microwire via coaxial cables. Adiabatic inversion in MRFM experiments requires an amplitude and phase modulated periodic waveform, which can be produced by a digital device. We synthesize the waveform so that the total accumulated phase of the waveform over half the cantilever cycle is equal to an odd multiple of π . The RF waveform has to be limited in the spectral domain to an excitation width of typically 1 MHz.

NI AWGs feature large waveform memory (128 MB for PXIe-5451, 32 MB for PXI-5421) and thus allow direct high-precision synthesis of the RF waveform. In our experiments, we use a hardware implementation based on AWG combined with HP 8657A high frequency signal generator (100 kHz to 1040 MHz). The circuit schematics

are shown in Fig. 4.5. The total signal waveform is obtained by analogue mixing of a sine wave carrier from HP 8657A and an RF waveform envelope which is produced by NI AWG. Waveform envelope is computed by sampling the following function at discrete time points:

$$F(t) = A(t) \cos \left(\int_0^t \omega(t) dt + \phi_0 \right) \quad (4.9)$$

where $A(t)$ is amplitude modulation, $\omega(t)$ is frequency modulation and ϕ_0 is the initial phase of the waveform. $A(t)$ and $\omega(t)$ are chosen to obtain the desired amplitude ($\omega_1(t)$) and frequency modulation ($\Delta\omega(t)$) of adiabatic pulses.

We apply sawtooth and hyperbolic secant frequency sweeps for achieving adiabatic inversion [11, 30].

SAWTOOTH:

$$\begin{aligned} \omega(t) &= \omega_0 - \Delta\omega + 4\Delta\omega \frac{t}{T_c}, \quad 0 \leq t \leq \frac{T_c}{2} \\ \phi(t) &= \phi_0 + \int_0^t \left(\omega_0 - \Delta\omega + 4\Delta\omega \frac{t}{T_c} \right) dt \\ \phi(t) &= \phi_0 + (\omega_0 - \Delta\omega)t + 2\Delta\omega \frac{t^2}{T_c} \end{aligned} \quad (4.10)$$

Setting the boundary conditions for the phase, $\phi(0) = 0$ and $\phi(\frac{T_c}{2}) = (2N + 1)\pi$, we obtain $\phi_0 = 0$ and $N = \frac{\omega_0 T_c - 1}{2\pi}$. Therefore, for a waveform with constant-amplitude modulation and sawtooth frequency modulation,

$$F(t) = A \cos \left[\left(\frac{2\pi}{T_c} (2N + 1) - \Delta\omega \right) t + 2\Delta\omega \frac{t^2}{T_c} \right] \quad (4.11)$$

HYPERBOLIC SECANT (HS):

$$\begin{aligned} \omega(t) &= \omega_0 + \Delta\omega \frac{\tanh(\beta(\frac{4t}{T_c} - 1))}{\tanh \beta} \\ \phi(t) &= \phi_0 + \int_0^t \left(\omega_0 + \Delta\omega \frac{\tanh(\beta(\frac{4t}{T_c} - 1))}{\tanh \beta} \right) dt \\ \phi(t) &= \phi_0 + \omega_0 t + \frac{\Delta\omega T_c \coth \beta \log(\cosh(\beta(\frac{4t}{T_c} - 1)))}{4\beta} \end{aligned} \quad (4.12)$$

Setting the boundary conditions for the phase, we obtain $\phi_0 = -\frac{\Omega T_c \coth \beta \log(\cosh(\beta))}{4\beta}$ and $N = \frac{\omega_0 T_c - 1}{2\pi}$. Therefore, for a waveform with hyperbolic secant amplitude modulation and hyperbolic tangent frequency modulation,

$$F(t) = \frac{1}{\cosh(\beta(\frac{4t}{T_c} - 1))} \cos \left[\frac{2\pi}{T_c} (2N + 1)t + \frac{\Delta\omega T_c \coth \beta \log\left(\frac{\cosh(\beta(\frac{4t}{T_c} - 1))}{\cosh \beta}\right)}{4\beta} \right] \quad (4.13)$$

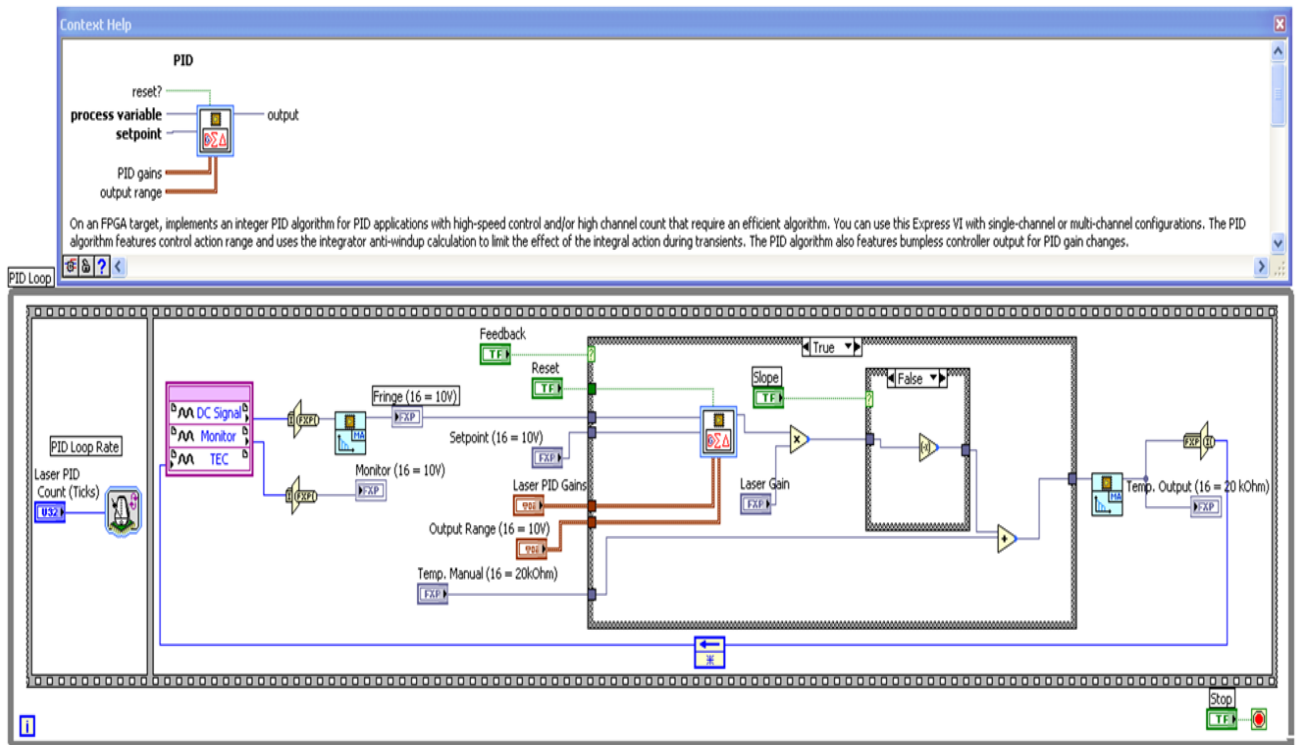


Figure 4.6: A PID controller to tune the temperature of the laser.

The power in carrier wave and waveform envelope are chosen to be similar, which allows nonlinear distortions of the RF amplifier to be minimized. The total signal waveform is band-pass filtered to remove the spectral components arising from upconversion process. However due to imperfections of the RF circuit, the amplitude of the RF field outside the excitation bandwidth is not strictly zero. The typical peak amplitude of the RF rotating magnetic field used in MRFM experiments is $B_1 = 10$ mT. In our experimental setup, continuous application of RF adiabatic pulses with such a peak amplitude results in sample heating of less than 0.5 K. The duration (~ 0.1 ms) of the RF pulse for π -inversion is long enough to adiabatically invert the populations of the nuclear spin states. On the other hand, the duration is much shorter than the correlation time ($\tau_m \sim 100$ ms) of nuclear spin polarization, and thus achieves a complete inversion of the polarization.

4.6 FPGA-based control system

For our experiments in MRFM, a FPGA-based control system is implemented as it offers performance and flexibility. The Labview FPGA project consists of a single FPGA VI consisting of all possible control and measurement loops. Each of these loops is controlled by a separate Host VI which runs on the computer. All the Host and FPGA VIs were programmed using Labview FPGA 2010, Labview 2010, Digital Filter Design Toolkit (DFD) and Control Design Toolkit. These toolkits are very convenient and efficient to use for programming and enable us to approach the task in an “electrical engineering” way. We have also used Modulation Toolkit to simplify the generation of radio frequency waveforms.

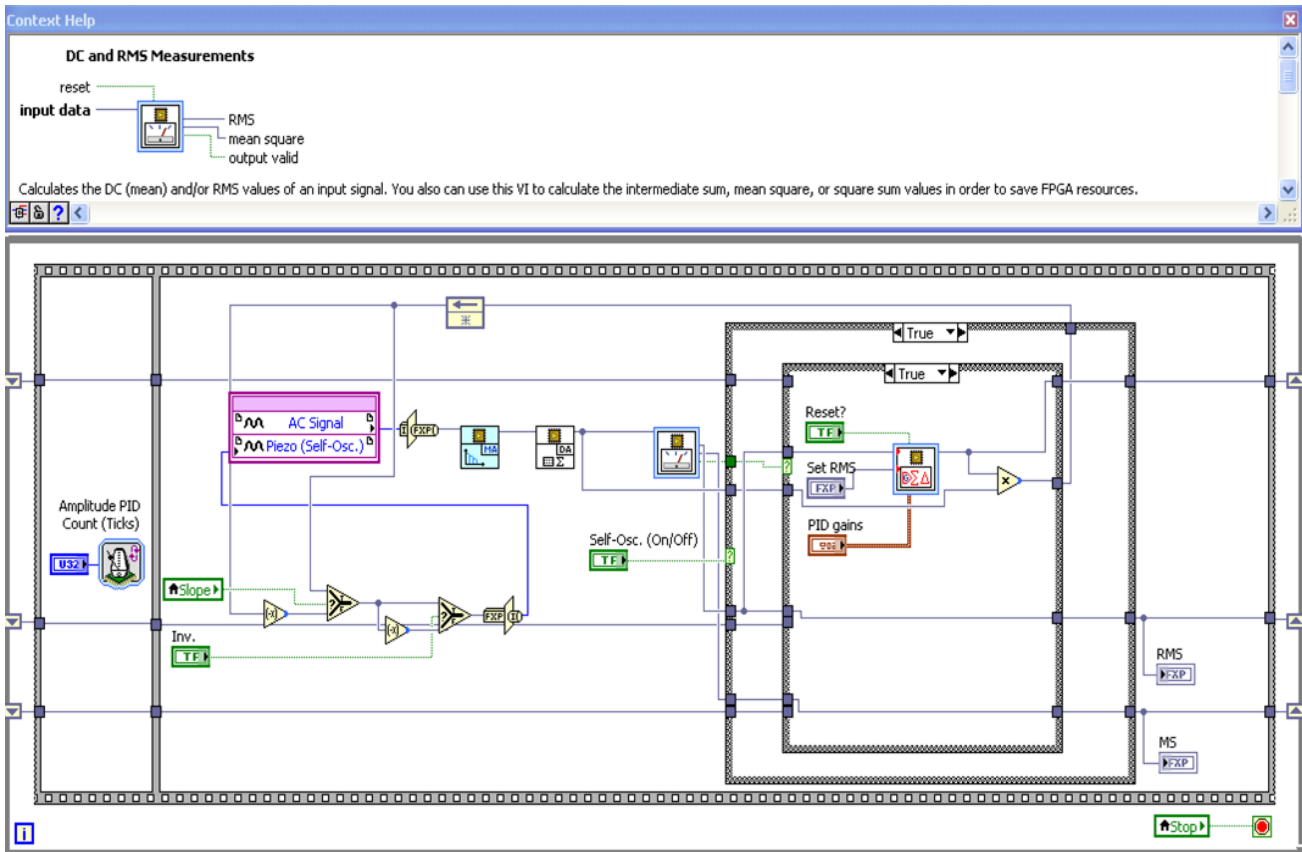


Figure 4.7: A PID controller to self-oscillate the cantilever to a set amplitude.

The FPGA VI is programmed considering the fact that the multipliers (DSP48Es) are the limiting resources among all the available logic elements in the FPGA hardware. There are 64 DSP48Es in PXI-7854R hardware. Each DSP48E consists of a single 25 bit by 18 bit multiplier. Accordingly, special attention has been paid so that the word lengths of the intermediary inputs and outputs does not exceed 25 bits as far as possible. This avoids the consumption of more than one DSP48E for a single multiplication task. Moreover, Butterworth filter available in FPGA palette consumes four DSP48Es for a single filtering operation. Therefore, we have developed and generated our own filter codes using DFD toolkit, the filter architecture being either moving average (for lowpass) and distributed arithmetic (for highpass). Effectively, each one of these filters consume either zero or one DSP48E.

FPGA VI consists of the following subVIs:

1. Laser PID controller (6 DSP48Es) used to tune the temperature of the laser by controlling the TEC,
2. Displacement PID controller (10 DSP48Es) used to self-oscillate the cantilever via positive feedback,
3. Optimal controller (6 DSP48Es) used to control the cantilever Q or response time via negative feedback,
4. Phase locked loop (15 DSP48Es) used to measure the frequency of a self-oscillated cantilever signal,
5. Lock-in filter bank (0 DSP48Es) used to filter the spin noise and thermal noise, and
6. Frequency counter, trigger and pulse generator (0 DSP48Es), used for iOSCAR/CERMIT experiments.

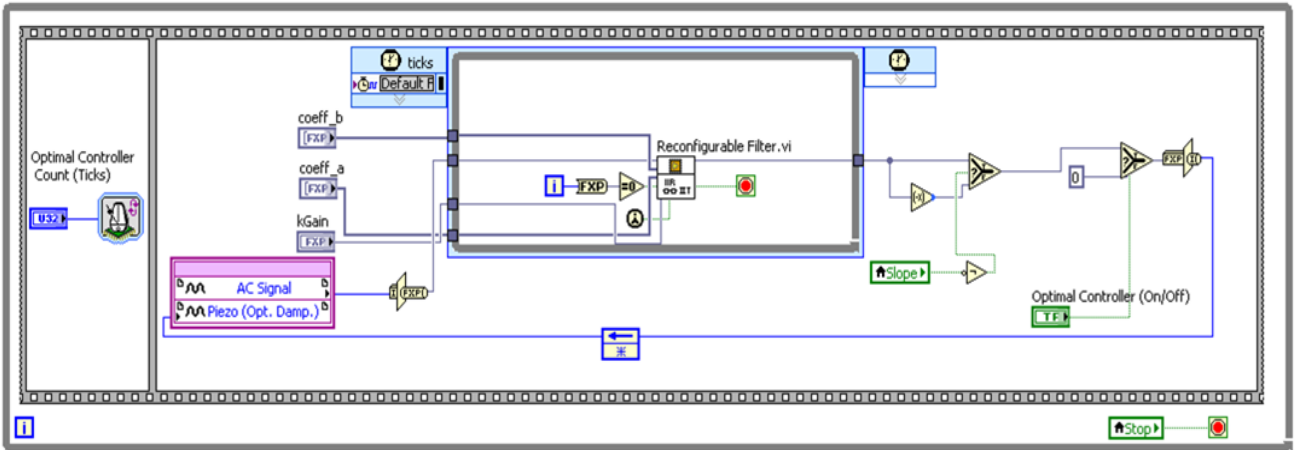


Figure 4.8: An optimal controller to damp the cantilever Q .

Using careful optimization procedures, FPGA VI consumed a total of 37 DSP48Es only. We have also made extensive use of FIFOs, single cycled timed loops (SCTLs) and block RAM to transfer data within the FPGA VI; and also to transfer data from the FPGA VI to the Host VI and vice versa. The device utilization is summarized below:

- Total Slices: 37.1% (6409 out of 17280),
- Slice Registers: 20.9% (14417 out of 69120),
- Slice LUTs: 21.8% (15085 out of 69120),
- DSP48s: 60.9% (39 out of 64), and
- Block RAMs: 51.6% (66 out of 128).

4.6.1 Laser PID controller

A constant laser temperature (wavelength) is maintained by a proportional-integral-derivative (PID) feedback loop controlling the thermoelectric cooler (TEC) while monitoring the slowly varying cantilever deflection (DC signal). The feedback loop is implemented with a FPGA hardware and a Thorlabs (TED200C) temperature controller (Fig. 4.6).

4.6.2 Displacement PID controller

The cantilever signal (AC) is measured with a FPGA hardware. The cantilever mounted on a piezoelectric actuator is driven in a PID loop which uses the desired cantilever root-mean-square (RMS) amplitude as its setpoint (Fig. 4.7).

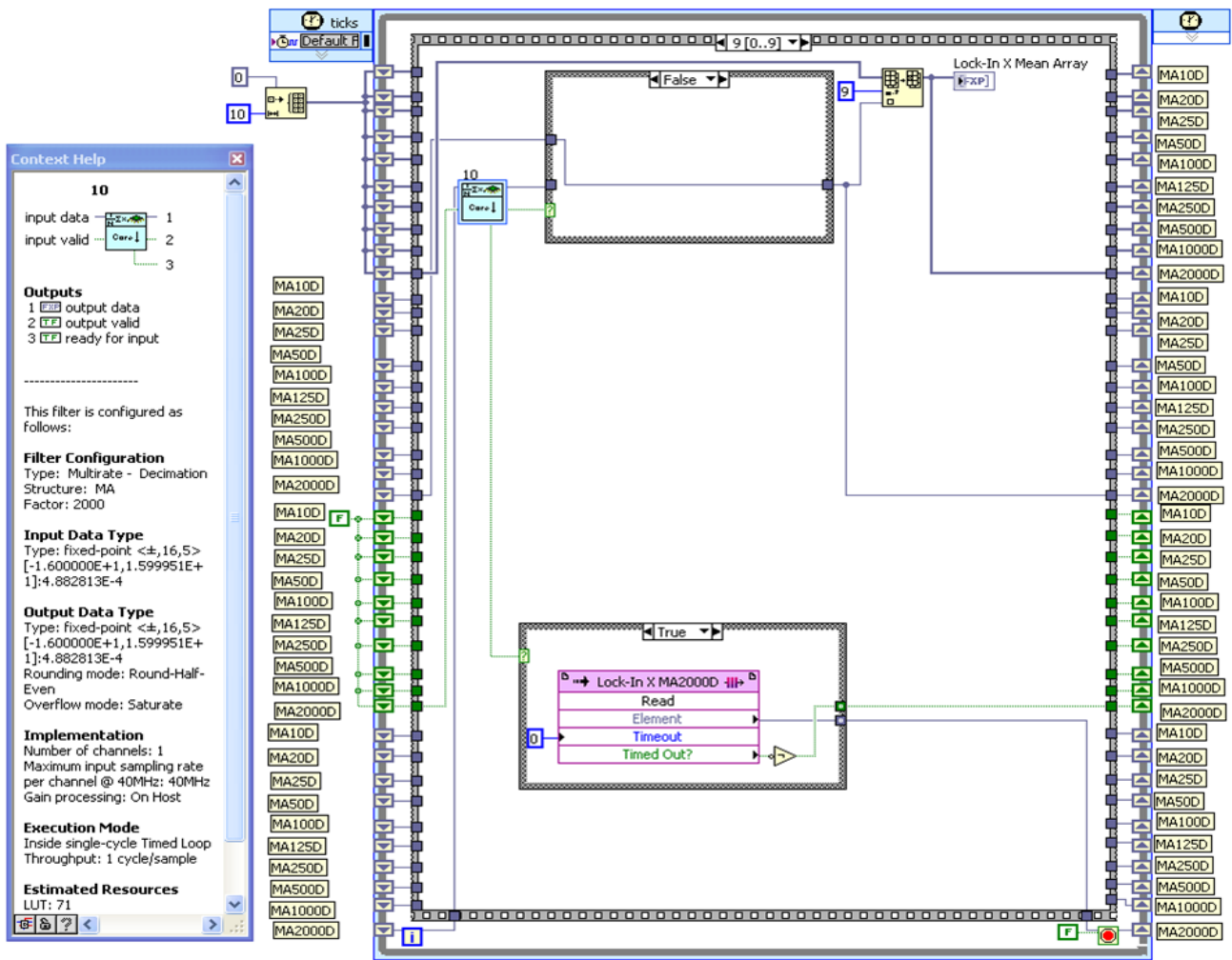


Figure 4.9: A bank of moving-average filters to filter the spin noise and thermal noise.

4.6.3 Optimal controller

The optimal controller is used for broadening the cantilever response bandwidth without sacrificing the signal-to-noise ratio [46]. The optimal control theory calculates the transfer function of the controller for the set of cantilever parameters (Ω_0 , k , Q , thermal force noise, measurement noise). The performance of the optimal controller is superior to the standard negative feedback controller because the optimal control theory considers the process and measurement noise when calculating the controller parameters, while the negative feedback controller is independent of these noise terms. Therefore, its performance is better at large damping, when the resonance curve gets pushed down to the level of the interferometer measurement noise. One can achieve variable damping with the optimal controller by controlling the target Q (Fig. 4.8).

4.6.4 Phase locked loop (PLL)

The basic PLL code is downloaded from Labview FPGA RF Communication Library available as an IP in NI website. PLL block has to be inside a SCTL and a sampling frequency of 50 kHz works well for sampling the input. PLL outputs 50k frequency points every second and the data is sent to the host every second using

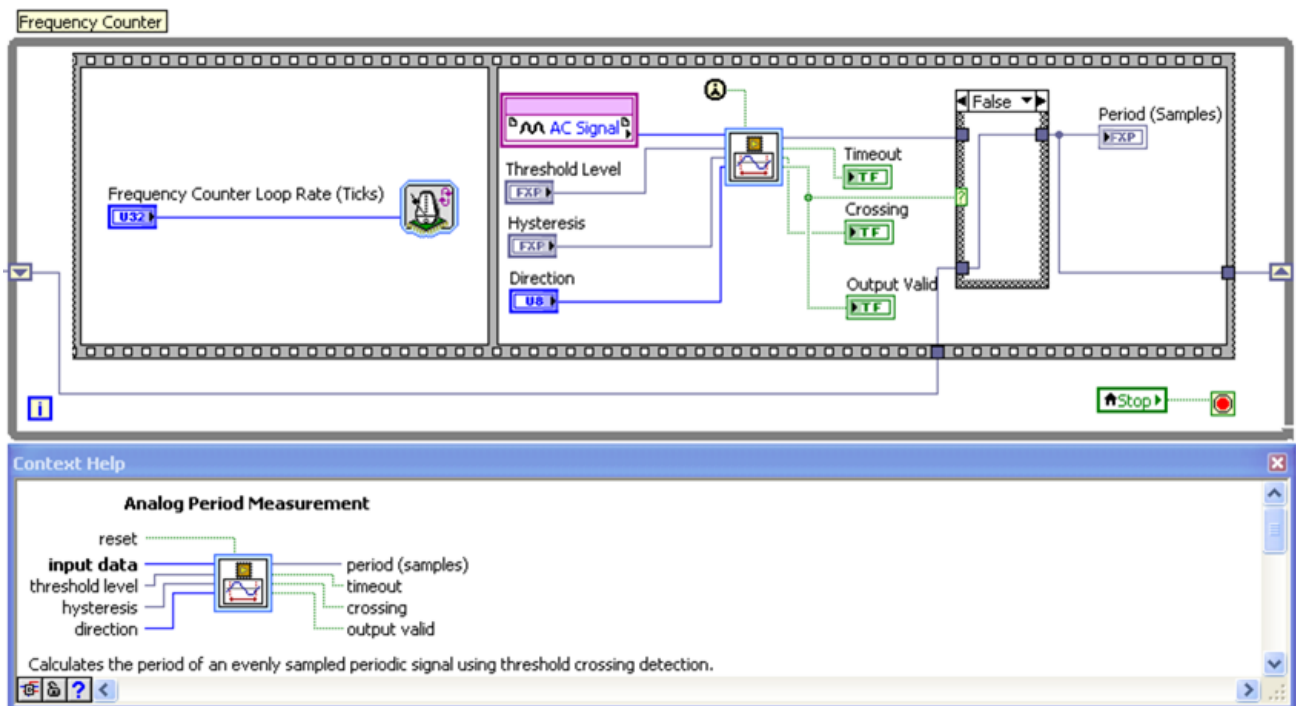


Figure 4.10: A frequency counter to measure the cantilever period in real-time.

one of the 3 available DMA channels. PLL can easily be tested by generating a single frequency tone from a function generator and adjusting “alpha” to control the bandwidth and the time taken for locking. It can easily lock on to the frequency of a self-oscillated cantilever signal and sometimes even to that of a non-excited cantilever. We have also tested the capability of PLL to demodulate the frequency modulated (FM) cantilever signal by inputting a test waveform from a function generator capable of FM. It can detect frequency shifts as small as 1 mHz and the bandwidth of demodulation can be as high as 50 Hz, typical for MRFM experiments. Using “FM Power Spectral Density (PLL).vi”, we can record the frequency fluctuation spectrum (FFS) of the cantilever signal and the noise amplitude spectrum depends on the alpha used which controls the bandwidth. One can calibrate the amplitude of the peak observed in FFS for a given “alpha” and a given amount of mHz FM modulation input supplied from a function generator, and then use it for iOSCAR and CERMIT experiments. We have done such calibration tasks but we haven’t performed MRFM experiments using this PLL so far.

4.6.5 Lock-in filter bank

While doing frequency sweep or iOSCAR/CERMIT experiments, the output from the lock-in amplifier has to be filtered at various time constants to determine the correlation time (Fig. 4.9). This task is done using this VI for both the in-phase and out-of-phase channels. It consists of a bank of ten moving average (MA) decimation filters having a range of time constants (and decimation factors) and the statistics of the spin noise can be plotted in real time using the host VI. In principle, we can add more number of filters without consuming additional multipliers. HF2LI lock-in from Zurich Instruments is also used to implement the filtering functionality described above. It has six dual-phase demodulators and the filter bandwidth for each demodulator can be set independently.

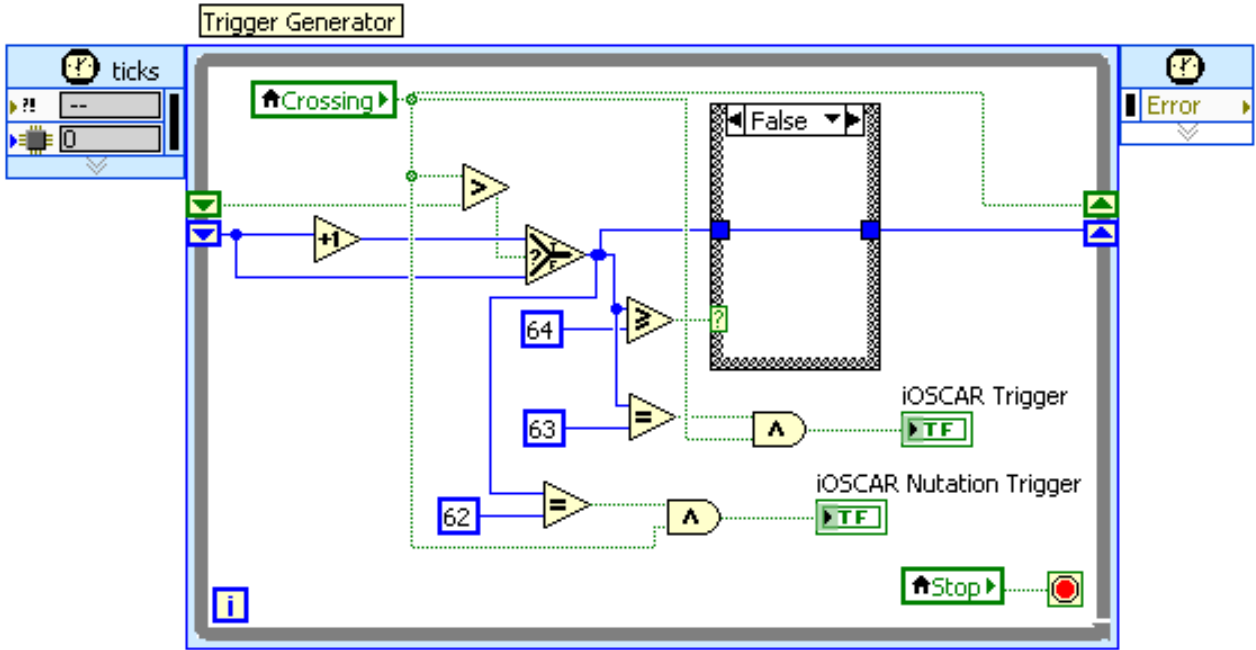


Figure 4.11: A trigger generator generates a trigger every N cantilever cycles.

4.6.6 Frequency counter, trigger and pulse generator

These custom designed functionalities are useful for iOSCAR and CERMIT experiments (Fig. 4.10, Fig. 4.11 and Fig. 4.12). The frequency counter samples the self-oscillated signal at 500 kHz and detects every zero crossing. The pulse generator can generate a iOSCAR/CERMIT pulse every $32T_c$, $64T_c$, $128T_c$ (only in powers of 2) etc. where T_c is the period of the cantilever. It sends a digital trigger to the arbitrary waveform generator using one of the PXI triggers. The quality of the generated CERMIT and iOSCAR pulses was found to be good during testing. We have used a microwire with an integrated nanomagnetic tip to measure the statistical nuclear spin polarization of proton spins by iOSCAR MRFM protocol. The successful demonstration of the compatibility of iOSCAR scheme with a microwire RF source would allow us to perform very sensitive electron spin resonance experiments in a sample-on-cantilever MRFM geometry.

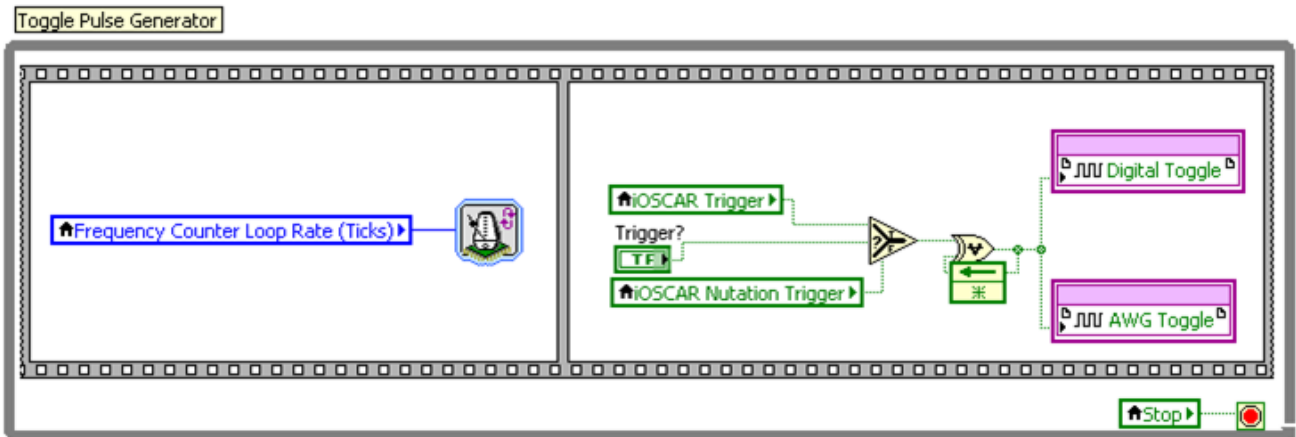


Figure 4.12: A pulse generator to send a digital trigger pulse to the waveform generator.

Chapter 5

Spin Order

The experimental research reported in this Chapter required ~ 6 months of study and constitutes the core of the scientific work presented in this thesis.

5.1 Introduction

Control over the dynamics of nanometer-scale nuclear spin systems is of interest both for fundamental studies and in applications such as quantum information processing and magnetic resonance imaging. Here we achieve such control through mechanical detection of nuclear spins in a semiconductor nanowire (NW) with a magnetic resonance force microscope (MRFM). In contrast to previous experiments, where the intrinsic electron-nuclear feedback mechanisms were employed to control the polarization dynamics [19–22, 50–52], we demonstrate an extrinsic scheme using active real-time control of radio frequency (RF) fields applied to nuclear spins [23]. Using radio frequency pulses, we demonstrate the real-time measurement and state preparation of small-scale nuclear spin ensembles. Our approach takes advantage of real-time feedback control to harness the statistical fluctuations of a nuclear spin ensemble.

Soon after the first measurements of nuclear magnetic resonance (NMR) in a condensed matter system, Bloch [1] predicted the presence of statistical fluctuations proportional to $1/\sqrt{N}$ in the polarization of an ensemble of N spins. First observed by Sleator et al. [7, 53], so-called “spin noise” has recently emerged as a critical ingredient in nanoscale magnetic resonance imaging (nanoMRI) [3, 9, 15, 54]. This prominence is a direct result of MRI resolution improving to better than $(100 \text{ nm})^3$, a size-scale in which statistical spin fluctuations begin to dominate the polarization dynamics. Here we demonstrate a technique that creates spin order in nanoscale ensembles of nuclear spins by harnessing these fluctuations resulting in polarized and narrowed spin distributions. We focus on ensembles containing $\sim 10^6$ phosphorus and hydrogen spins associated with single InP and GaP nanowires

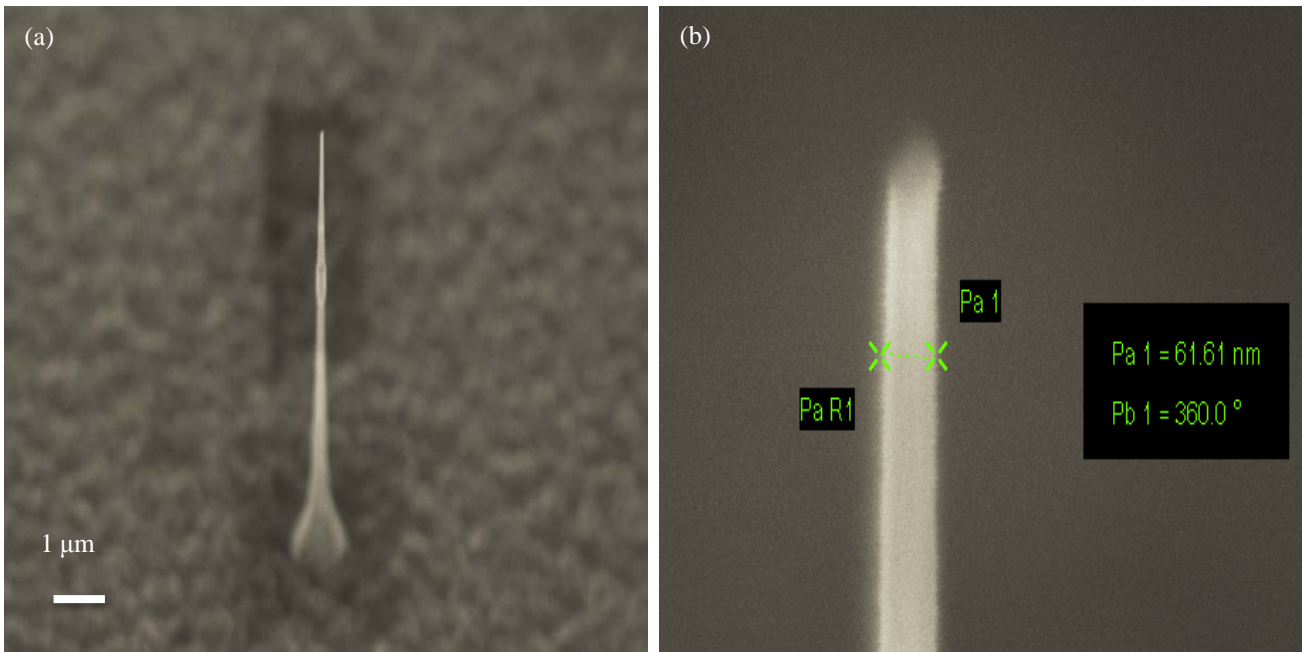


Figure 5.1: SEMs of a representative InP NW. (a) An as-grown InP NW before its attachment to the cantilever tip. (b) A zoomed-in view of the narrow end of the NW, with the Au catalyst particle at the tip.

(NWs) and their hydrogen-containing adsorbate layers. We have developed spin manipulation protocols that allow us to monitor and control fluctuations of the nuclear spin ensemble in real-time. Furthermore, we capture large fluctuations in the ensemble's spin polarization and store them for extended periods. Given that the thermal spin imbalance vanishes as an ensemble shrinks, the selective capture of large polarization fluctuations may provide a route for enhancing sensitivity to the weak magnetic signals produced by nanoscale volumes of nuclear spins. The scheme may also prove useful for initializing the nuclear hyperfine field of electron spin qubits in the solid-state.

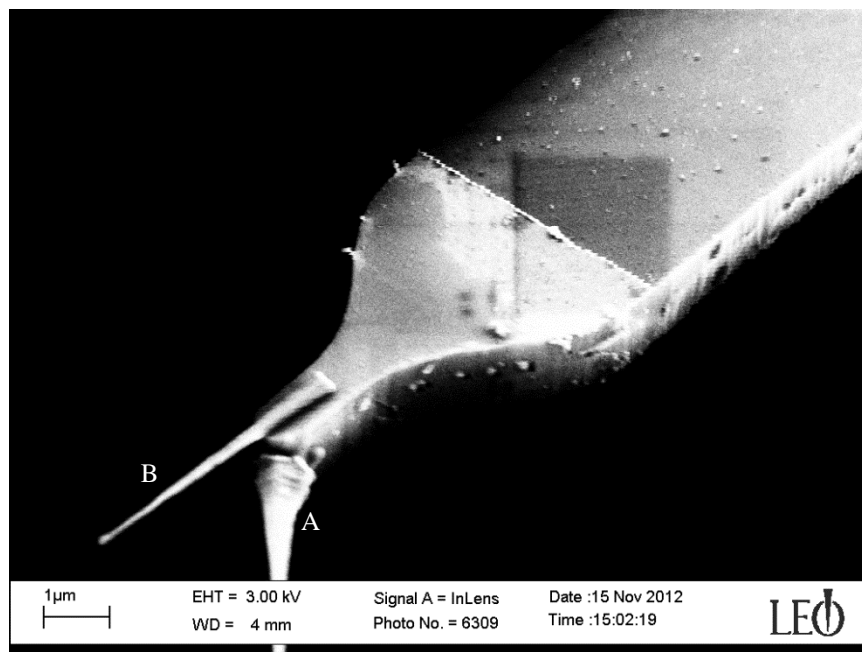


Figure 5.2: This SEM depicts two InP NWs affixed to the Si cantilever which is evaporated with Si/Au (10/30 nm). The nanowire, marked as 'A', is the one likely studied in this experiment due to its greater extension.

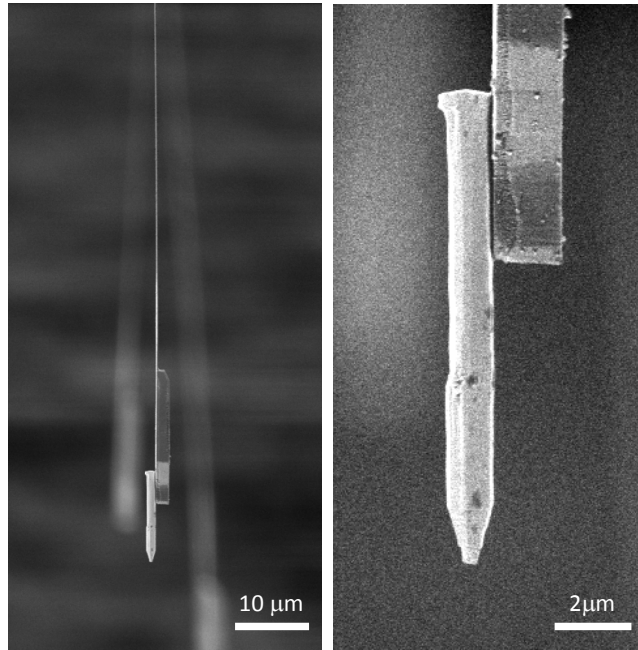


Figure 5.3: SEMs of the GaP NW on the cantilever tip. (left) This SEM depicts the GaP NW affixed to the Si cantilever from the side. (right) A second SEM shows a zoomed-in view of the NW. The cantilever is 100-nm-thick with a 2- μm -thick and 17- μm -long mass at its end.

5.2 Nanowire sample preparation

We study two separate samples: an InP and a GaP NW, both grown with the vapor-liquid-solid method in a metal-organic vapor-phase epitaxy reactor using gold droplets as catalyst [55]. The InP NW is 8 μm -long; its diameter shrinks from 200 nm to 60 nm along its length; and it is tipped by a 60 nm diameter Au catalyst particle, left over from the growth process. The GaP NW is 10 μm -long; its diameter is 1.0 μm ; and it has a 1.5- μm -long tapered tip which reaches 90 nm in diameter at the Au droplet. In this case we remove the Au droplet by cutting of the end of the NW with a focused ion beam, resulting in a 300-nm-diameter GaP tip. Finally, we sputter a 5 nm layer of Pt onto the NW in order to shield electrostatic interactions [56]. Each NW is affixed to the end of the cantilever (Figs. 5.2, 5.3) with less than 100 fL of Gatan G1 epoxy. In the attachment process, we employ an optical microscope equipped with a long working distance and a pair of micromanipulators.

5.3 Nanowire growth

5.3.1 InP nanowire growth

The InP NWs (Fig. 5.1) are grown with the vapor-liquid-solid (VLS) method in a low-pressure (50 mbar) Aixtron CCS-MOVPE reactor. The Au catalyst nanoparticles are dispersed using a 60-nm Au colloidal solution over the InP (111)B substrate. The InP NWs are grown at 420°C for 20 min using Tri-Methyl Indium (TMI) and Phosphine (PH_3) as precursor gases at molar fractions of 2.5×10^{-5} and 8.3×10^{-3} , respectively, with a total flow

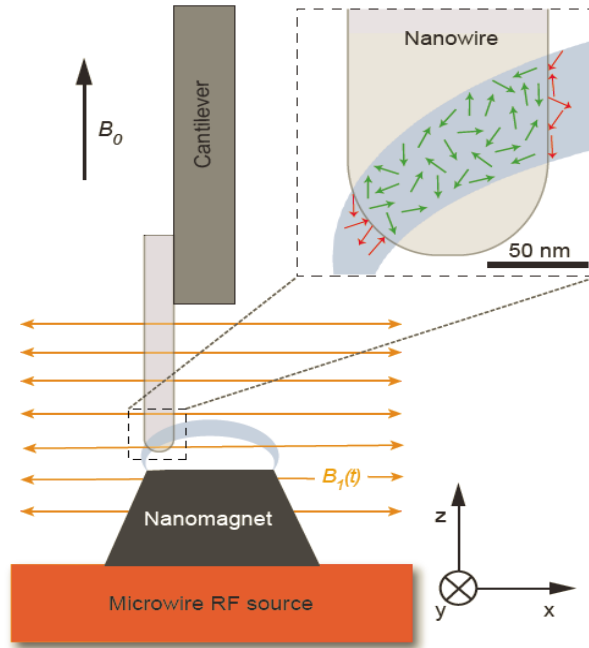


Figure 5.4: Schematic of the experimental geometry. The end of the NW, which is affixed to an ultrasensitive cantilever, is positioned 50-100 nm away from the nanomagnet. Below the tip, a microwire RF source generates ARP sweeps to invert the nuclear spin ensemble within a nanometerscale “resonant slice” (in light blue). Two types of spin ensembles are investigated: one composed of ^{31}P nuclei within the NW lattice (green spins) and another consisting of ^1H nuclei from the thin adsorbate layer on the NW surface (red spins).

of 6.0 l/min using hydrogen as a carrier gas. The Arsine (AsH_3) gas (molar flow 3.3×10^{-4}) is introduced in the reactor chamber for 2 s in order to grow an InAsP quantum dot, followed by 20 min InP growth. The samples are then overgrown for 5 min at 500°C with a InP shell, using TMI and PH_3 at molar fractions of 2.3×10^{-5} and 8.3×10^{-3} , respectively.

5.3.2 GaP nanowire growth

The GaP NWs (Fig. 5.3) are grown with the VLS method in a low-pressure (50 mbar) Aixtron CCS-MOVPE reactor, using Au nanocatalysts deposited in square arrays by e-beam lithography (25 nm - 100 nm diameter, 200 nm - 5 μm pitch) over a zinc blende GaP (111)B substrate [55]. The samples are annealed at 750°C for 8 min and then grown at 750°C for 13 min using Tri-Methyl Gallium (TMG) and Phosphine (PH_3) as precursor gases at molar fractions of 7.4×10^{-5} and 1.7×10^{-3} , respectively, with a total flow of 8.2 l/min using hydrogen as carrier gas. Hydrogen Chloride (HCl) gas (molar fraction 1.2×10^{-4}) is used to suppress the radial overgrowth in the NWs. In order to increase the NW diameter, the GaP shell growth is performed at 690°C for 22 min using TMG and PH_3 as precursor gases at molar fractions of 8.1×10^{-5} and 1.1×10^{-2} , respectively. Next, the $\text{Al}_{0.4}\text{Ga}_{0.6}\text{P}$ shell is grown for 5 min with TMG, TMAI and PH_3 as precursor gases at molar fractions of 2.7×10^{-5} , 1.5×10^{-5} and 1.1×10^{-2} , respectively. The tapered axial segment which can be seen at the top of the NWs is related to the parasitic decomposition of the precursors at the gold droplet during the shell growth.

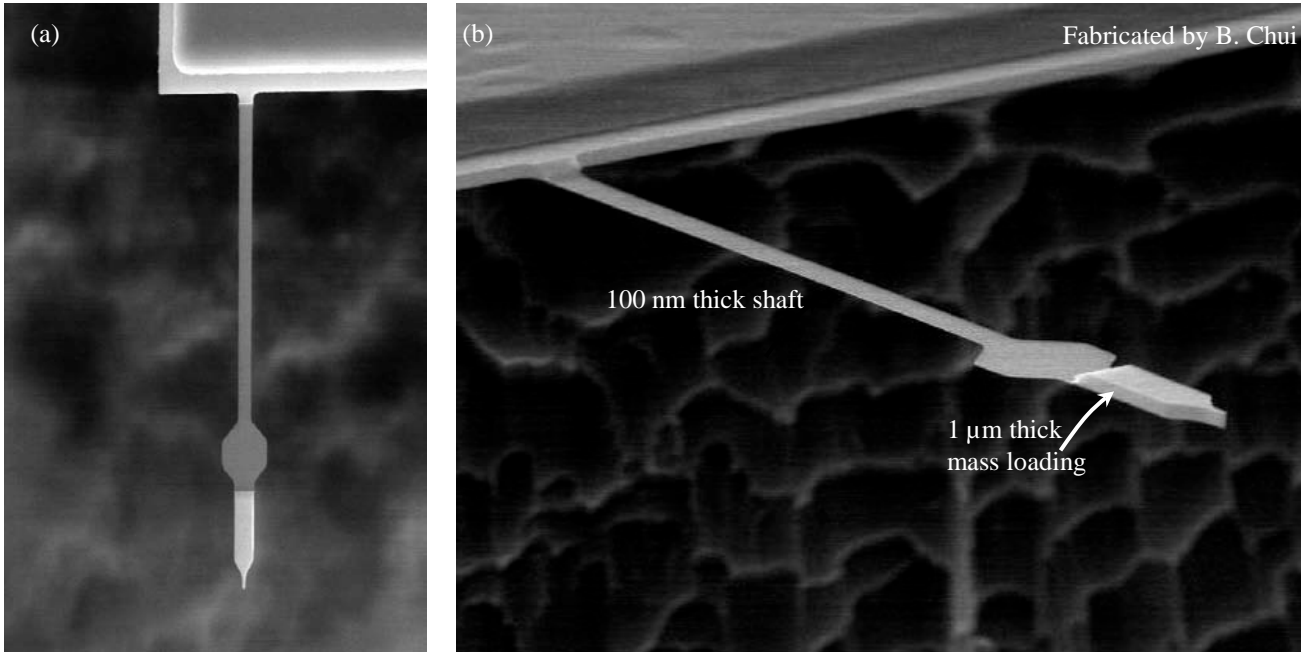


Figure 5.5: SEM micrograph of the Si cantilever. (a) The cantilever is shown protruding from a Si chip. (b) The detailed view shows the paddle and mass-loaded end of the cantilever.

5.4 Experimental details

In a low-temperature ultra-high-vacuum MRFM, the force signal that is detected arises from the interaction between the gradient field of a nanomagnet and the nuclear magnetic moments in the sample. The cantilever, acting as a sensor in MRFM, can be used for the sensitive detection of nuclear spin force signals in nanoscale samples with lateral dimensions below 100 nm. The MRFM experimental setup (Fig. 5.4) consists of an ultrasensitive cantilever mounted perpendicular to the substrate which is patterned with a microwire RF source and an integrated magnetic Dysprosium (Dy) tip [47]. Ultrasensitive cantilevers are made from undoped single-crystal Si and measure $120\ \mu\text{m}$ in length, $4\ \mu\text{m}$ in width, and $0.1\ \mu\text{m}$ in thickness (Fig. 5.5). In vacuum and at the operating temperatures, the NW-loaded cantilevers have resonant frequencies $f_c = 2.4$ and 3.5 kHz, intrinsic quality factors $Q_0 = 3.0 \times 10^4$ and 3.5×10^4 , and spring constants $k = 60$ and $100\ \mu\text{N}/\text{m}$ for the InP and GaP NW experiments respectively. During the measurement, the cantilever is actively damped in order to give it a fast response time of $\tau_c = 65$ ms. A fiber-optic interferometer is used to measure the displacement of the cantilever. Up to 50 nW of laser light at 1550 nm are incident on the cantilever as part of the fiber-optic interferometer. The nanomagnetic tips (Fig. 5.6) are truncated cones of Dy fabricated by optical lithography [57]. For the InP (GaP) NW experiment the tip measures 225 (280) nm in height, 270 (250) nm in upper diameter, and 380 (500) nm in lower diameter. The RF source (Fig. 5.6), on which the Dy tip sits, is a $2\text{-}\mu\text{m}$ -long, $1\text{-}\mu\text{m}$ -wide, and 200-nm-thick Au microwire. The experiments were performed in vacuum pressures better than 1×10^{-6} mbar, at temperatures down to 4 K and in an applied longitudinal field up to $B_{\text{ext}} = 6$ T.

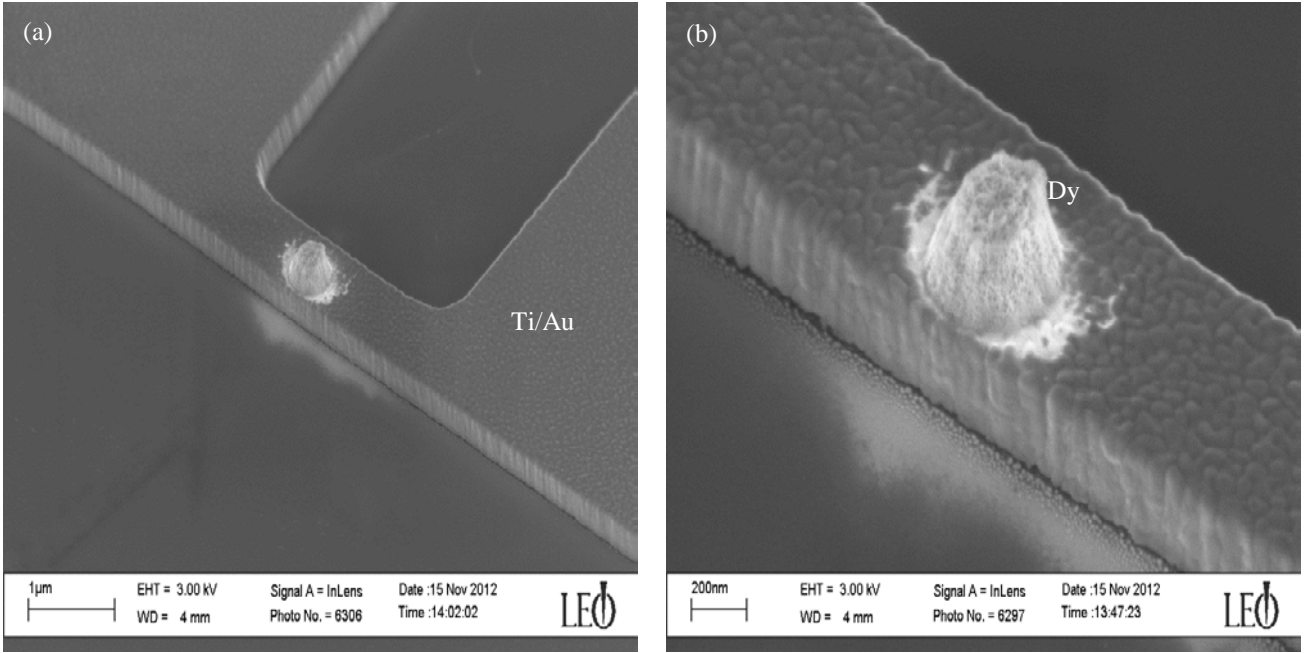


Figure 5.6: SEM micrograph of the microwire. (a) Ti/Au microwire with an integrated Dy tip is patterned on a Si chip. (b) The zoom-in view shows the Dy tip.

We measure the polarization of nanometer-scale ensembles of ^{31}P nuclei within each NW and of ^1H nuclei contained in the hydrocarbon adsorbate layer on the surface (Fig. 5.7, Fig. 5.8). The NW of interest is attached to the end of the cantilever and is positioned within 100 nm of the nanomagnetic tip. A transverse RF field from a microwire is applied to excite nuclear spin resonance. The strong magnetic field gradient ($\geq 10^6$ T/m) of the tip field confines the magnetic resonance to the region that satisfies the condition $\mathbf{B}_0 = \mathbf{B}_{\text{ext}} + \mathbf{B}_{\text{tip}} = \omega/\gamma$, where ω is the frequency of the RF field, γ is the gyromagnetic ratio of the nuclear spin, and \mathbf{B}_0 is the tip field plus an external field from a superconducting magnet. The detection volume can be exposed to spatial magnetic field gradients exceeding 1.5×10^6 T/m and RF $B_1(t)$ fields larger than 20 mT without significant changes in the experimental operating temperature. We use hyperbolic secant adiabatic rapid passage (ARP) sweeps with $\beta = 10$ and a modulation amplitude set to 500 kHz peak-to-peak for ^{31}P and 1 MHz for ^1H [30, 58]. These parameters, combined with the geometry of the sample and the profile of $\partial B_0/\partial x$, determine the size of the detection volume [42].

5.5 ARP sweep detection protocol

In MRFM detection, spins are cyclically inverted by using magnetic resonance, and the net spin projection along the time-dependent effective magnetic field in the rotating frame is detected mechanically by measuring the interaction between a nanomagnetic tip and the spins in the sample. The force generated by a statistically polarized ensemble of nuclear spins ($N \sim 10^6$) on the cantilever is $\sim 10^{-18}$ N when subjected to a magnetic field gradient of 10^6 T/m from the tip. Coherent manipulation of the spins for many cantilever cycles are employed

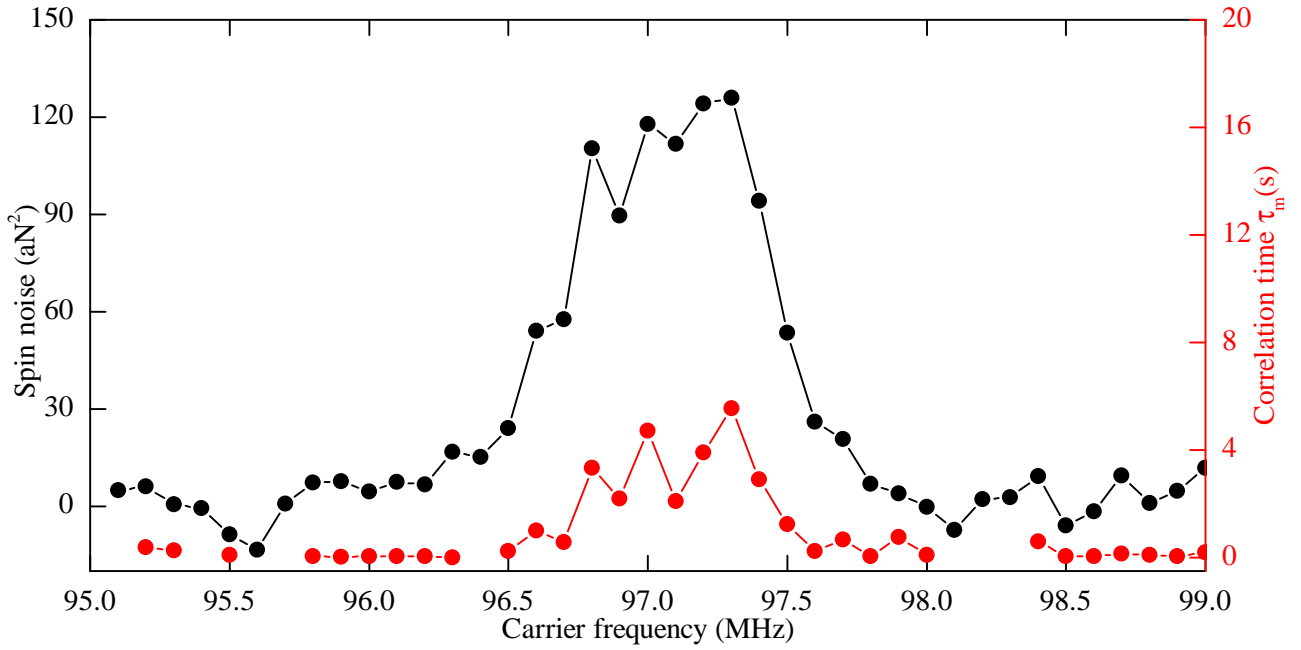


Figure 5.7: MRFM signal from the statistical polarization of ^{31}P nuclear spins. Black and red dots show the resonant force variance of spin noise and the correlation time τ_m as a function of the carrier frequency.

to improve the sensitivity to detect such small forces. Owing to the long spin correlation times τ_m characteristic of nuclear spins, cyclic adiabatic inversions of spins at the cantilever frequency can give rise to an amplitude modulated periodic force on the cantilever. Thus, a time-dependent force due to the nuclear spin polarization signal oscillating in-phase with the cantilever produces an additional displacement of the cantilever.

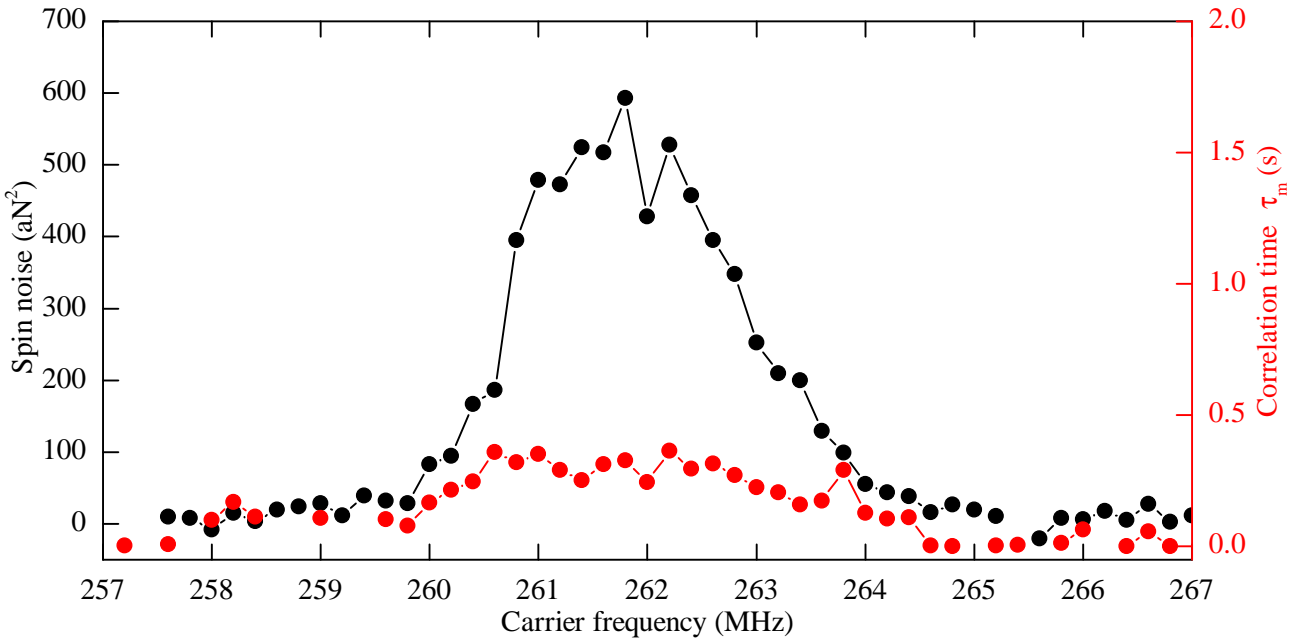


Figure 5.8: MRFM signal from the statistical polarization of ^1H nuclear spins. Black and red dots show the variance of spin noise and the correlation time τ_m as a function of the carrier frequency.

ARP sweeps of the RF field through the Larmor frequency of the spins are used to cyclically invert the polarization of nanometer-scale volumes of a particular nuclear spin isotope. These inversions occur because the spin polar-

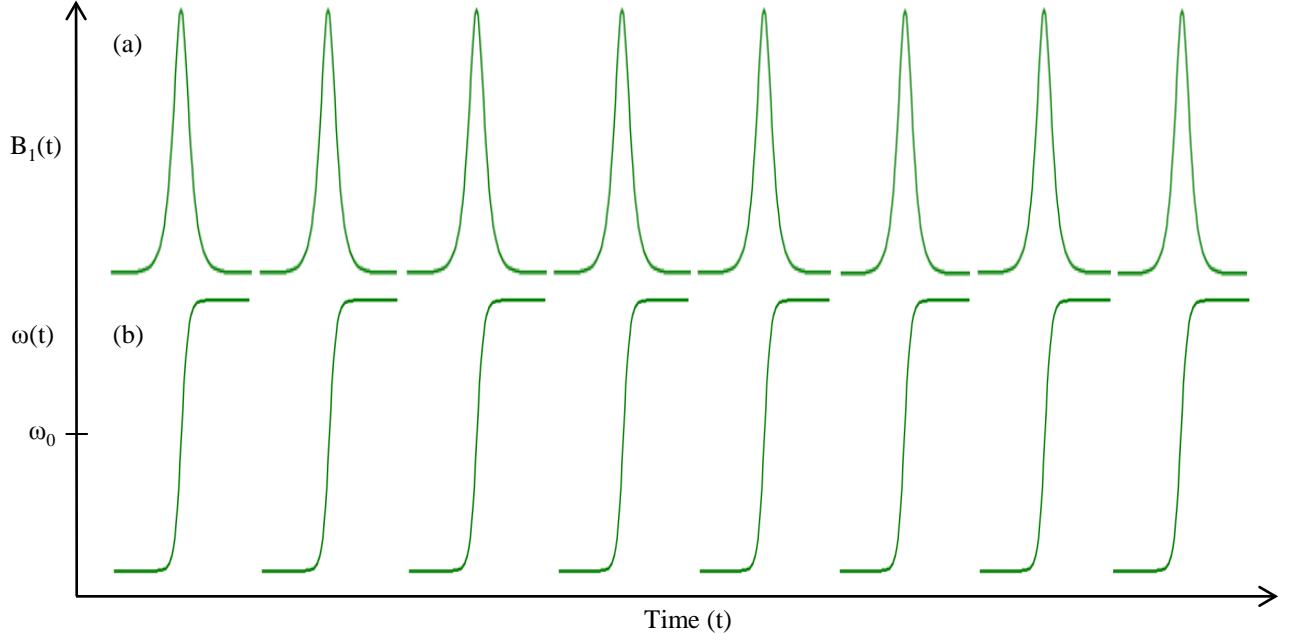


Figure 5.9: Cyclic adiabatic rapid passage (ARP) pulse sequence. Hyperbolic secant ARP pulses are applied twice every cantilever cycle.

ization follows (or is “spin-locked”) to the time-dependent effective field $\mathbf{B}_{\text{eff}}(t) = \left(B_0 - \frac{2\pi f_{\text{RF}}(t)}{\gamma} \right) \mathbf{e}_z + B_1(t) \mathbf{e}_x$ in a frame rotating with the RF field, where $f_{\text{RF}}(t)$ is the instantaneous frequency of the ARP sweeps, $B_1(t)$ their amplitude, and the unit vectors are defined in the rotating frame. In a magnetic field gradient, these periodic inversions generate an alternating force that drives the mechanical resonance of the cantilever; the resulting oscillations, which are proportional to this force, are detected by the fiber-optic interferometer. The volume of inverted spins, known as the “resonant slice”, is determined by the spatial dependence of \mathbf{B}_{tip} and the parameters of the pulses; in these experiments it occupies a volume on the order of $(50 \text{ nm})^3$.

In our MRFM detection protocol, spin inversions are obtained by operating RF field $\mathbf{B}_1(t)$ that is both amplitude modulated and frequency modulated (swept unidirectionally twice per cantilever cycle) using hyperbolic secant pulses (Fig. 5.9). At every extremum of the frequency sweep, $\mathbf{B}_{\text{eff}}(t)$ will have reversed the orientation. This results in a change of the magnetization from locked to antilocked and vice versa every half-cycle of the cantilever, producing a force signal that oscillates at the cantilever frequency. This endows the spin signal with a distinctive signature because of the fact that any spurious cantilever excitation caused by the frequency modulation is at a second harmonic of the cantilever frequency. The cantilever force signal is fed to a lock-in amplifier referenced to the periodic spin inversions and its in-phase (X) and quadrature (Y) amplitudes are monitored. The limiting source of noise in the measurement is the thermal force noise acting on the cantilever. The thermomechanical noise, due to its random phase, is present in both the lock-in channels and on average contributes equally to X and Y . On the other hand, force fluctuations due to the nuclear spin polarization are in phase with the inversion pulses and contribute only to X .

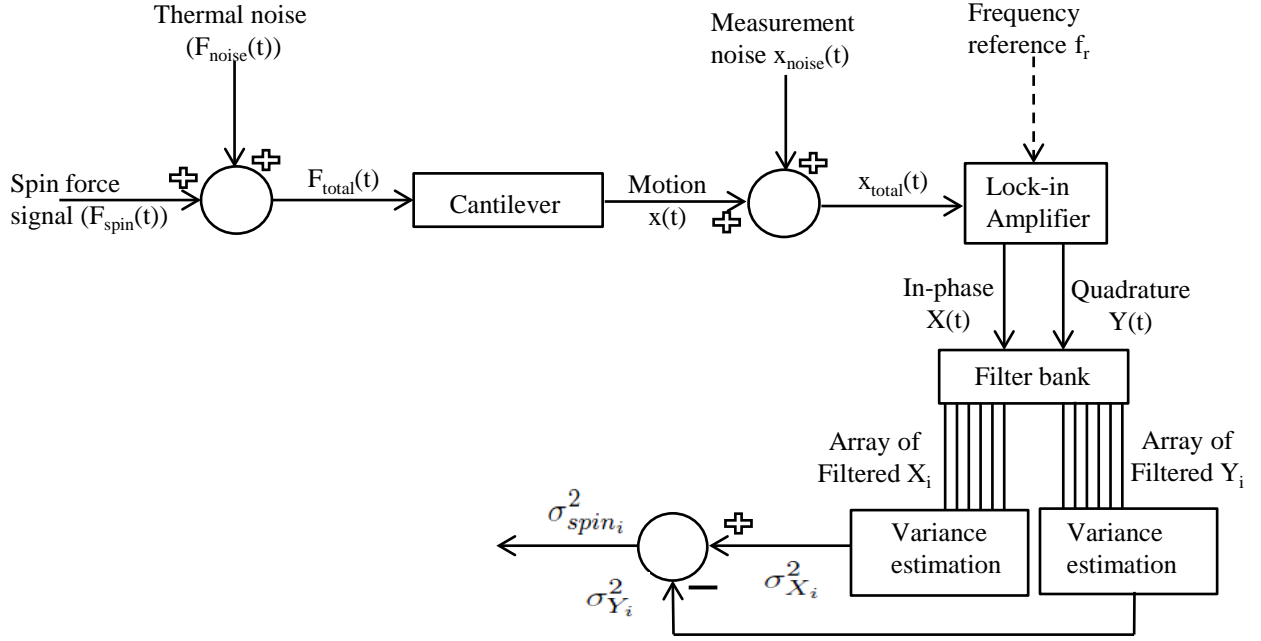


Figure 5.10: MRFM signal processing scheme. By measuring σ_{spin}^2 as a function of detection bandwidth of the filter, the spin signal variance and the correlation time τ_m of the spin signal can be determined.

The nuclear spin polarization in the rotating frame evolves in time under the influence of the random magnetic field fluctuations caused by the thermal (Brownian) motion of high-frequency modes of cantilever vibrations in the presence of a large field gradient [32]. Since fluctuating polarization signals have a time dependence that is a priori unknown and the signal varies randomly in time, measurement over a total averaging interval T long compared to the spin correlation time results in a zero average signal [8, 59]. In this situation, information about the fluctuations is contained in the measured signal variance, provided the random spin correlation time τ_m satisfies: $\tau_c \ll \tau_m \ll T$ where τ_c is the cantilever period (Fig. 5.10). The cancellation of the thermomechanical cantilever excitation caused by the reservoir is accomplished by measuring the variance of the cantilever amplitude for both the channels and subtracting the quadrature variance (σ_Y^2) from the in-phase variance (σ_X^2) to compute the spin signal ($\sigma_{spin}^2 = \sigma_X^2 - \sigma_Y^2$). The frequency modulation amplitude of RF sweeps determines the effective thickness of the resonant slice, and thus the number of spins contributing to the signal. The variance of the oscillating noise force from the spins is given by $\sigma_{spin}^2 = N\mu^2G^2$, where G is the average tip field gradient, N is the number of spins in the slice and μ is the nuclear spin magnetic moment.

5.6 Nuclear spin noise simulations

MATLAB simulations allow us to determine the total spin noise $M_N(t)$ of an ensemble of N spins by adding the individual time traces of each nuclear spin (Appendix B). The time evolution of each spin $\mu_i(t)$ is treated as a random process that is discrete in amplitude but continuous in time, the so-called random telegraph process. At any time instant, $\mu_i(t)$ takes on one of two possible states $+\mu$ and $-\mu$. Each spin switches energy levels in a random manner in time due to the interactions with the environment and the time intervals of jumps

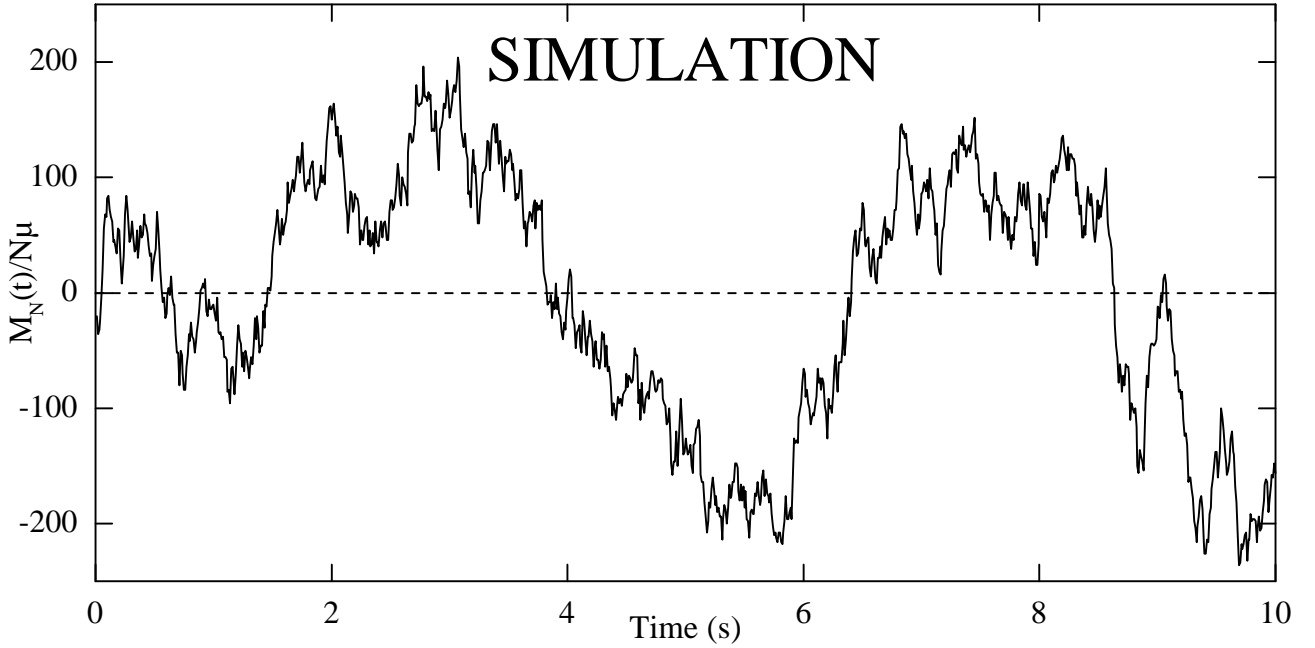


Figure 5.11: A typical time trace of the spin noise simulation of an ensemble of 10000 spins with a correlation time $\tau_m=1$ s.

are described by a Poisson process. $M_N(t)$ is calculated by summing N possible realizations for $\mu_i(t)$, i.e., $M_N(t) = \sum_{i=1}^N \mu_i(t)$ (Fig. 5.11). The simulated statistical fluctuations of the nuclear spin ensemble qualitatively resembles the measured time traces of the spin noise.

5.7 Real-time measurement

The time trace obtained from the lock-in channels is filtered with different bandwidths, which are slow enough to filter out the thermally induced vibrations but fast enough to probe slow random variations of the nuclear spin polarization [25]. The filter time constants are set depending on the correlation time of the spins and the thermal cantilever displacement noise. Thus, as shown in Fig. 5.12, we can monitor $Y(t)$, the thermal force, and $X(t)$, the thermal force plus the force due to the nuclear spin inversions. $X(t)$ is dominated by the large fluctuations and the long τ_m of the spin noise, while the thermally induced displacement of the cantilever $Y(t)$ has a smaller amplitude and a shorter correlation time set by the damped cantilever force sensor. τ_m is limited by the magneto-mechanical noise originating from the thermal motion of the cantilever in a magnetic field gradient and by the ARP pulse parameters [32]. Since the contribution of the spin signal to $X(t)$ is large enough, we can follow – in real-time – the instantaneous nuclear spin imbalance in the rotating frame.

Fig. 5.13 shows the variances σ_X^2 and σ_Y^2 , which give the variance due only to the thermal noise $\sigma_T^2 = \sigma_Y^2$ and the variance due only to the spin noise, $\sigma_S^2 = \sigma_X^2 - \sigma_Y^2$. σ_S^2 is in turn related to the number of nuclear spins in the detection volume. The typical size of the spin ensembles we measure is between 2×10^5 and 7×10^5 for ^1H and

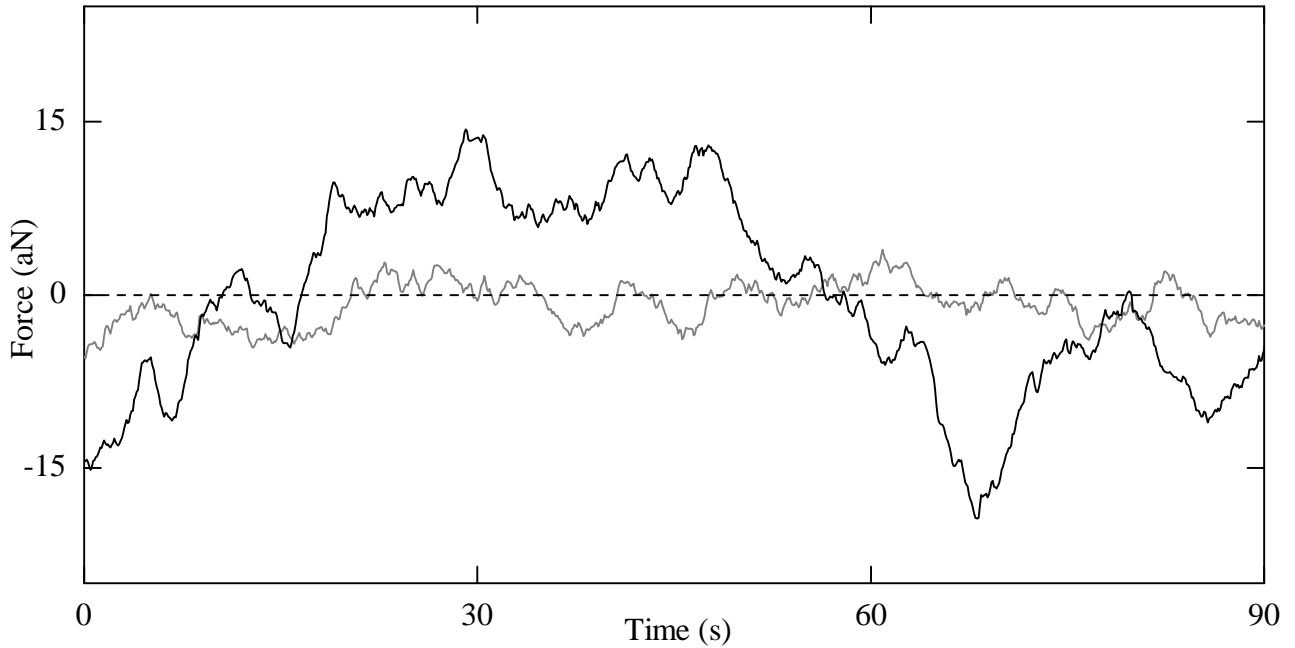


Figure 5.12: Spin noise from an ensemble of $6 \times 10^5 < N < 1 \times 10^7$ ^{31}P spins in an InP NW. (a) Time trace recorded in the in-phase $X(t)$ (black) and quadrature $Y(t)$ (light gray) channels of the cantilever displacement fluctuations demodulated at the cantilever frequency. $T = 4.2$ K and $B_{\text{ext}} = 6$ T. The lock-in time constant is set to be $\tau_l = 5$ s, in order to match the correlation time $\tau_m = 3.6$ s of the spin fluctuations and to filter out the cantilever's thermal displacement fluctuations with a correlation time $\tau_c = 65$ ms. The measured force fluctuations in the in-phase channel is dominated by the spin signal rather than thermal noise. The baseline noise level in the quadrature channel limits the MRFM detection sensitivity to be roughly 250 ^{31}P nuclear spins rms.

between 6×10^5 and 1×10^7 for ^{31}P . Given the density of typical adsorbate layers and InP and GaP, the detection volumes discussed here are between $(13 \text{ nm})^3$ and $(21 \text{ nm})^3$ for ^1H and between $(30 \text{ nm})^3$ and $(80 \text{ nm})^3$ for ^{31}P .

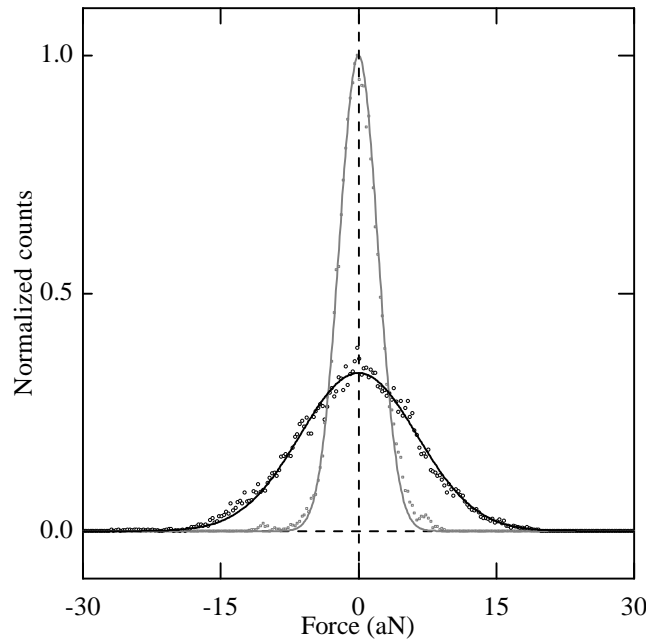


Figure 5.13: Histogram of the in-phase fluctuations is constructed with the lock-in signal recorded for 1 hour. The black curve is a Gaussian fit to the histogram with a standard deviation 6.4 aN. For comparison, histogram of the quadrature channel (light gray) shows that the variance of the thermal noise is ~ 9 times smaller.

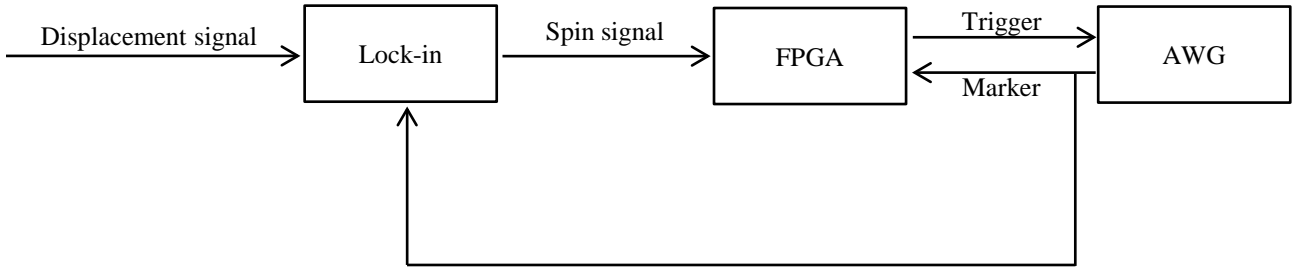


Figure 5.14: Real-time communication among the measurement hardware.

5.8 Real-time control

This near real-time measurement of polarization allows us to apply short RF π -inversion pulses to rectify and narrow the fluctuations of the spin ensemble [23]. High frequency coaxial lines connected to the microfabricated RF wire allow rapid changes of RF waveforms, which in turn are generated by a large bandwidth arbitrary waveform generator (AWG) hardware (Fig. 5.14). The feedback method uses FPGA hardware to measure the polarization in real-time. We run the ARP sweeps until the polarization reaches a predetermined threshold, at which point the AWG hardware switches to a π -inversion pulse having the duration of one cantilever cycle (Fig. 5.15, Fig. 5.16). As a result, the spin ensemble's periodic inversion at the cantilever frequency undergoes a 180° phase shift. After the completion of π -inversion, the AWG hardware switches back to the original ARP sweeps for measuring polarization.

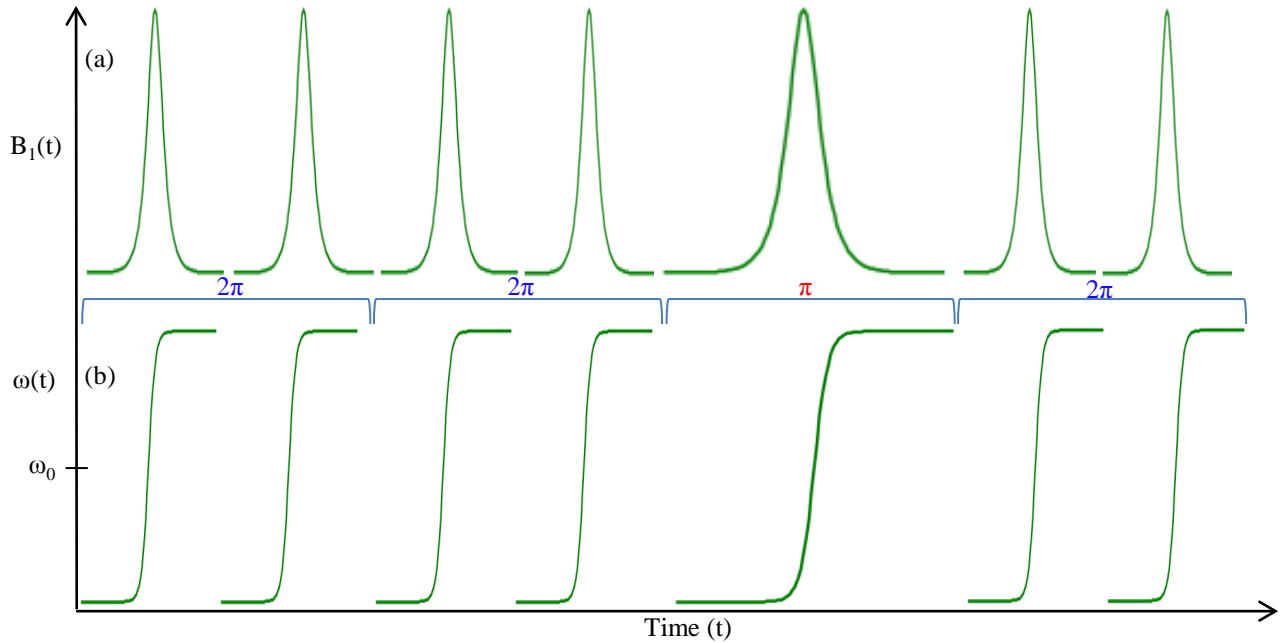


Figure 5.15: Pulse sequence showing a π -inversion. An adiabatic inversion pulse with a duration equivalent to a full cantilever cycle is applied.

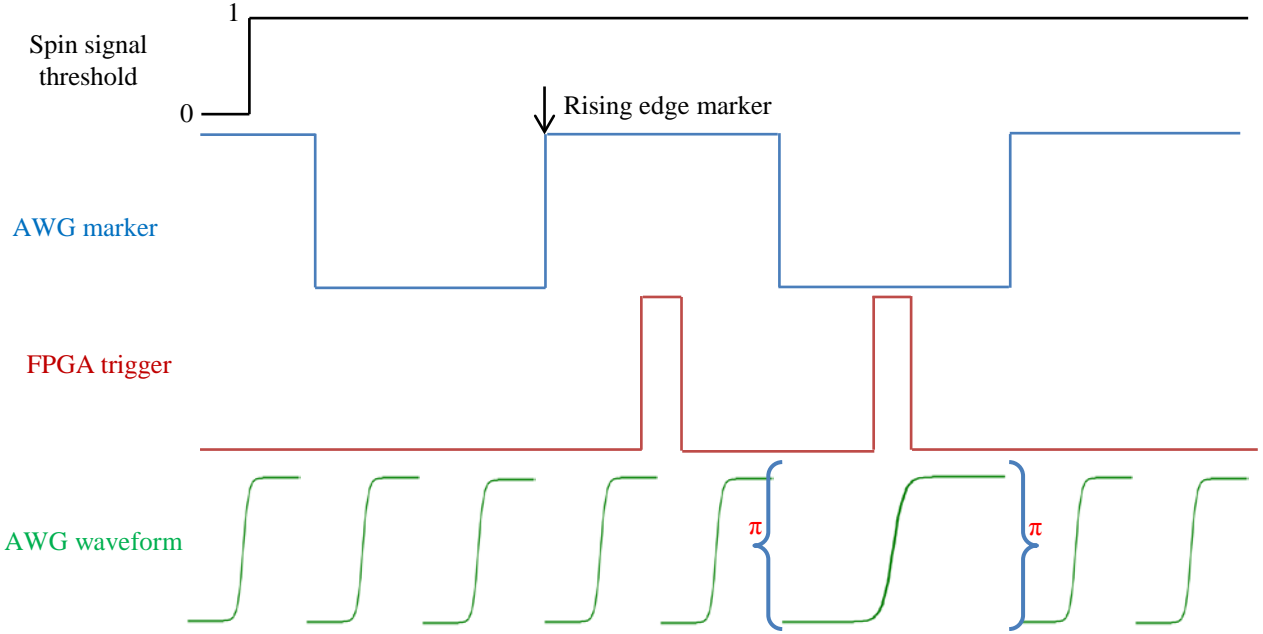


Figure 5.16: Timing diagram for the π -inversion protocol. FPGA triggering routine starts on the rising edge marker. The pulse is precisely timed to last one full cantilever cycle.

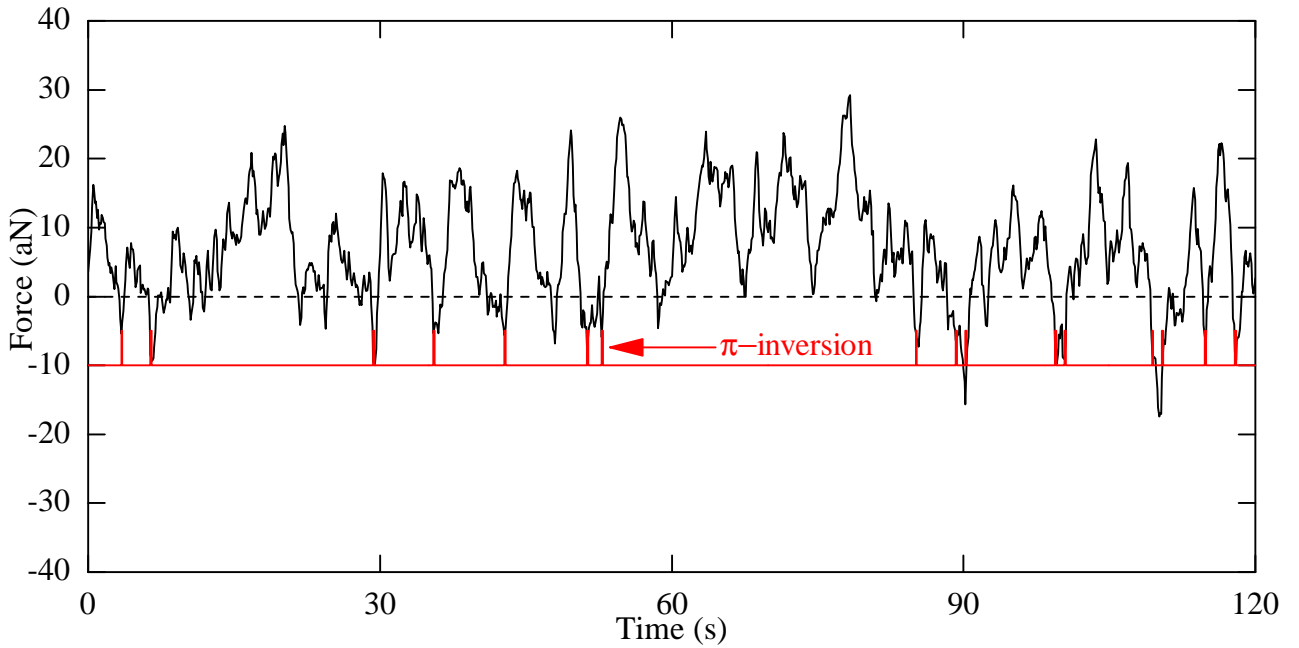


Figure 5.17: A time-trace of the hyper-polarized spin fluctuations recorded with a rectification threshold set to -5 aN. Positive spin polarization is maintained using active feedback during the course of the measurements. The time instants at which the π -inversions are applied are indicated by the red vertical bars. $\tau_l = 0.8$ s.

5.9 Non-equilibrium spin states in the rotating frame

Experimentally, we can monitor the effect of π -inversions by measuring the time traces of polarization. We find that the repetitive application of π -inversions can be used to control and maintain the polarization fluctuations with the same sign - positive or negative (Fig. 5.17), and can also be used to confine the polarization fluctuations

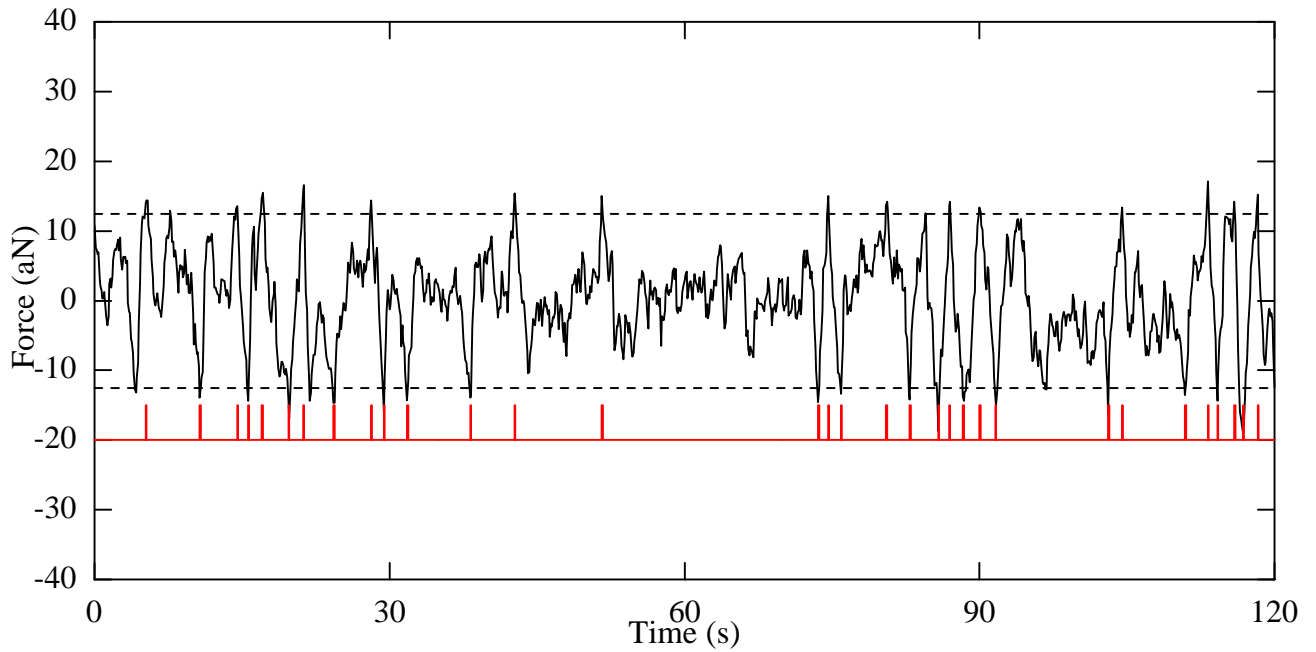


Figure 5.18: A time-trace of the narrowed spin fluctuations. A π -inversion (red vertical bar) is applied whenever the absolute value of the fluctuations exceed a threshold of 12.5 aN. $\tau_l = 0.8$ s

within a certain window (Fig. 5.18). Since only fluctuations due to nuclear spins are affected by the π -inversions, the effectiveness of the protocol depends on the component of $X(t)$ arising from spin compared to thermal fluctuations, i.e., the larger the power signal-to-noise ratio (SNR) σ_S^2/σ_T^2 is, the more effective the control of $X(t)$ will be. As shown in Fig. 5.19, this process can produce both hyper-polarized and narrowed nuclear spin distributions in the rotating frame. Therefore, our ability to continuously measure and manipulate spin polarization enables us to polarize or narrow its distribution using real-time feedback.

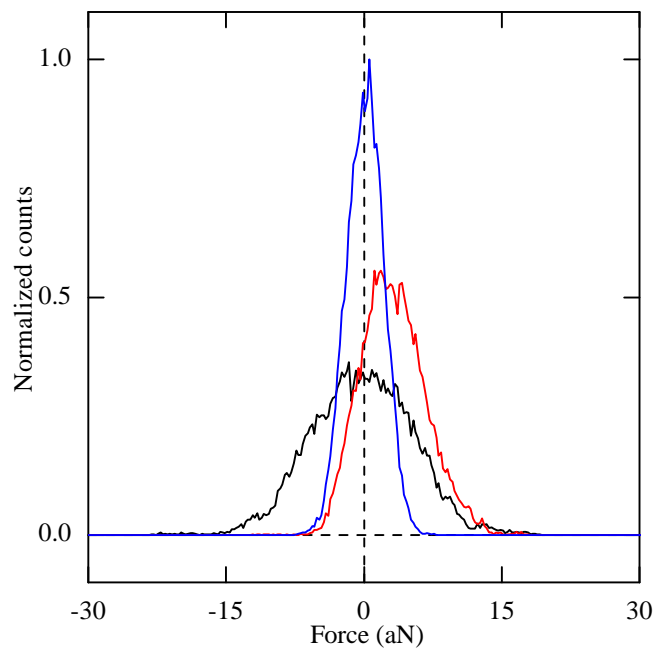


Figure 5.19: Histograms of $X(t)$ recorded over 1 hour corresponding to the natural (black), rectified (red), and narrowed (blue) cases. The mean polarization of the rectified distribution is 2.9 aN compared with 0.0 aN of the natural distribution. The standard deviation of the narrowed distribution is 2.0 aN, compared with 5.6 aN of the natural distribution.

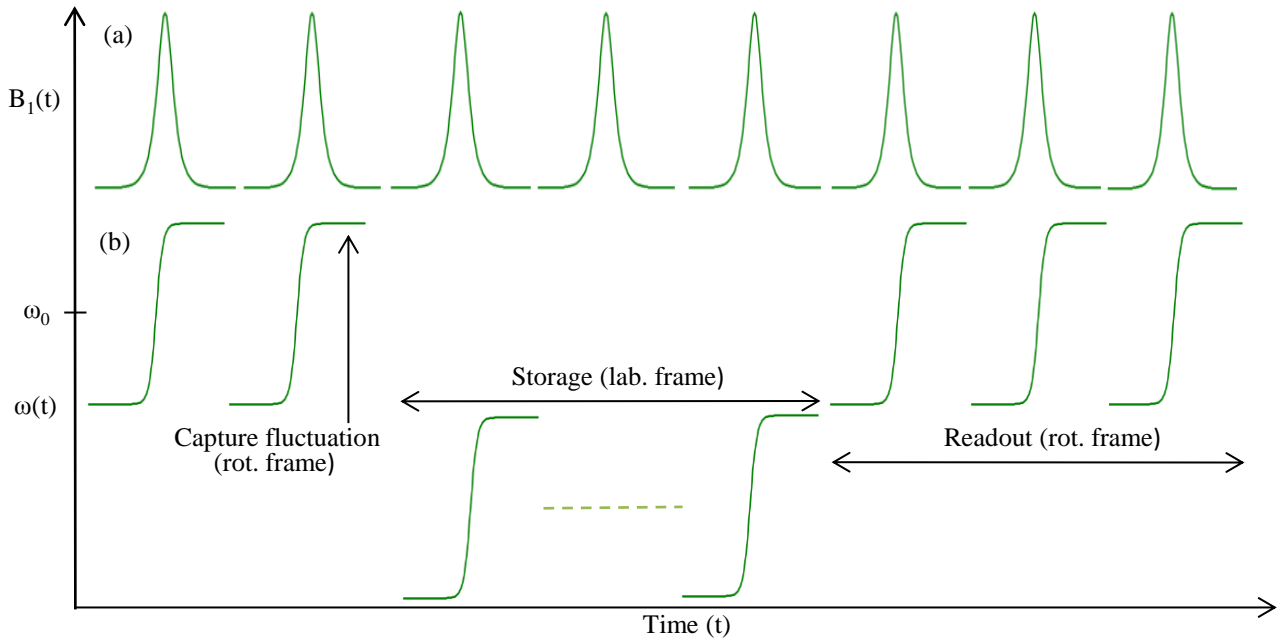


Figure 5.20: Capture-store-readout pulse sequence.

5.10 Capture-store-readout pulse sequence

In addition to controlling the spin fluctuations in real-time, we can also take a less active approach by simply selecting and storing the large statistical polarization fluctuations [23]. The fast nuclear spin fluctuations in the rotating frame can be captured and projected onto the laboratory frame using real-time RF control techniques. Using this approach, the nuclear spin polarization can be stored in the laboratory frame for time periods that exceed their lifetime in the rotating frame. Once prepared, this non-equilibrium nuclear spin state can be readout at a later time and it eventually recovers equilibrium fluctuations on the same time scale as the spin correlation time in the rotating frame. Although the capture-store-readout (CSR) pulse sequence generates only a modest net nuclear spin polarization ($< 1\%$), the resulting nuclear spin state has its variance reduced by a factor of six.

As a second demonstration of creating nuclear spin order, we continuously monitor the spin fluctuations $X(t)$ until they reach a predetermined threshold X_c in the rotating frame (Fig. 5.20). Upon registering a threshold, the spin order is transferred to the laboratory frame by detuning the ARP sweeps from resonance. This leaves the instantaneous spin polarization pointing along \mathbf{B}_0 and the sweeps have no discernable effect on the cantilever amplitude as the cantilever experiences only thermal excitations. In other words, the z-component of polarization is essentially left static and out-of-lock when the sweeps are off-resonance. In this manner, hyper-polarized states of the spin ensemble can be captured and stored in the laboratory frame for as long as T_1 relaxation time.

After some storage time T_{store} , the ARP sweeps are reapplied through the Larmor frequency of the spins to readout the stored nuclear spin state, and the nuclear spin fluctuations are observed again (Fig. 5.20). By bringing

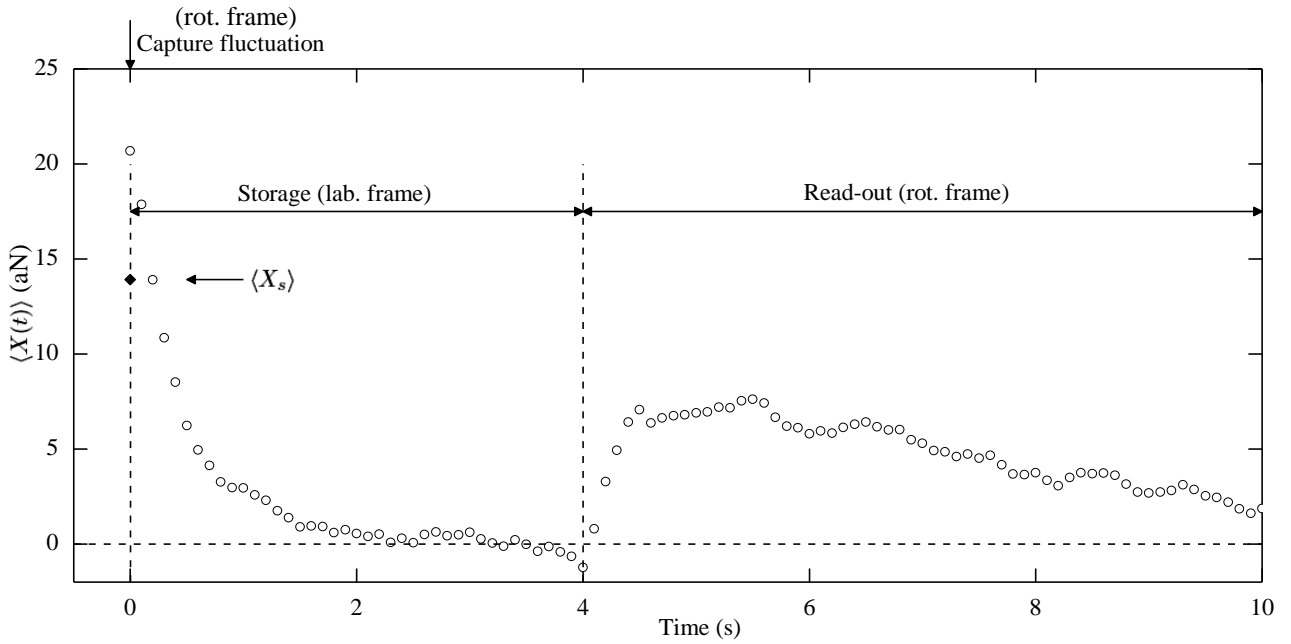


Figure 5.21: $\langle X(t) \rangle$ averaged over 100 CSR pulse sequences showing $T_{\text{store}} = 4$ s for a ^{31}P spin ensemble in a GaP NW. The mean stored fluctuation $\langle X_s \rangle$ is shown as a filled diamond. $T = 4.2$ K and $B_{\text{ext}} = 6$ T. The residual signal observed after the capture arises from the memory effect of the lock-in filter with a time constant $\tau_l = 0.4$ s. The read-out fluctuations decay over a time $\tau_m = 3.8$ s.

the spins into magnetic resonance, the magnetic moments at a given sample location are once again “spin-locked” to the effective field in the rotating frame and undergo periodic inversions at the cantilever frequency because of the frequency modulation of the RF field. In other words, the z-component of polarization oscillates in response to the adiabatic frequency sweeps when the sweeps are on-resonance.

To confirm that the signal is due to storage in the nuclear spins, the experiment is repeated with non-resonant ARP sweeps to capture a fluctuation; no nuclear spin state is recovered in this case. It is important to note that the captured spin fluctuation is transient and only the projection of this state onto the laboratory frame that is stored. Crucially, the time to capture and to retrieve the nuclear spin state occurs over a time scale given by the inverse of the cantilever frequency, which is much shorter than the time scale involved in the spin dynamics in the rotating frame.

The interaction of the nuclear spins with the magnetic field fluctuations at the Rabi frequency can give rise to longitudinal nuclear spin transitions and decrease the correlation time τ_m of the statistical nuclear polarization in the rotating frame compared to that in the laboratory frame. Near a magnetic tip, field fluctuations originate from thermally driven random vibrations of low-frequency mechanical modes of the cantilever [32]. In the presence of the modulation of the RF frequency $\omega_{\text{RF}}(t)$, one might expect such interactions to be sensitive to noise in a frequency band set by $\gamma B_1 \leq \omega_{\text{eff}}(t) \leq \gamma B_{\text{eff}}(t)$ where $B_{\text{eff}}(t) = \sqrt{B_1^2(t) + (\omega_{\text{RF}}(t)/\gamma - B_0)^2}$ is the effective magnetic field in the rotating frame.

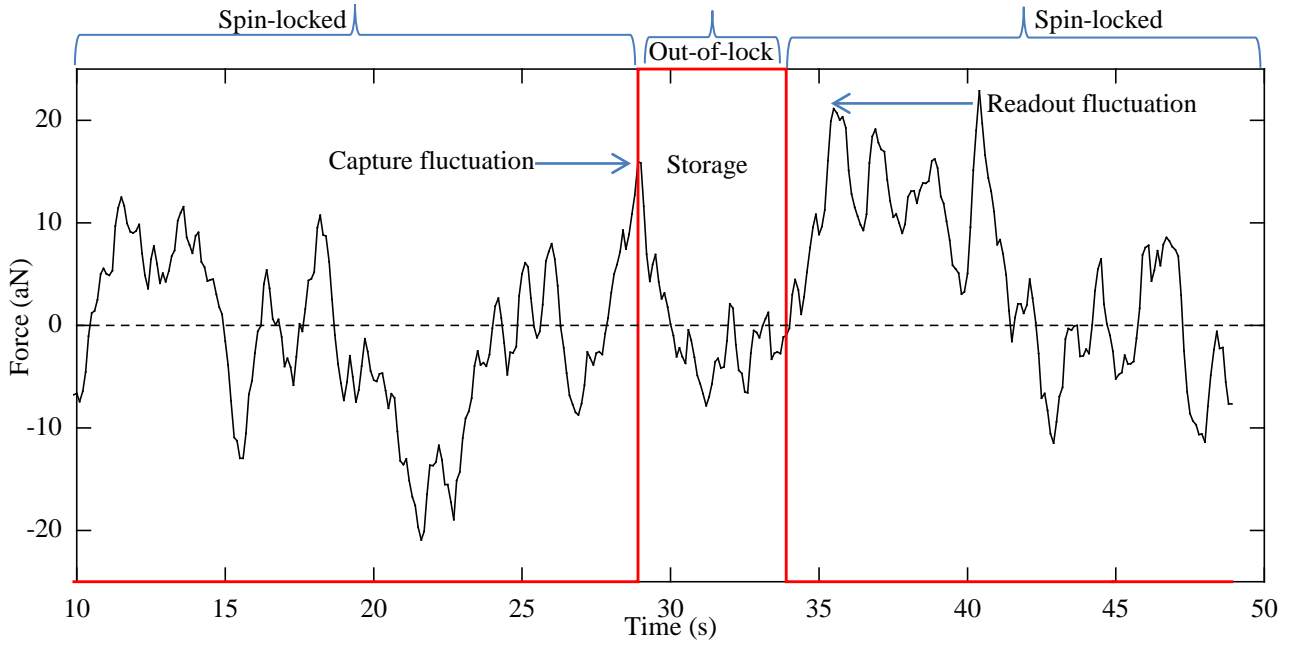


Figure 5.22: Time trace showing an individual capture-store-readout sequence with a storage time of 5 s.

We calculate the ensemble averages $\langle X(t) \rangle$ and $\langle Y(t) \rangle$ by performing multiple independent measurements on nanometer-scale ^{31}P and ^1H ensembles (Fig. 5.21). Because of the randomness of the cantilever thermal noise, ensemble average over many measurements results in a near zero average signal $\langle Y(t) \rangle = 0$. Fig. 5.22 shows a time record of the cantilever fluctuations in an individual capture-store-readout sequence for ^{31}P nuclei.

To determine the time scale T_1 on which the nuclear spin polarization can be stored in the laboratory frame, we captured a polarization within the resonant slice and watched its relaxation back to the equilibrium for varying storage times. As shown in Fig. 5.23 and Fig. 5.24, $\langle X_r \rangle$ and τ_m are extracted from bi-exponential fits to $X(t)$ during the readout sequence using our knowledge of the lock-in time constant τ_l . Deviations of $\langle X_r \rangle$ from $\langle X_s \rangle$ could be caused by the spin-lattice relaxation of the polarization in the laboratory frame – set by T_1 – or by the incomplete projection of the polarization onto \mathbf{B}_0 . For both ^{31}P and ^1H in Fig. 5.23 and Fig. 5.24, these deviations are negligible within our error for two values of T_{store} . Limitations of the experimental hardware prevented measurements for larger T_{store} , although our data show that $T_1 \gg 20$ s for ^{31}P in InP and $T_1 \gg 2.5$ s for ^1H on GaP at 4.2 K.

The size of the captured spin fluctuation is, in principle, only limited by the amount of time one is willing to wait during the capture step. For the normally distributed random variable $X(t)$, the average amount of wait time required to capture a fluctuation X_c is given by $T_{\text{wait}} = \frac{2}{n_0} e^{X_c^2/(2\sigma_X^2)}$, where n_0 is the average number of times $X(t)$ crosses zero per second [60]. For example, given that $n_0 = 0.2$ Hz is a typical value in our experiments, fluctuations of $3\sigma_X$ are expected after just $T_{\text{wait}} = 15$ min, or alternatively for $T_{\text{wait}} = 1$ hr, a fluctuation of $3.4\sigma_X$ can be expected. For a ^{31}P spin ensemble with $N = 10^6$ at $B = 6$ T and $T = 4.2$ K, the standard deviation

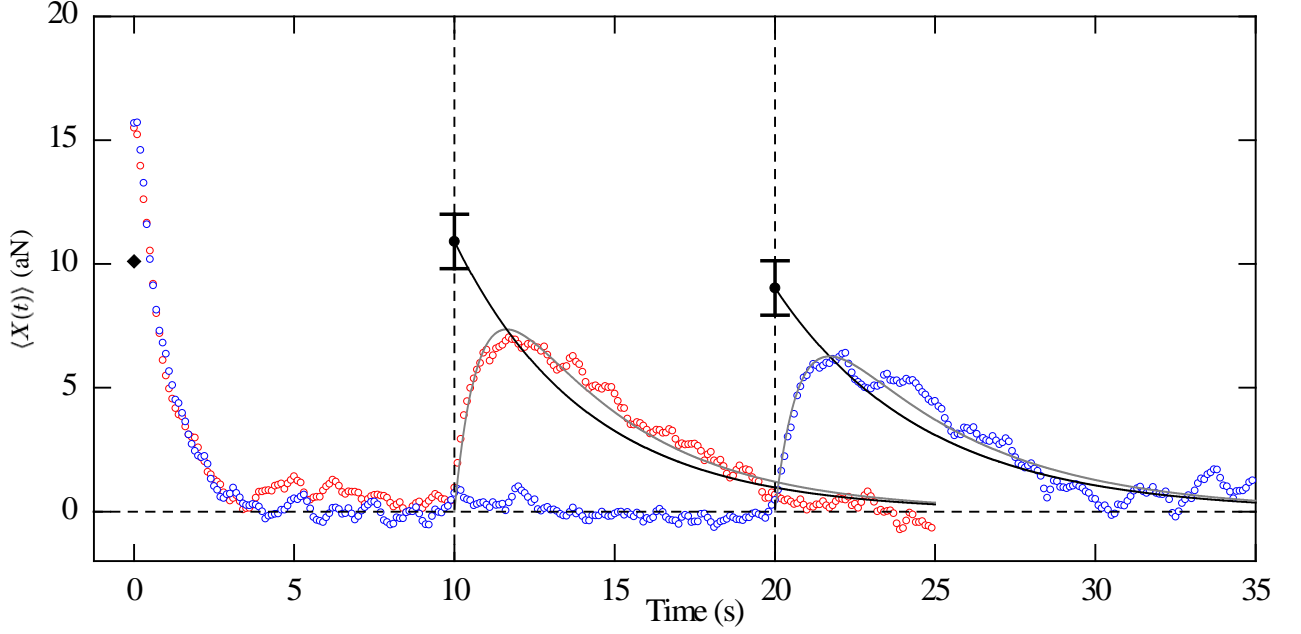


Figure 5.23: Two capture-store-readout sequences are shown for different T_{store} for an ensemble of $6 \times 10^5 < N < 1 \times 10^7$ ^{31}P spins in an InP NW. Fits to $X(t)$ during the readout take into account the lock-in time constant $\tau_l = 0.8$ s (grey) and allow us to recover the value of the retrieved fluctuation $\langle X_r \rangle$ (filled circles) and its exponential decay with $\tau_m = 4.3$ s without the effect of τ_l (black). The filled diamond indicates the mean stored fluctuation $\langle X_s \rangle$. $T = 4.2$ K and $B_{\text{ext}} = 6$ T.

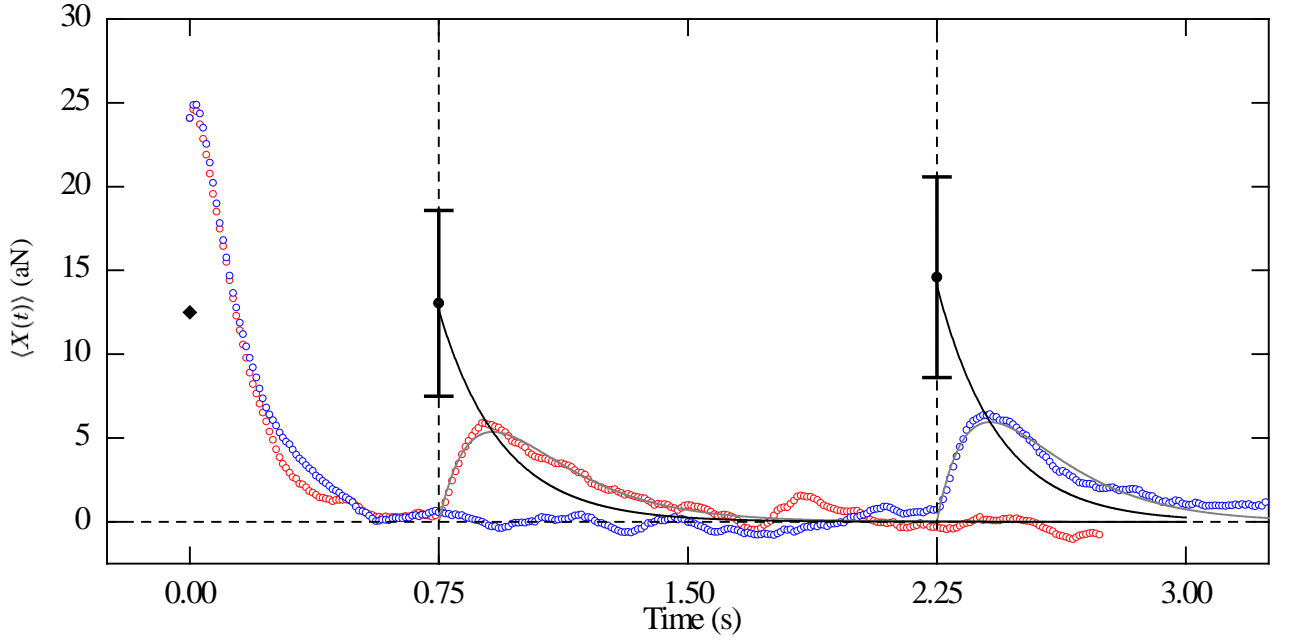


Figure 5.24: Two CSR sequences are shown for different T_{store} for an ensemble of $2 \times 10^5 < N < 7 \times 10^5$ ^1H spins in a GaP NW with $\tau_l = 140$ ms where τ_m is found to be 190 ms. Again $\langle X_r \rangle$ are displayed as filled circles and $\langle X_s \rangle$ as a filled diamond. $T = 4.2$ K and $B_{\text{ext}} = 6$ T.

of the statistical polarization fluctuations is given by $\rho_S = \sqrt{\frac{I+1}{3I} \frac{1}{N}} = 0.1\%$ and its mean thermal polarization is $\rho_B = \frac{I+1}{3} \frac{\hbar\gamma B}{k_B T} = 0.06\%$ [42]. Therefore, in the limit of large SNR where σ_X is dominated by spin fluctuations, we can expect to capture polarizations of $4.8\rho_B$ in 15 min and $5.5\rho_B$ in 1 hr. The polarization captured in a given T_{wait} could be increased even further by reducing τ_m and therefore increasing n_0 , e.g. through the periodic

randomization of the spin ensemble using bursts of $\frac{\pi}{2}$ -pulses [25]. In principle, the nuclear spin decoherence time T_2 sets the lower limit for τ_m . As the size of the spin ensemble shrinks, the size of the achievable polarization increases as $1/\sqrt{N}$, making such a protocol increasingly relevant as detection volumes continue to shrink. Given that conventional pulse protocols based on thermal polarization require an initialization step taking at least T_1 , waiting for an extended time to capture a large spin fluctuation may be attractive – especially when the magnitude of the captured fluctuation greatly exceeds the possible thermal polarization.

Note that the crucial step in the CSR protocol is that the monitoring and capture occurs in the rotating frame, where the time between statistically independent spin configurations – set by τ_m – is much faster than the equivalent time T_1 in the laboratory frame. This reduced rotating-frame correlation time, allows the system to quickly explore its spin configuration space. On the other hand, once a large fluctuation is captured and transferred to the laboratory frame, the long T_1 effectively freezes the ensemble in this rare configuration.

We therefore show the long-term storage of large spin polarization fluctuations in nanoscale nuclear spin ensembles with $N \sim 10^6$. Storage times as long as 20 s for ^{31}P are demonstrated, limited only by the measurement hardware. The ultimate limit to these times is set only by T_1 in the laboratory frame, which at low temperatures is typically extremely long, exceeding hours for some nuclear spins. While these results were obtained with a low-temperature MRFM, the capture and storage of spin fluctuations should be generally applicable to any technique capable of detecting and addressing nanoscale volumes of nuclear spins in real-time.

5.11 Narrowing of spin polarization fluctuations

The ability to prepare narrowed distributions of nuclear spin polarization may find application in quantum information processing for coherent control of solid-state electron spins, whose dephasing time is often limited by the random nuclear field distribution in the host material [18–22]. We have demonstrated that the nuclear spin polarization capture process is accompanied by a decrease of the width of the nuclear spin polarization distribution, possibly leading to a narrowing or reduction of the randomness in the nuclear magnetic field.

Let the spin fluctuation S and thermal fluctuation T be independent random variables that are normally distributed with mean zero and variance σ_S^2 and σ_T^2 respectively, i.e., the probability density of the spin fluctuation $S = s$ is given by $f_S(s) = N(0, \sigma_S^2)$ and the probability density of the thermal fluctuation $T = t$ is $f_T(t) = N(0, \sigma_T^2)$. Our measurement X contains both a spin fluctuation S and an additive and independent thermal noise fluctuation T . Since S and T are independent, the total fluctuation $X = S + T$ is also normally distributed, with the probability density of $X = x$ given by $f_X(x) = N(0, \sigma_S^2 + \sigma_T^2)$. The conditional probability

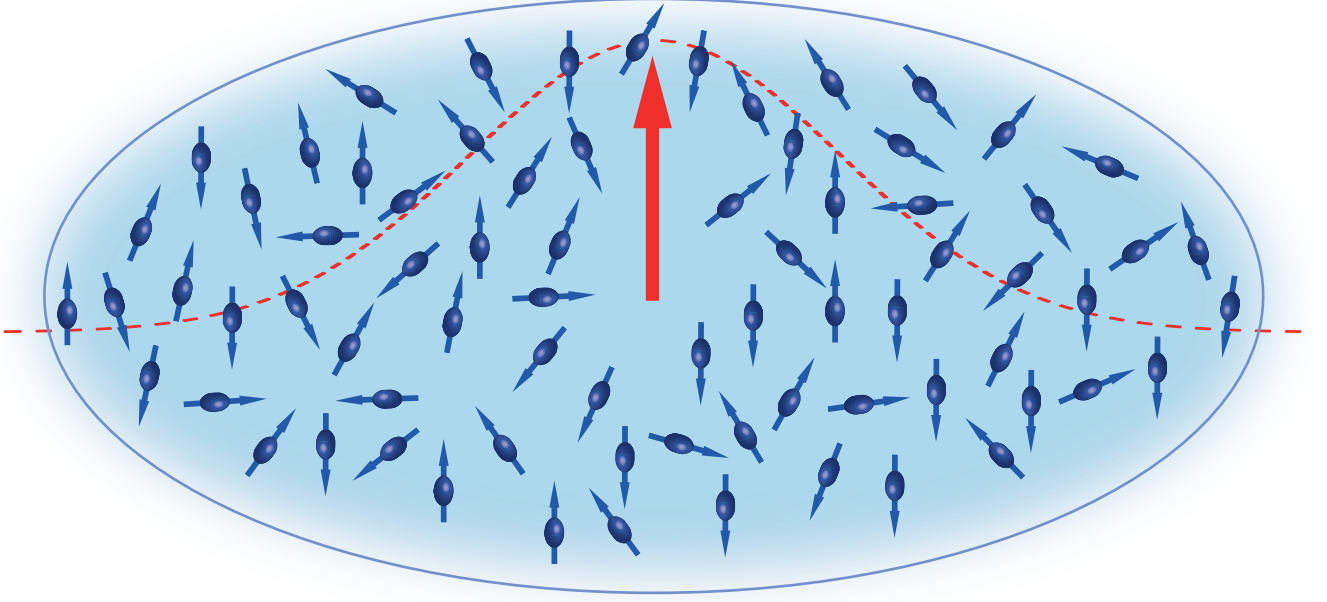


Figure 5.25: An electron spin confined in a quantum dot interacts with the mesoscopic ensemble of nuclear spins ($\sim 10^4$ - 10^6) via hyperfine interaction.

density for the spin fluctuation $S = s$ given the occurrence of the total fluctuation $X = x$ is,

$$\begin{aligned}
f_S(s|X=x) &= \frac{f_T(x-s)f_S(s)}{f_X(x)} \\
&= \frac{1}{\sqrt{2\pi} \frac{\sigma_S \sigma_T}{\sqrt{\sigma_S^2 + \sigma_T^2}}} e^{-\frac{1}{2} \left(\frac{(x-s)^2}{\sigma_T^2} + \frac{s^2}{\sigma_S^2} - \frac{x^2}{\sigma_S^2 + \sigma_T^2} \right)} \\
&= \frac{1}{\sqrt{2\pi} \frac{\sigma_S \sigma_T}{\sqrt{\sigma_S^2 + \sigma_T^2}}} e^{-\frac{1}{2} \left(\left(\frac{1}{\sigma_T^2} + \frac{1}{\sigma_S^2} \right) s^2 - \frac{2sx}{\sigma_T^2} + \frac{x^2}{\sigma_T^2} - \frac{x^2}{\sigma_S^2 + \sigma_T^2} \right)} \\
&= \frac{1}{\sqrt{2\pi} \frac{\sigma_S \sigma_T}{\sqrt{\sigma_S^2 + \sigma_T^2}}} e^{-\frac{1}{2} \left(\frac{1}{\sigma_T^2} + \frac{1}{\sigma_S^2} \right) \left(s^2 - 2s \frac{\sigma_S^2}{\sigma_T^2 + \sigma_S^2} x + \frac{\sigma_S^4}{(\sigma_S^2 + \sigma_T^2)^2} x^2 \right)} \\
&= \frac{1}{\sqrt{2\pi} \frac{\sigma_S \sigma_T}{\sqrt{\sigma_S^2 + \sigma_T^2}}} e^{-\frac{\left(s - \frac{\sigma_S^2}{\sigma_T^2 + \sigma_S^2} x \right)^2}{2 \frac{\sigma_S^2 \sigma_T^2}{\sigma_S^2 + \sigma_T^2}}} .
\end{aligned} \tag{5.1}$$

Therefore, $f_S(s|X=x) = N \left(\frac{\sigma_S^2}{\sigma_S^2 + \sigma_T^2} x, \frac{\sigma_S^2 \sigma_T^2}{\sigma_S^2 + \sigma_T^2} \right)$.

This result means that in an idealized measurement of our CSR protocol, in which the spin component of the captured fluctuation X_c is fully projected onto \mathbf{B}_0 , the stored fluctuation X_s will be normally distributed with a mean $\langle X_s \rangle = X_c \frac{\sigma_S^2}{\sigma_S^2 + \sigma_T^2}$ and a variance $\sigma_{X_s}^2 = \frac{\sigma_S^2 \sigma_T^2}{\sigma_S^2 + \sigma_T^2}$. The fact that $\langle X_s \rangle < X_c$ reflects the finite SNR of the measurement, in this case limited by the cantilever's thermal noise. Note also that the distribution of the stored polarization is narrowed, i.e., it has a reduced variance, compared to the variance of spin polarization under normal evolution ($\sigma_{X_s}^2 < \sigma_S^2$). In the limit of large SNR ($\sigma_S^2 \gg \sigma_T^2$), $\langle X_s \rangle \rightarrow X_c$ and $\sigma_{X_s}^2 \rightarrow 0$. If

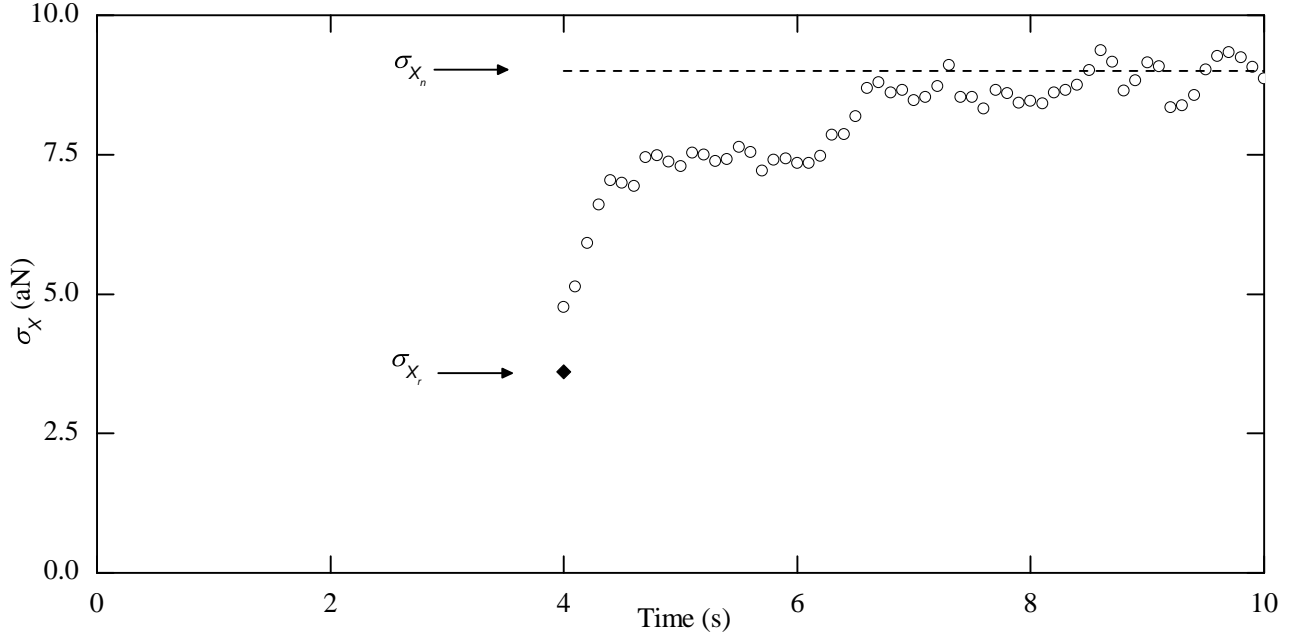


Figure 5.26: $\sigma_X(t)$ calculated over the same 100 sequences (as in Fig. 5.21) showing the narrowed variance of the retrieved fluctuation σ_{X_r} (filled diamond) as it equilibrates back to its rotating frame value σ_{X_n} (dotted line).

during T_{store} this stored polarization undergoes negligible relaxation in the laboratory frame, the corresponding retrieved fluctuation X_r has a mean $\langle X_r \rangle = \langle X_s \rangle$. However, the variance will include the additional thermal noise of the measurement: $\sigma_{X_r}^2 = \frac{\sigma_s^2 \sigma_T^2}{\sigma_s^2 + \sigma_T^2} + \sigma_T^2$ as we measure both the spin signal and the thermal noise during the retrieval measurement. In other words, $\sigma_{X_r}^2 > \sigma_{X_s}^2$ due to the finite SNR of the measurement.

Fig. 5.26 shows the reduced standard deviation of the retrieved polarization σ_{X_r} , eventually approaching σ_{X_n} after a time on the order of τ_m in the rotating frame. Note that τ_l is much shorter than the time over which σ_{X_r} evolves, excluding the lock-in as a source of the behavior. Further beyond the first few lock-in time constants, the suppression of the total fluctuations proves that the spin fluctuations are reduced in the nuclear spin state. Thus, we have reported a method of preparing the nuclear spin ensemble that suppresses or narrows the distribution of nuclear spin polarization fluctuations below its equilibrium value by a factor of six. The degree of narrowing demonstrated is limited by the SNR of the measurement. The polarization of the nuclear spin ensemble could be initialized to a narrow distribution of values before each measurement which may provide us the ability to enhance the electron-spin dephasing time.

Chapter 6

Magnet-on-Cantilever MRFM

This Chapter provides a brief mention of the experimental work performed towards the realisation of a magnet-on-cantilever MRFM setup. During the course of this work (roughly ~ 1 year), many technical difficulties and challenges were encountered, some of which still remain unresolved.

6.1 Introduction

There are two variants in the geometry of MRFM: sample-on-cantilever and magnet-on-cantilever. The recent progress in MRFM has largely been confined to the sample-on-cantilever geometry resulting in the spin detection sensitivity and spatial resolution achievable on the order of 10^3 spins and 10 nm respectively [3, 61]. On the other hand, the magnet-on-cantilever geometry would give us more flexibility in studying a wide variety of samples ranging from molecules on surfaces to self-assembled and gate-defined quantum dots (QDs) in GaAs heterostructures [62–64]. The magnet-tipped cantilever, serving as an AFM-like scanning probe, can be readily integrated into existing transport and optical setups used for studying the physics of quantum dots. Such a geometry would also obviate the requirement of attaching a sample to the cantilever, thereby offering flexibility to study arbitrary samples lying on a surface.

Pushing the limits of spin detection in the magnet-on-cantilever setup would enable us to conceive and realize magnetic resonance experiments in gate-defined quantum dots (QDs), QDs grown by molecular beam/droplet epitaxy and many more types of nanostructures such as quantum wells and nanowires. MRFM has the sensitivity to detect the statistical polarization fluctuations of ensembles containing 10^6 nuclear spins. It could therefore serve as a useful tool for measuring dynamic nuclear spin polarization (DNSP) and Knight shifts taking place due to electron-nuclear hyperfine interactions [65]. The roughly 10^5 nuclear spins present in typical semiconductor QDs are the leading cause of spin decoherence for electrons trapped in the dot [16, 17].

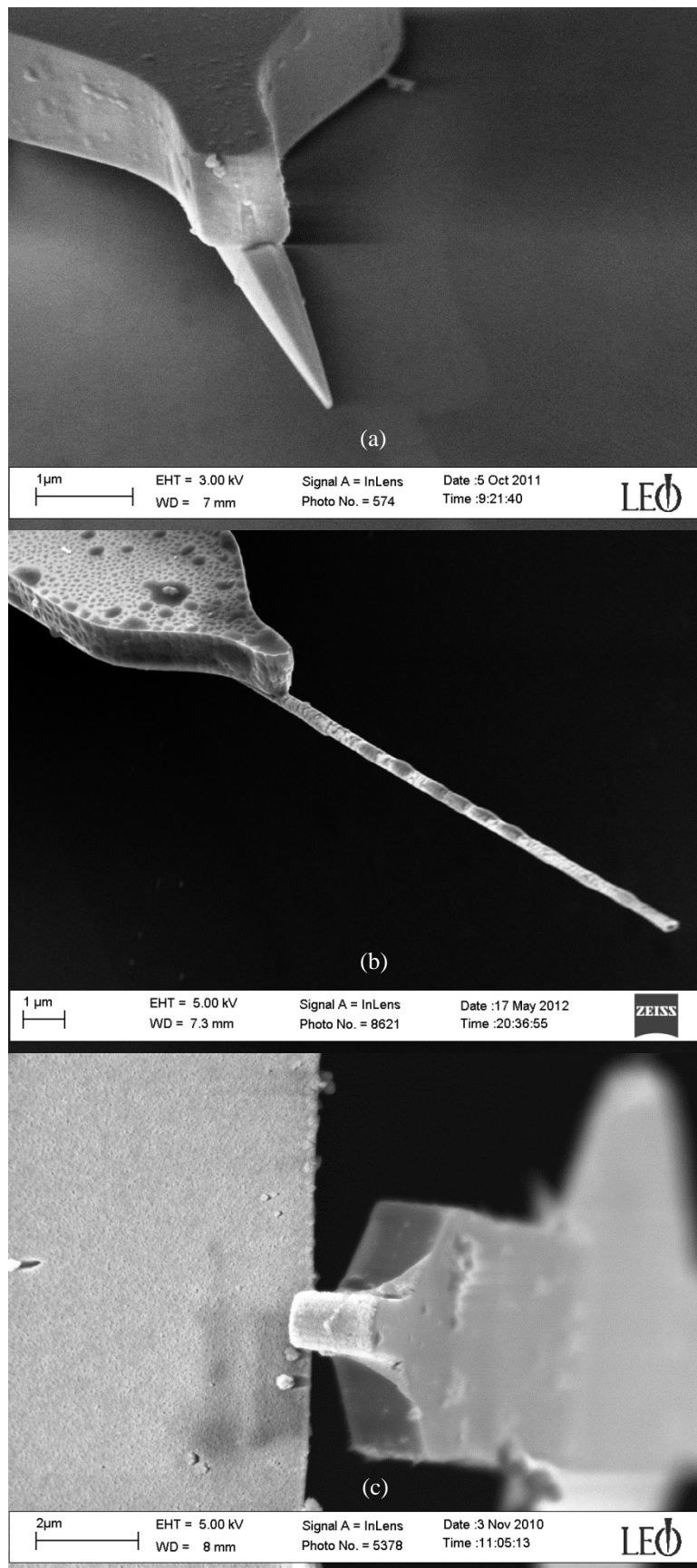


Figure 6.1: Three different types of magnetic tips are studied for magnet-on-cantilever MRFM experiments. (a) and (c) The cantilever tips evaporated with FeCo. (b) Ni ferromagnetic nanowires.

6.2 Magnetic tips

Previous MRFM studies using a magnet-on-cantilever setup have employed magnets made of hard or high anisotropy magnetic materials [8]. A micron-sized magnet was glued to the cantilever in an orienting magnetic field, and then further shaped using a focused ion beam (FIB) resulting in a sharper and smaller magnet. Such magnets provided gradients on the order of 10^5 T/m and showed negligible magnetic dissipation as demonstrated by cantilever magnetometry measurements [56]. The quality factor of the magnet-tipped cantilever decreased only marginally in the presence of the magnetic fields of a few tesla possibly due to the high anisotropy of the magnet. However, the complex fabrication procedures (using a FIB) required for preparing such magnets does not make it an attractive and convenient option for achieving a large gradient in a MRFM experiment.

Soft magnetic materials, such as FeCo, offer higher saturation magnetization compared to other available hard materials. Also, FeCo nanomagnetic tips can be integrated onto a microwire RF source using standard clean room processing techniques. These magnets have been shown to provide large gradients on the order of 10^6 T/m in a sample-on-cantilever setup [3]. A thin film of Ti/FeCo (10/90 nm) evaporated onto the end of the cantilever might seem to be a promising candidate for a magnet-on-cantilever experiment (Fig. 6.1). However, such cantilevers experience large dissipation in a magnetic field due to the oscillatory canting of the magnetic moment of the film [56]. In other words, magnetic friction occurs because the moment rotates while trying to follow the direction of the external magnetic field. This dissipation can be avoided by working in a MRFM geometry where the external magnetic field is oriented parallel to the cantilever's angular rotation vector. Therefore, we have built a novel perpendicular geometry setup for performing nanoscale MRFM experiments [66]. In such a setup, as the cantilever oscillates, it does not change its angle with respect to the applied magnetic field. However, performing an MRFM experiment in the perpendicular geometry has proven to be challenging in practice, mainly because the MRFM probe is somehow coupled to the external vibrations for still unknown reasons.

The saturation magnetization that was determined from cantilever magnetometry measurements on the Ni nanowire is approximately $\mu_0 M = 0.5$ T [67], which is about three times smaller than the magnetization of the FeCo tips reported in the tobacco mosaic virus (TMV) experiment [3]. This means that a gradient just above 10^6 T/m is expected at a distance of 25 nm. Our FeCo tips, in practice, are not achieving the same gradients as in the TMV experiment, perhaps due to a thicker oxidation layer or other contamination processes in the sample preparation. The other reasons for our FeCo tips not being of good quality are the methods with which the tips are fabricated - using a public evaporator and not baking the system before evaporation etc. The recent calculations of point spread function (PSF) for the InP/GaP nanowire experiments would seem to strongly back up these claims. So, probably these Ni nanowire tips are expected to be only a small factor worse than our current FeCo tips and it seems promising to use these tips for the magnet-on-cantilever experiments. They also serve two other advantages. First, there is no need to evaporate metal on the cantilever tip, as the nanowires

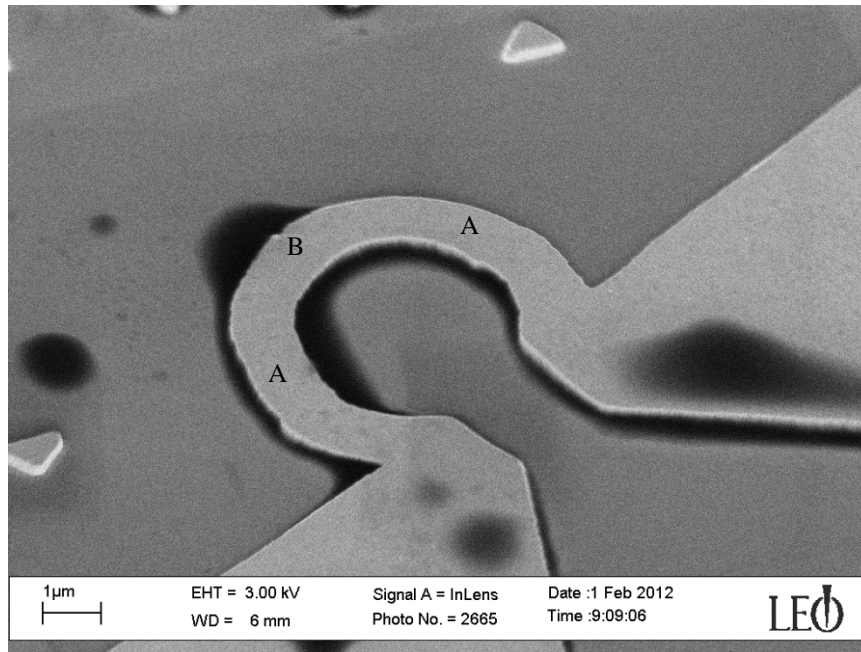


Figure 6.2: SEM micrograph of the microcoil. The magnet-tipped cantilever, when positioned at ‘A’, experiences much less excitation from the current flowing underneath it, than at ‘B’.

are quite long 10-15 μm and already coated with metal. Second, the drop in Q in the normal MRFM geometry (not perpendicular) is very low even at MRFM operating fields around 3 T. The quality factor of Ni nanowire tipped cantilever stays almost constant at 30000 on ramping up the magnetic field from 0 T to 3 T. In fact, Ni ferromagnetic nanowires experience negligible dissipation in both configurations (normal and perpendicular). The ferromagnetic Ni nanowires serving as sources of magnetic field gradient can be glued to the tip of the cantilever using a micromanipulator setup. However, no MRFM signal is observed with these Ni nanowires, probably because the gradients realised are too small and the volume of the resonant slice too tiny.

6.3 Microcoil

There exists spurious interaction between the RF microwire and the magnetic tip which leads to an excitation of the cantilever [61]. Our experimental studies conclude that this interaction depends on the orientation of the cantilever with respect to the direction of the RF field generated from the wire. Therefore, we have made a microcoil device to minimize these interactions (Fig. 6.2).

6.4 Outlook

The important ingredient for performing a magnet-on-cantilever MRFM experiment is a cantilever with an attached magnetic tip which can provide a large field gradient. Such a tip should be of high quality and not dissipate any energy from the cantilever even in the presence of large magnetic fields. Therefore, it's worthwhile to

consider other strategies for fabricating magnetic tips which are equally applicable for both tip-on microwire and tip-on-cantilever experiments. High quality magnetic tips are currently being used for sensitive measurements in magnetic force microscopy (MFM). Their expertise can be borrowed to make better tips than that are currently employed in MRFM. These magnetic tips are prepared by sputtering (rather than e-beam evaporation) by depositing 5-20 nm of Co and further capping it with Cr or Pt to prevent oxidation. Such magnetic tips intended to be used for MRFM can be fabricated by sputtering InGaAs nanoneedle samples with a magnetic material. These tips are magnetically “hard” and could be used in the normal MRFM geometry [68]. On the other hand, evaporating FeCo or Dy on the nanoneedles would make these tips magnetically “soft” which requires the experiments to be performed in the perpendicular geometry.

Chapter 7

Outlook

This thesis mainly dealt with creating order in small ensembles of nuclear spins by harnessing its random fluctuations using the technique of magnetic resonance force microscopy. Here, we outline some of the potential applications of this novel technique.

1. The ability to create, manipulate, store and retrieve polarization in the nuclear spin environment of nanoscale systems is important for the development of novel nuclear magnetic resonance (NMR) techniques and the implementation of memory devices. The thermal equilibrium polarization being small in nanoscale nuclear spin ensembles, the other methods to create nuclear spin order must be considered. When polarization cannot be created via techniques such as Overhauser-mediated dynamic nuclear spin polarization or Hartmann-Hahn cross-polarization transfer between polarized and unpolarized nuclei, the selective capture of large statistical fluctuations enhances the sensitivity to detect the weak magnetism from nuclear spins. The ensembles polarized in this work, nanometer-scale volumes of ^1H on an adsorbate layer and ^{31}P in a single semiconducting NW, demonstrate the types of samples which could benefit from this technique. One could imagine, for instance, such nuclear spin polarization capture processes enhancing the weak MRI signals of a nanometer-scale ^1H -containing biological sample on a surface or of a semiconducting nanostructure.
2. Conventional NMR and MRI techniques applied to large spin ensembles have mostly relied on manipulating thermal equilibrium polarization to produce resonance signals. However, as the size of the detection volume continues to shrink, the time-dependent excursions of the nuclear spin polarization become increasingly larger compared to the mean thermal polarization. Moreover, the polarization of the ensemble has a fluctuating or noisy nature resulting in a random amplitude and sign. Therefore, it's worthwhile to consider and develop novel detection techniques that take advantage of harnessing the intrinsic statistical polarization fluctuations to observe magnetic resonance in nanoscale nuclear spin ensembles. The temporal

control gained over the nuclear spin polarization fluctuations in this work can provide a means to initialize the nuclear spin ensemble with a fixed sign and large amplitude. Such initialization schemes can provide the basis for realizing advanced pulse protocols which can be borrowed directly from conventional NMR to enhance detection sensitivity and acquire NMR spectra of statistically polarized samples.

3. For example, previous work to detect nuclear double resonance in self-polarized ensembles of heteronuclear coupled spins has focused on continuous-wave magnetic resonance techniques [69], which are unsuitable for the manipulation required for cross-polarization transfer between dipolar-coupled spins. A further step forward will be to extend the nuclear spin storage measurements presented here to observe polarization transfer between different spin species, which will serve as a new contrast mechanism - a valuable tool in nano-MRI. In our capture-store-readout sequence, the capture and readout of the polarization is performed on the same nuclear spin species (I-spin). In principle, the large polarization stored in the laboratory frame can be transferred to other nuclear spin species having a low-gamma (S-spin) using Hartmann-Hahn method of cross-polarization. The real-time switching and control of RF fields we have achieved would allow us to perform the readout of the polarization on the S-spin species thus resulting in a direct real-time observation of polarization transfer in small spin ensembles which would be the first of its kind.

4. The experimental demonstration of fast real-time radio frequency control techniques on nuclear spin systems may become a useful tool in the preparation of narrowed and polarized nuclear spin states. Such states lead to an enhancement of coherence times of spin qubits with promising applications in quantum information and ultrasensitive magnetometry tasks [70]. One of the future challenges will be to integrate the classical feedback control techniques presented here with the full quantum control of electron spins in the solid-state environment. With the recent advance of a large gradient in a magnet-on-cantilever MRFM experiment [61], the proposed techniques should enable efficient implementation of quantum computational tasks based on spin qubits in gate-defined and self-assembled quantum dots, nitrogen vacancy centers [71] and many more types of nanostructures such as quantum wells and nanowires.

Appendix A

FPGA Programs

A.1 Steps to run the laser PID controller

1. Open **Laser PID Controller (Host).vi** which is the host VI.
2. Click the **Calibrate Gains** and specify the **AC Preamplifier Gain** and **DC Preamplifier Gain**, which are the preamplifier gains for the AC and DC signals respectively.
3. The **Sample Rate (S/s)** for the FPGA loop is set as 10 Hz. Make sure that the **PID** loop in FPGA VI also has the same sampling frequency.
4. Slide the **TEC Manual (Ohms)** through one cycle so that the photodiode signal moves through 2-3 fringes and observe that the **Fringe Max. (V)**, **Fringe Min. (V)**, **Fringe Average (V)**, **Fringe Amplitude (V)** and **Fringe Visibility** changes, and finally leave the **TEC Manual (Ohms)** at 0.
5. Click the **Set Setpoint & Calibrate** which sets the **Fringe Average (V)** to **Setpoint (V)**.
6. Click the **Feedback** and adjust the **Output Gain** and **PID Gains** so that the fringe locks on the **Setpoint (V)**.
7. **Slope** functionality can make the PID loop to lock on either the positive or negative slope of the fringe.
8. Click the **STOP Host** so that it leaves the PID loop running in the FPGA hardware.
9. Clicking the **STOP FPGA** aborts the running PID loop in FPGA but leaves the host VI running.

A.2 Steps to run the displacement PID controller

Note: Before running the **Displacement PID Controller**, make sure that the photodiode signal is locked on the center of the fringe.

1. Open **Displacement PID Controller (Host).vi** which is the host VI.
2. Click **Run Continuously** button to measure the **Displacement (nm-rms)**.
3. Specify the desired **Set Displacement (nm-rms)**.
4. Click the **Self-osc. (On/Off)** and adjust the **Proportional Gain (Kc)** to get a stable self-oscillation signal.

A.3 Steps to run the phase shifter

Note: Before using this program for a real cantilever signal, it is recommended to test the phase shift functionality for any 1-10 KHz clean sinusoidal signal with the help of a lock-in amplifier. This phase shifter can also be used for damping the cantilever vibrations. The principle of damping caused by 90 degrees phase shift strictly applies only if there are no signal paths and filters placed before and after the phase shifter as they cause unintended physical time delays and phase delays. Therefore, it is advisable to have amplified (but unfiltered!) signal from the preamplifier as the input of the FPGA program and the output is directly sent to the piezo without any filtering by the preamplifier.

1. Open **Phase_Shifter(Host).vi** which is the host VI of the project.
2. Specify the **Cantilever Frequency**.
3. Set the **Phase (Degrees)** to the desired phase shift.
4. Adjust the **Tunable Gain** as required for your application. A **Tunable Gain** of 1 corresponds to an output/input amplitude ratio of 1.

Appendix B

MATLAB simulation of spin noise

```
Fs = 100; sample rate (samples per second)
P = 10; time of simulation
M = 10000;
Z = zeros(M,P*Fs);
Y = zeros(1,P*Fs);
A = zeros(1,P*Fs);
for m = 1:M
N = 20; number of switches in realization
lambda = .5; switching rate (switches per second)
X = [];
S = rand(1,N); uniform random variables
T = -log(S)/lambda; transform to exponential RVs
V = cumsum(T); switching times
for i = 1:2
state(i) = -1+(i-1)*2;
end
j = randi(2,1);
state = state(j);
Nsold = 1;
for k = 1:N
Nsnew = ceil(V(k)*Fs); new switching time
Ns = Nsnew - Nsold; number of samples in current switching interval
X = [X state*ones(1,Ns)];
state = -state; switch state
```

```
Nsold = Nsnew;
end
t = [1:length(X)]/Fs; time axis
for l = 1:P*Fs
Y(l) = X(l);
end
u = [1:length(Y)]/Fs;
Z(m,:) = Y;
end
for n = 1:P*Fs
A(n) = 0;
for o = 1:M
A(n) = A(n) + Z(o,n);
end
end
plot(u,A)
v = transpose(u);
B = transpose(A);
savefile = 'noise.mat';
save(savefile,'v','B');
```

Appendix C

Microcoil fabrication steps

1. Cut GaAs wafer into 3 mm by 4 mm samples.
2. Spin 1 mm thick PMMA onto the sample. (4000 rpm for 40 s)
3. With the help of e-beam lithography, define the microwire, markers and the big leads.
4. Dip the patterned sample in the developer for 75 s and then in IPA for 15 s.
5. Check the quality of the developed pattern under the optical microscope.
6. Evaporate 10/190 nm of Ti/Au.
7. Insert the sample in NMP for 30 minutes and then in Acetone for 5 minutes for liftoff purposes.
8. Insert the sample in Ethanol for 5 minutes and finally in IPA for 5 minutes for liftoff.
9. After further rinsing the sample in distilled water for 5 minutes, the microcoil is ready to be used.

Bibliography

- [1] F. Bloch, *Phys. Rev.* **70**, 460 (1946).
- [2] E. A. Chekhovich, M. N. Makhonin, A. I. Tartakovskii, A. Yacoby, H. Bluhm, K. C. Nowack, and L. M. K. Vandersypen, *Nature Mater.* **12**, 494 (2013).
- [3] C. L. Degen, M. Poggio, H. J. Mamin, , C. T. Rettner, and D. Rugar, *Proc. Natl. Acad. Sci. USA* **106**, 1313 (2009).
- [4] N. Zhao, J. Honert, B. Schmid, M. Klas, J. Isoya, M. Markham, D. Twitchen, F. Jelezko, R.-B. Liu, H. Fedder, and J. Wrachtrup, *Nature Nanotech.* **7**, 657 (2012).
- [5] J. R. Maze, P. L. Stanwix, J. S. Hodges, S. Hong, J. M. Taylor, P. Cappellaro, L. Jiang, M. V. G. Dutt, E. Togan, A. S. Zibrov, A. Yacoby, R. L. Walsworth, and M. D. Lukin, *Nature* **455**, 644 (2008).
- [6] G. Balasubramanian, I. Y. Chan, R. Kolesov, M. Al-Hmoud, J. Tisler, C. Shin, C. Kim, A. Wojcik, P. R. Hemmer, A. Krueger, T. Hanke, A. Leitenstorfer, R. Bratschitsch, F. Jelezko, and J. Wrachtrup, *Nature* **455**, 648 (2008).
- [7] T. Sleator, E. L. Hahn, C. Hilbert, and J. Clarke, *Phys. Rev. Lett.* **55**, 1742 (1985).
- [8] H. J. Mamin, R. Budakian, B. W. Chui, and D. Rugar, *Phys. Rev. B* **72**, 024413 (2005).
- [9] H. J. Mamin, M. Kim, M. H. Sherwood, C. T. Rettner, K. Ohno, D. D. Awschalom, and D. Rugar, *Science* **339**, 557 (2013).
- [10] D. Rugar, C. S. Yannoni, and J. A. Sidles, *Nature* **360**, 563 (1992).
- [11] D. Rugar, O. Zueger, S. Hoen, C. S. Yannoni, H. M. Vieth, and R. D. Kendrick, *Science* **264**, 1560 (1994).
- [12] J. A. Sidles, J. L. Garbini, K. J. Bruland, D. Rugar, O. Zueger, S. Hoen, and C. S. Yannoni, *Rev. Mod. Phys.* **67**, 249 (1995).
- [13] H. J. Mamin and D. Rugar, *Appl. Phys. Lett.* **79**, 3358 (2001).
- [14] J. A. Sidles, *Appl. Phys. Lett.* **58**, 2854 (1991).

- [15] T. Staudacher, F. Shi, S. Pezzagna, J. Meijer, J. Du, C. A. Meriles, F. Reinhard, and J. Wrachtrup, *Science* **339**, 561 (2013).
- [16] I. A. Merkulov, A. L. Efros, and M. Rosen, *Phys. Rev. B* **65**, 205309 (2002).
- [17] A. V. Khaetskii, D. Loss, and L. Glazman, *Phys. Rev. Lett.* **88**, 186802 (2002).
- [18] W. A. Coish and D. Loss, *Phys. Rev. B* **70**, 195340 (2004).
- [19] D. J. Reilly, J. M. Taylor, J. R. Petta, C. M. Marcus, M. P. Hanson, and A. C. Gossard, *Science* **321**, 817 (2008).
- [20] C. Latta, A. Hoegle, Y. Zhao, A. N. Vamivakas, P. Maletinsky, M. Kroner, J. Dreiser, I. Carusotto, A. Badolato, D. Schuh, W. Wegscheider, M. Atatüre, and A. Imamoglu, *Nature Phys.* **5**, 758 (2009).
- [21] I. T. Vink, K. C. Nowack, F. H. L. Koppens, J. Danon, Y. V. Nazarov, and L. M. K. Vandersypen, *Nature Phys.* **5**, 764 (2009).
- [22] H. Bluhm, S. Foletti, D. Mahalu, V. Umansky, and A. Yacoby, *Phys. Rev. Lett.* **105**, 216803 (2010).
- [23] R. Budakian, H. J. Mamin, B. W. Chui, and D. Rugar, *Science* **307**, 408 (2005).
- [24] J. A. Sidles and D. Rugar, *Phys. Rev. Lett.* **70**, 3506 (1991).
- [25] C. L. Degen, M. Poggio, H. J. Mamin, and D. Rugar, *Phys. Rev. Lett.* **99**, 250601 (2007).
- [26] C. P. Slichter, *Principles of Magnetic Resonance* (Springer Series, 1996).
- [27] J. J. Sakurai, *Modern Quantum Mechanics* (Addison-Wesley, 1994).
- [28] H. Gassmann, M. S. Choi, H. Yi, and C. Bruder, *Phys. Rev. B* **69**, 115419 (2004).
- [29] J. Baum, R. Tycko, and A. Pines, *Phys. Rev. A* **32**, 3435 (1985).
- [30] A. Tannus and M. Garwood, *J. Magn. Reson., Ser. A* **120**, 133 (1996).
- [31] G. P. Berman, F. Borgonovi, and V. I. Tsifrinovich, *Phys. Rev. B* **72**, 224406 (2005).
- [32] C. L. Degen, M. Poggio, H. J. Mamin, and D. Rugar, *Phys. Rev. Lett.* **100**, 137601 (2008).
- [33] J. A. Sidles, J. L. Garbini, and G. P. Drobny, *Rev. Sci. Instrum.* **63**, 3881 (1992).
- [34] D. Mozyrsky, I. Martin, D. Pelekhov, and P. C. Hammel, *Appl. Phys. Lett.* **82**, 1278 (2003).
- [35] G. P. Berman, V. N. Gorshkov, D. Rugar, and V. I. Tsifrinovich, *Phys. Rev. B* **68**, 094402 (2003).
- [36] D. Gamliel and H. Levanon, *Stochastic Processes in Magnetic Resonance* (World Scientific, 1995).
- [37] D. Rugar, R. Budakian, H. J. Mamin, and B. W. Chui, *Nature* **430**, 329 (2004).
- [38] C. G. Cassandras and S. Lafortune, *Introduction to Discrete Event Systems* (Springer Series, 2008).

- [39] R. Kubo, J. Phys. Soc. Jpn. **9**, 935 (1954).
- [40] P. W. Anderson, J. Phys. Soc. Jpn. **9**, 316 (1954).
- [41] Z. Deng and J. Eberly, Optics Comm. **51**, 189 (1984).
- [42] F. Xue, D. P. Weber, P. Peddibhotla, and M. Poggio, Phys. Rev. B **84**, 205328 (2011).
- [43] C. Kittel, *Elementary Statistical Physics* (John Wiley & Sons, 1958).
- [44] E. W. Weisstein, *Binomial Distribution* (Wolfram Mathworld).
- [45] R. Kubo, M. Toda, and N. Hashitsume, *Nonequilibrium Statistical Mechanics* (Springer Series, 1998).
- [46] J. P. Jacky, J. L. Garbini, M. Ettus, and J. A. Sidles, Rev. Sci. Instrum. **79**, 123705 (2008).
- [47] M. Poggio, C. L. Degen, C. T. Rettner, H. J. Mamin, and D. Rugar, Appl. Phys. Lett. **90**, 263111 (2007).
- [48] D. Rugar, H. J. Mamin, R. Erlandsson, J. E. Stern, and B. D. Terris, Rev. Sci. Instrum. **59**, 2337 (1988).
- [49] K. J. Bruland, J. L. Garbini, W. M. Dougherty, S. H. Chao, S. E. Jensen, and J. A. Sidles, Rev. Sci. Instrum. **70**, 3542 (1999).
- [50] A. Greilich, A. Shabaev, D. R. Yakovlev, A. L. Efros, I. A. Yugova, D. Reuter, A. D. Wieck, and M. Bayer, Science **317**, 1896 (2007).
- [51] X. Xu, W. Yao, B. Sun, D. G. Steel, A. S. Bracker, D. Gammon, and L. J. Sham, Nature **459**, 1105 (2009).
- [52] E. Togan, Y. Chu, A. Imamoglu, and M. D. Lukin, Nature **478**, 497 (2011).
- [53] T. Sleator, E. L. Hahn, C. Hilbert, and J. Clarke, Phys. Rev. B **36**, 1969 (1987).
- [54] J. M. Nichol, T. R. Naibert, E. R. Hemesath, L. J. Lauhon, and R. Budakian, (2013).
- [55] S. Assali, I. Zardo, S. Plissard, D. Kriegner, M. A. Verheijen, G. Bauer, A. Meijerink, A. Belabbes, F. Bechstedt, J. E. M. Haverkort, and E. P. A. M. Bakkers, Nano Lett. **13**, 1559 (2013).
- [56] B. C. Stipe, H. J. Mamin, T. D. Stowe, T. W. Kenny, and D. Rugar, Phys. Rev. Lett. **87**, 096801 (2001).
- [57] H. J. Mamin, C. T. Rettner, M. H. Sherwood, L. Gao, and D. Rugar, Appl. Phys. Lett. **100**, 013102 (2012).
- [58] I. T. Tomka, J. D. van Beek, R. Joss, and B. H. Meier, Phys. Chem. Chem. Phys. **15**, 3438 (2013).
- [59] H. J. Mamin, R. Budakian, B. W. Chui, and D. Rugar, Phys. Rev. Lett. **91**, 207604 (2003).
- [60] S. O. Rice, *Mathematical analysis of random noise* (Bell Telephone Laboratories, 1944).
- [61] J. G. Longenecker, H. J. Mamin, A. W. Senko, L. Chen, C. T. Rettner, D. Rugar, and J. A. Marohn, ACS Nano **6**, 9637 (2012).
- [62] P. Maletinsky, M. Kroner, and A. Imamoglu, Nature Phys. **5**, 407 (2009).

- [63] M. N. Makhonin, K. V. Kavokin, P. Senellart, A. Lematre, A. J. Ramsay, M. S. Skolnick, and A. I. Tartakovskii, *Nature Mater.* **10**, 844 (2011).
- [64] E. A. Chekhovich, K. V. Kavokin, J. Puebla, A. B. Krysa, M. Hopkinson, A. D. Andreev, A. M. Sanchez, R. Beanland, M. S. Skolnick, and A. I. Tartakovskii, *Nature Nanotech.* **7**, 646 (2012).
- [65] P. Maletinsky, A. Badolato, and A. Imamoglu, *Phys. Rev. Lett.* **99**, 056804 (2007).
- [66] F. Xue, P. Peddibhotla, M. Montinaro, D. P. Weber, and M. Poggio, *Appl. Phys. Lett.* **98**, 163103 (2011).
- [67] D. P. Weber, D. Rueffer, A. Buchter, F. Xue, E. Russo-Averchi, R. Huber, P. Berberich, J. Arbiol, A. F. i Morral, D. Grundler, and M. Poggio, *Nano Lett.* **12**, 6139 (2012).
- [68] P. C. Hammel and D. V. Pelekhov, *The Magnetic Resonance Force Microscope (Handbook of Magnetism and Advanced Magnetic Materials)* (John Wiley & Sons, 2007).
- [69] M. Poggio, H. J. Mamin, C. L. Degen, M. H. Sherwood, and D. Rugar, *Phys. Rev. Lett.* **102**, 087604 (2009).
- [70] J. M. Taylor, P. Cappellaro, L. Childress, L. Jiang, D. Budker, P. R. Hemmer, A. Yacoby, R. Walsworth, and M. D. Lukin, *Nature Phys.* **4**, 810 (2008).
- [71] S. Kolkowitz, A. C. B. Jayich, Q. P. Unterreithmeier, S. D. Bennett, P. Rabl, J. G. E. Harris, and M. D. Lukin, *Science* **335**, 1603 (2012).

Curriculum Vitae

Background

<i>Birth</i>	29th of August, 1983
<i>Citizenship</i>	India
<i>Languages</i>	English

Education

<i>Apr. 2009 – June 2013</i>	Ph.D. in Physics, University of Basel, Switzerland
<i>Oct. 2006 – Dec. 2008</i>	M.Sc. in Micro and Nanosystems, ETH Zurich, Switzerland
<i>Sep. 2001 – May 2005</i>	B.Tech. in Mechanical Engineering, Indian Institute of Technology, Madras, India

Employment

<i>July 2005 – June 2006</i>	Software Engineer , IBM Global Services, Bangalore, India
------------------------------	--

List of Publications

1. **Harnessing nuclear spin polarization fluctuations in a semiconductor nanowire**,
P. Peddibhotla, Fei Xue, H. I. T. Hauge, S. Assali, E. P. A. M. Bakkers and M. Poggio,
Under review.
2. **Feedback cooling of cantilever motion using a quantum point contact transducer**,
M. Montinaro, A. Mehlin, H. S. Solanki, **P. Peddibhotla**, S. Mack, D. D. Awschalom, and M. Poggio,
Applied Physics Letters **101**, 133104 (2012).
3. **Measurement of statistical nuclear spin polarization in a nanoscale GaAs sample**,
Fei Xue, D. P. Weber, **P. Peddibhotla**, and M. Poggio,
Physical Review B **84**, 205328 (2011).
4. **A geometry for optimizing nanoscale magnetic resonance force microscopy**,
Fei Xue, **P. Peddibhotla**, M. Montinaro, D. P. Weber, and M. Poggio,
Applied Physics Letters **98**, 163103 (2011).